Structural Response of Shells

to Shock and Detonation Loading

by

W.M. Beltman
University of Twente
Faculty of Mechanical Engineering
PO Box 217
7500 AE Enschede
The Netherlands

and

J.E. Shepherd
Aeronautics
California Institute of Technology
Pasadena, CA 91125

Technical Report FM98-3
Graduate Aeronautical Laboratories

April 1998

Structural response of shells to detonation and shock loading, part I: theory

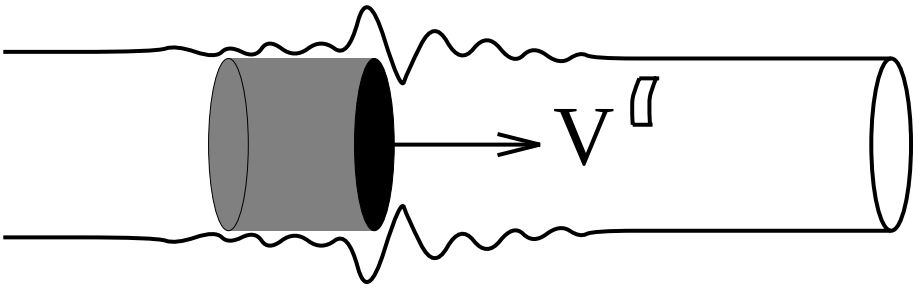

W.M. Beltman
University of Twente
Faculty of Mechanical Engineering
P.O. Box 217
7500 AE Enschede
The Netherlands

Advisor
Prof. J.E. Shepherd
California Institute of Technology
Graduate Aeronautical Laboratories
Pasadena, CA 91125
U.S.A.

June 4, 1999

Summary

The internal shock or detonation loading of cylindrical shells involves loads that propagate at high speeds. Several analytical models are available to calculate the structural response of shells to this type of loading. These models show that the speed of the load is an important parameter. In fact, for a linear model of a shell of infinite length, the amplitude of the radial deflection becomes unbounded when the speed of the shock or detonation is equal to a critical velocity. This "resonance" is due to the excitation of flexural waves in the shell. The critical velocity is a function of material and geometrical properties of the tube. It is evident that simple (static) design formulas are no longer accurate in this case. The present report deals with a numerical and experimental study on the structural response of cylindrical shells to shock or detonation loading. In part I of this report, the theoretical models are described. Several analytical models were developed for tubes of infinite length. By assuming an infinite tube, the problem reduces to a steady state problem. This greatly simplifies the analysis. However, reflections and interference of waves can lead to high strains and stresses in the tube. Therefore analytical models were developed to describe the transient motion of finite length thin cylindrical shells to shock or detonation loading. Finally, transient finite element models were developed. The finite element model enables a more realistic modelling of boundary conditions.

Nomenclature

A_4	dispersion premultiplication factor	
A_2	dispersion premultiplication factor	
A_0	dispersion premultiplication factor	
E	Young's modulus	N/m^2
F	dimensionless loading function	
F_x	axial force	N
F_s	dimensionless static loading function	
F_d	dimensionless dynamic loading function	
G	shear modulus	N/m^2
L	length of shell	m
M_{xx}	moment resultant	N
N_{xx}	axial stress resultant	N/m
$N_{\theta\theta}$	circumferential stress resultant	N/m
Q_x	shear stress resultant	N/m
R	shell mean radius	m
T	exponential decay factor	s
a_q	static participation factor	
b_q	dynamic participation factor	
h	shell thickness	m
i	imaginary unit	
k	wave number	$1/m$
l	shell length	m
m, m_1, m_2	characteristic roots	
n, n_1, n_2	characteristic roots	
p_1	pre-shock pressure	Pa
p_2	post-shock pressure	Pa
p_{atm}	atmospheric pressure	Pa
p_∞	final pressure	Pa
q	mode index	
r	mode index	
t	time	s
u	axial deflection	m
$\overline{u}$	dimensionless axial deflection	

v	load speed	m/s
v_{c0}	critical velocity	m/s
v_{c1}	shear wave velocity	m/s
v_{c2}	dilatational wave velocity in a bar	m/s
v_{c3}	dilatational wave velocity	m/s
v_d	dilatational wave speed	m/s
v_s	shear wave speed	m/s
w	radial deflection	m
$\overline{w}$	dimensionless radial deflection	
$\overline{w}_b$	dimensionless radial deflection, bending	
$\overline{w}_b^I$	dimensionless radial deflection region I	
$\overline{w}_b^{II}$	dimensionless radial deflection region II	
x	axial coordinate	m
α	characteristic root	
β	shell thickness parameter	
$\overline{\eta}$	dimensionless (moving) axial coordinate	
$\overline{\eta}_0$	dimensionless exponential decay factor	
Δp	pressure difference across shell	Pa
κ	shear correction factor	
ν	Poisson's ratio	
ρ	density	kg/m^3
ψ_x	rotation	
$\overline{\psi}$	rotation	
Λ_j	excitation parameter ($j = 1, 2, \infty$)	
Λ_j^s	excitation parameter ($j = 1, 2, \infty$)	
Λ_j^d	excitation parameter ($j = 1, 2, \infty$)	

Contents

List of Figures

List of Tables

Acknowledgments

This report is the result of a six months stay at the Graduate Aeronautical Laboratories of the California Institute of Technology. I was offered the possibility to join Caltech as a "Visitor in Aeronautics" during this period. This stay would not have been possible without the help of several persons and institutions. First of all I thank my advisor in The Netherlands, Prof. Tijdeman, for his continuing efforts to support me and other students. He made it possible to interrupt my PhD project at the University of Twente for a stay at Caltech. The generous support from the department of Applied Mechanics and the Faculty of Mechanical Engineering enabled a good quality of life in beautiful sunny (?, El Nino) Southern California. In this respect I also thank Prof. Huetink and Prof. Grootenboer.

The work at Caltech was both challenging and rewarding. I thank my colleagues at the Explosion Dynamics Group and my advisor, Prof. Shepherd, for creating a very stimulating and pleasant environment both inside and outside the lab. The work could not have been completed without the help of Raza, Mike and Eric in the Guggenheim sub-basement lab.

This research was sponsored by the Netherlands Organization for Scientific Research (NWO). Their support is gratefully acknowledged.

Pasadena, June 4, 1999

Marco Beltman

Chapter 1

Introduction

1.1 General introduction

At the Aeronautics department of the California Institute of Technology the behaviour of shock waves and detonations is studied. A detonation test tube facility and several shock tube facilities are available for laboratory experiments. During a shock or detonation test, the tube is exposed to high pressures. The detonation or shock wave propagates down the tube and therefore the tube is subjected to a moving pressure load. The problem has a strong dynamic nature. This report deals with the structural response of cylindrical shells to moving pressure loads. The results can be used for the analysis of tube systems, both in industrial and military applications.

1.1.1 Shock tube

Shock tubes are used to investigate shock wave propagation. A shock is created by the driver of the shock tube. The shock wave then travels down the tube at a nearly constant speed. A typical measured pressure history for a point in the tube is given in figure 1.1. The figure shows the measured pressure versus time for a thin aluminium tube in the GALCIT 6 inch shock tube facility. The character of the shock loading is a stepwise varying pressure, advancing at constant speed. Therefore the loading for a shock tube will be represented by a step profile in this report. The load is characterized by the pre-shock pressure p_1, the post-shock pressure p_2 and the velocity v (see figure 1.1)

1.1.2 Detonation tube

A detonation consists of a shock wave and a reaction zone that are tightly coupled. For prompt detonation, at one side of the detonation tube an explosion is initiated by a high explosive. The detonation then travels down the tube at a nearly constant speed: the Chapman-Jouguet velocity. The pressure history for this type of loading can be characterized by the initial pressure p_1, the peak

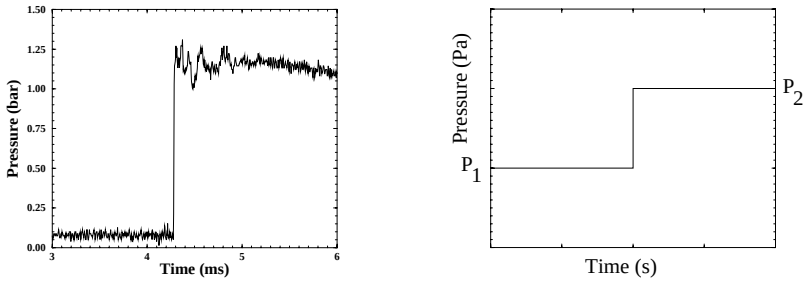

Figure 1.1: Pressure versus time for shock loading

pressure p_2, the final pressure p_∞ and the exponential decay factor T (see figure 1.2).

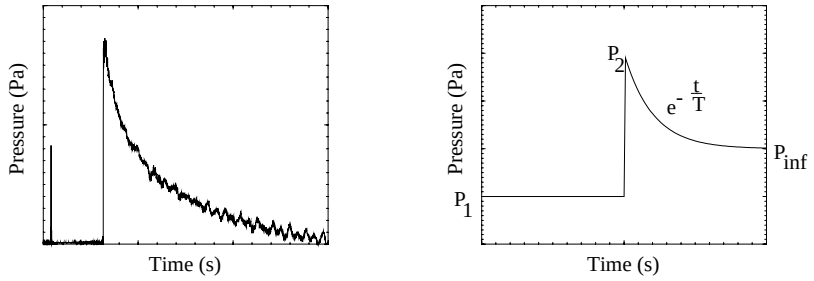

Figure 1.2: Pressure versus time for detonation loading

For the prompt detonation case the pressure loads are well defined. However, the case of deflagration to detonation (DDT) is more complex. In the deflagration to detonation case there intitially is no detonation but only a propagating flame. The flame compresses the unreacted gas ahead of the flame and a spontaneous explosion can occur in this unreacted gas. This can lead to extremely high pressures. However, for a properly operated detonation facility the chance of a DDT event is very low.

1.1.3 Structural response

In figure 1.3 the measured circumferential strain versus time for shock loading of a thin aluminium tube is depicted.

The measured strain shows a sharp peak when the shock passes. For the shock under consideration, the strain exceeds the equivalent static strain by a factor 3. This example indicates that a simple static model of the tube cross

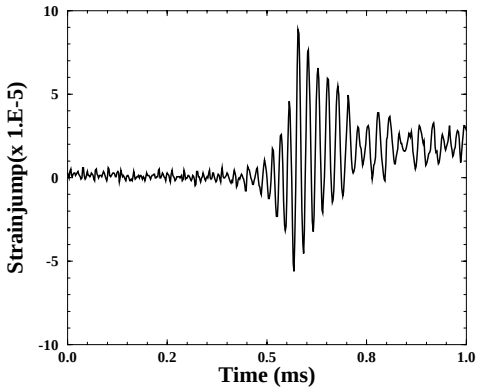

Figure 1.3: Strain history for shock loading

section is not sufficient to predict this large strain. One could calculate the maximum strains and stresses corresponding to the maximum load, but this would result in stresses and strains that are too low. The key question now is: what is the cause of the high strain? A somewhat more sophisticated model takes into account the step character of the loading. However, unfortunately the difference with the simple static cross-sectional model is small, even when the loading is located near a support.

It is now clear that the cause of the high strain is of a dynamic nature. The most simple dynamical model is the dynamical version of the cross-sectional model. This model describes the radial (breathing) motion of the cylinder cross-section. For shock loading, the maximum strain is twice the equivalent static strain. Although significantly higher strains are obtained with this model, it is clear that an essential mechanism is still missing.

Experiments on shock tubes and gun tubes revealed that the speed of propagation of the shock wave is an important parameter. The high strains in the experiments are due to flexural motion of the cylinder wall. Several models were developed to describe this phenomenon, some including for instance rotatory inertia and transverse shear deformation. The flexural models predict the existance of a so-called critical velocity. When the shock travels at the critical speed, the solution for the radial tube motion becomes unbounded. Evidently, damping, non-linearities and plastic deformation will be the controlling mechanisms in this case. Nevertheless, the flexural models are able to predict the high strains that were found in the experiments.

1.2 Formulation of the problem

The main aims of this study are:

- prediction of the structural reponse of a cylindrical tube to shock or detonation loading and comparison with experimental data
- development of design criteria and design methods for tubes that are subjected to shock or detonation loading

Special attention will be paid to the following subjects:

- end effects
  In most models the tube is assumed to be infinite in length. However, in practical situations one deals with short tube sections that are connected by flanges. This will have important implications for the structural response and the design of the tube.
- limits of predictability
  An important issue to keep in mind when developing models and design concepts, is the subject of "limited predictability". Due to variation in the input data, *e.g.* material properties or geometrical properties, there is a degree of uncertainty in the results.

1.3 Outline

This research is carried out in a number of steps. Accordingly, the report is divided into three parts. In part I, the general theory for the structural response of tubes to shock or detonation loading is presented. A number of analytical models is described. These models are not new. However, for the present study they were all rewritten into the same notation in order to put them into perspective. Simple analytical models were developed to describe the transient response of a finite length shell. Finally, in order to describe more complicated boundary conditions, a finite element model was developed.

In part II of this report an analysis is presented for the GALCIT 6 inch shock tube. Results from calculations and experiments are compared for a thin aluminium tube subject to shock loading. The shock tube problem is well defined and the important mechanisms and concepts can be analyzed for this setup.

Finally, an analysis of the detonation tube problem will be described in part III. The detonation tube is a thick walled tube that is constructed of relatively short segments, connected by flanges. Theory and experiments will be used to develop methods in the design process.

Chapter 2

Literature

2.1 Related research fields

The key issue in the shock and detonation problem is the reponse of a structure to a moving load. This problem is related to several other research fields (see figure 2.1):

- vehicle dynamics: the reponse of structures to traffic loads
- interaction between railroad tracks and soil
- structural response of gun tubes
- structural reponse of beam structures to moving loads

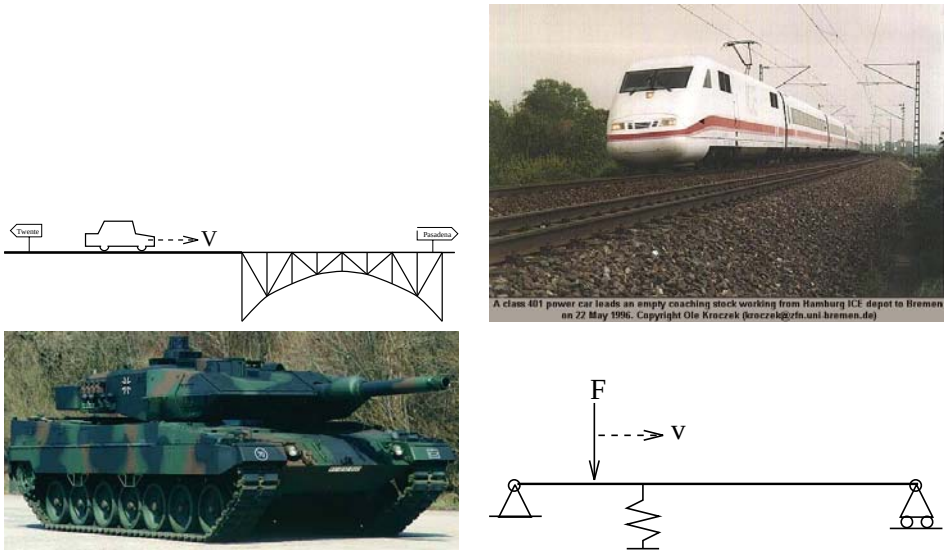

Figure 2.1: Related research topics

2.2 Short literature overview

In the tables 2.1 and 2.2 a short overview of related literature is presented. It is not the intention of the author to present a list with all publications on this subject. For an overview on numerical methods, the reader is referred to Mackerle [1].

Authors	*Ref*	*Year*	*Structure*			*Material*			*Model aspects*				*Loading*			*Solution*						*Remarks*
			Beam	Shell	Plate	Elastic	Plastic	Elasto/plastic	Rot. inertia	Tr. shear	Infinite	Semi-infinite	Moving point	Moving step	Detonation	Steady state	Transient	Analytical	Fourier	Finite element	Other	
Mackerle	[1]	1996																		X	X	Overview paper
Rieker, Lin, Tretheway	[2]	1996	X			X			X	X			X				X			X		Accuracy analysis
Felszeghy	[3]	1996	X			X			X	X	X			X		X			X			Elastic foundation
Felszeghy	[4]	1996	X			X			X	X		X		X			X				X	Elastic foundation Num. integration
Chang, Liu	[5]	1996	X			X							X				X			X		Elastic foundation Nonlinear analysis
Müller, Kryżyński, Ilias	[6]	1995	X			X			X	X	X		X			X			X		X	Periodic structures
Dieterman, Metrikine	[7]	1996	X			X					X		X			X			X			Elastic foundation (halfspace)
Dieterman, Metrikine	[8]	1996	X			X					X		X			X			X			Elastic halfspace Parameter analysis
Pan, Okada, Atluri	[9]	1994			X			X					X	X			X			X	X	Coupled FEM/BEM Plate on soil
Reismann	[10]	1965		X		X					X			X		X		X				Incl. prestress
De Malherbe, Wing, Laderman, Oppenheim	[11]	1966		X		X									X		X	X				Cross section model Experiments
Tang	[12]	1965		X		X			X	X	X	X				X	X		X		X	Finite diff.
Simkins	[13]	1987		X		X					X			X		X		X			X	Thin shell model Thick shell model 3D-elasticity

Table 2.1: Short literature overview

Authors	*Ref*	*Year*	*Structure*			*Material*			*Model aspects*				*Loading*			*Solution*						*Remarks*
			Beam	Shell	Plate	Elastic	Plastic	Elasto/plastic	Rot. inertia	Tr. shear	Infinite	Semi-infinite	Moving point	Moving step	Detonation	Steady state	Transient	Analytical	Fourier	Finite element	Other	
Shepherd	[14]	1992		X		X									X		X	X				Cross section model
Li, Jones	[15]	1994		X			X			X					X		X				X	Num. integration
Bezverkhii, Mukoid	[16]	1994		X		X											X				X	Thick shell model Fin. difference Internal load (not moving)
Remez, Luchko	[17]	1995		X				X									X				X	Thick shell model Blast loading Fin. difference
Olson	[18]	1991		X	X		X										X			X	X	Finite strip model Nonlinear External blast load
Jiang, Olson				X				X									X				X	Finite strip model Nonlinear External blast load
Tenannt, Levine	[19]	1994		X				X									X			X		Cylinder in soil External blast/shock load Nonlinear
Maresca, Millela	[20]	1993						X							X		X					SDOF structural model

Table 2.2: Short literature overview (Continued)

Chapter 3

Cross-sectional model

Consider a cross section of the tube. The tube is exposed to an internal overpressure $p(t)$. The following assumptions are introduced to calculate the tube response:

- rotatory symmetry
- linear elastic theory

The following differential equation governs the structural response of the tube cross section (see appendix A and figure 3.1):

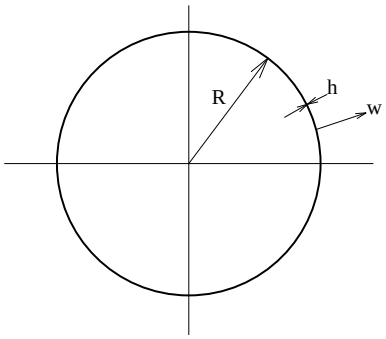

Figure 3.1: Cross sectional model

$$\frac{\partial^2 w}{\partial t^2} + \Omega^2 w = \frac{p(t)}{\rho h} \tag{3.1}$$

where Ω is the frequency corresponding to the radial (breathing) motion:

$$\Omega = \sqrt{\frac{E}{\rho R^2}} \tag{3.2}$$

The displacement is written in a non-dimensional form according to:

$$\overline{w} = \frac{w}{h} \tag{3.3}$$

The basic equation now becomes:

$$\frac{\partial^2 \overline{w}}{\partial t^2} + \Omega^2 \overline{w} = \frac{p\,(t)}{\rho h^2} \tag{3.4}$$

3.1 Static response

In the static case with maximum pressure p_2, the maximum tube response is simply:

$$\overline{w} = \frac{(p_2 - p_{atm})}{\rho h^2 \Omega^2} = \frac{(p_2 - p_{atm})\, R^2}{E h^2} = \Lambda_2 \tag{3.5}$$

where the quantity Λ_2 is defined as:

$$\Lambda_2 = \frac{(p_2 - p_{atm})\, R^2}{E h^2} \tag{3.6}$$

Formula (3.5) is often used in the design of pressure vessels subjected to (quasi) static loading. The maximum pressure is used to determine the dimensions of the tube. However, in the case of shock or detonation loading, the pressure loads are highly transient and propagate at high speeds. In these cases the static design formula can give displacements that are too low, even when a seemingly reasonable safety margin is taken into account.

3.2 Response to shock loading

The dynamic tube response is obtained from:

$$\frac{\partial^2 \overline{w}}{\partial t^2} + \Omega^2 \overline{w} = \frac{p\,(t)}{\rho h^2} \tag{3.7}$$

For simple pressure histories, the tube response can be calculated analytically, for instance using Laplace transform. For the shock tube problem, the pressure history is given by:

$$p\,(t) = \begin{cases} p_1 & \text{for } t \leq 0 \\ p_2 & \text{for } t > 0 \end{cases} \tag{3.8}$$

The response of the tube cross-section to this pressure history is simply:

$$\overline{w} = \begin{cases} \Lambda_1 & \text{for } t \leq 0 \\ \\ \Lambda_1 + (\Lambda_2 - \Lambda_1)\,[1 - \cos(\Omega t)] & \text{for } t > 0 \end{cases} \tag{3.9}$$

The maximum displacement is given by:

$$\overline{w}_{max} = \Lambda_1 + 2\,[\Lambda_2 - \Lambda_1] \tag{3.10}$$

This expressions shows that the maximum displacement, expressed in terms of the maximum static deflection, depends on the loading values p_1 and p_2. It is more convenient to use the difference in deflection to the loads p_1 and p_2 as a reference. The difference in static displacement is:

$$\Delta\overline{w} = (\Lambda_2 - \Lambda_1) \tag{3.11}$$

The maximum difference in dynamic displacement is:

$$\Delta\overline{w}_{max} = 2\,(\Lambda_2 - \Lambda_1) \tag{3.12}$$

The *dynamic amplification factor*, Γ, is now defined as the ratio between these two quantities. For shock loading:

$$\Gamma = 2 \tag{3.13}$$

3.3 Response to detonation loading

For the detonation problem, the pressure history is:

$$p\,(t) = \begin{cases} p_1 & \text{for } t \leq 0 \\ \\ [p_2 - p_\infty]\, e^{-\frac{t}{T}} + p_\infty & \text{for } t > 0 \end{cases} \tag{3.14}$$

The reponse is:

$$\overline{w} = \begin{cases} \Lambda_1 & \text{for } t \leq 0 \\ \\ \Lambda_1 + (\Lambda_\infty - \Lambda_1)\,[1 - \cos(\Omega t)] & \\ \\ + (\Lambda_2 - \Lambda_\infty)\left[\dfrac{\Omega^2 T^2}{1 + \Omega^2 T^2}\right]\left[\dfrac{1}{\Omega T}\sin(\Omega t) - \cos(\Omega t) + e^{-\frac{t}{T}}\right] & \text{for } t > 0 \end{cases} \tag{3.15}$$

The dynamic amplification factor for detonation loading is:

$$\Gamma = max\left\{\frac{\Lambda_\infty - \Lambda_1}{\Lambda_2 - \Lambda_1}\,[1 - \cos(\Omega t)]\right. \tag{3.16}$$

$$\left. + \frac{\Lambda_2 - \Lambda_\infty}{\Lambda_2 - \Lambda_1}\left[\frac{\Omega^2 T^2}{1 + \Omega^2 T^2}\right]\left[\frac{1}{\Omega T}\sin(\Omega t) - \cos(\Omega t) + e^{-\frac{t}{T}}\right]\right\} \tag{3.17}$$

where $max\,\{\}$ denotes the maximum of the expression for $t > 0$. In appendix A, the reponse to a slighty different loading is also given.

Chapter 4

Flexural model: thin infinite shell

4.1 Basic equations

The model is based on the following assumptions:

- rotatory symmetry
- tube of infinite length
- no transverse shear deformation
- no rotatory inertia
- linear elastic theory

Dimensionless quantities and a moving co-ordinate system are introduced according to (see figure 4.1) [1]:

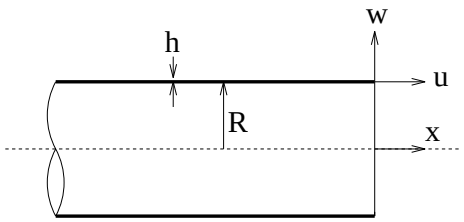

Figure 4.1: Flexural model

$$\overline{u} = \frac{u}{h} \quad ; \quad \overline{w} = \frac{w}{h} \quad ; \quad \overline{\eta} = \frac{\sqrt{12}}{h}\,[x - vt] \tag{4.1}$$

[1] This choice is made is order to enable direct comparison with the other models

The following parameters are used in this model:

$$\begin{aligned}
&\Lambda_i = \frac{(p_i - p_{atm})\, R^2}{Eh^2} && : \text{excitation parameter } (\mathrm{i} = 1, 2 \text{ or } \infty) \\
&v_d = \sqrt{\frac{E}{\rho\,(1-\nu^2)}} && : \text{dilatational wave velocity in a shell} \\
&\beta = \frac{h}{\sqrt{12}R} && : \text{non dimensional shell thickness parameter} \\
&\delta = \frac{N_{xx}\left(1-\nu^2\right)}{Eh} && : \text{prestress parameter}
\end{aligned} \tag{4.2}$$

where N_{xx} is the axial force per unit circumferential length due to prestress effects:

$$N_{xx} = \frac{F_x}{2\pi R} \tag{4.3}$$

Following Reismann [10] and Simkins [13], two additional assumptions are used to simplify the model:

- $\dfrac{v}{v_d} \ll 1$
- $\beta \ll 1$

In this case the differential equation reduces to the well-known form:

$$A_4 \frac{\partial^4 \overline{w}}{\partial \overline{\eta}^4} + A_2 \frac{\partial^2 \overline{w}}{\partial \overline{\eta}^2} + A_0 \overline{w} = F\left(\overline{\eta}\right) \tag{4.4}$$

where:

$$A_4 = 1 \quad ; \quad A_2 = \left[\left(\frac{v}{v_d}\right)^2 - \delta\right] \quad ; \quad A_0 = \beta^2\left(1-\nu^2\right) \tag{4.5}$$

The right hand side of this equation contains loading and prestress terms. For shock loading and detonation loading one has:

$$\text{shock} \;:\; \mathrm{F}\left(\overline{\eta}\right) = \beta^2\left(1-\nu^2\right)\left\{\Lambda_1 + \left(\Lambda_2 - \Lambda_1\right)\left[1 - \mathrm{H}\left(\overline{\eta}\right)\right]\right\} - \frac{\nu\beta\delta}{\sqrt{12}} \tag{4.6}$$

$$\begin{aligned}
\text{detonation} \;:\; \mathrm{F}\left(\overline{\eta}\right) &= \beta^2\left(1-\nu^2\right)\left\{\Lambda_1 + \left(\Lambda_\infty - \Lambda_1\right)\left[1 - H\left(\overline{\eta}\right)\right]\right\} \\
&+ \beta^2\left(1-\nu^2\right)\left\{\left(\Lambda_2 - \Lambda_\infty\right)\left[1 - H\left(\overline{\eta}\right)\right] e^{\frac{\overline{\eta}}{\eta_0}}\right\} \\
&- \frac{\nu\beta\delta}{\sqrt{12}}
\end{aligned} \tag{4.7}$$

where $H\left(\overline{\eta}\right)$ is the step function and $\eta_0 = \dfrac{\sqrt{12}vT}{h}$.

4.2 Dispersion equation

The solution of the differential equation (4.4) is composed of a homogeneous part and a particular part. The characteristic equation for the homogeneous equation determines the relation between the axial wave number $k = \dfrac{\sqrt{12}\alpha}{ih}$ and the shock speed v. Upon assuming for the homogeneous part:

$$\overline{w} = \hat{w}e^{\alpha\overline{\eta}} \tag{4.8}$$

the dispersion equation is:

$$A_4\alpha^4 + A_2\alpha^2 + A_0 = 0 \tag{4.9}$$

The solution is:

$$\alpha^2 = \frac{1}{2\beta^2\left(1-\nu^2\right)}\left[-\left[\left(\frac{v}{v_d}\right)^2 - \delta\right] \pm \sqrt{\left[\left(\frac{v}{v_d}\right)^2 - \delta\right]^2 - 4\beta^2\left(1-\nu^2\right)}\right] \tag{4.10}$$

There are four values of α for each value of v, appearing in pairs of complex conjugates. Depending on the value of v, these values are either complex or purely imaginary. Three cases can be distinguished:

- subcritical: $v < v_{c0}$
  values of α are complex: $\alpha = \pm n \pm im$
- critical: $v = v_{c0}$
  values of α are purely imaginary and equal: $\alpha = \pm im$
- supercritical: $v > v_{c0}$
  values of α are purely imaginary and distinct: $\alpha = \pm im_1$ and $\alpha = \pm im_2$

Evidently, the critical velocity for this model is:

$$v_{c0} = v_d\sqrt{\sqrt{4\beta^2\left(1-\nu^2\right)} + \delta} \tag{4.11}$$

The critical velocity increases when the axial prestress is tensile, and decreases when the axial prestress is compressive. In terms of material and geometrical properties:

$$v_{c0} = \sqrt{\frac{E}{\rho\left(1-\nu^2\right)}}\sqrt{\sqrt{\frac{h^2\left(1-\nu^2\right)}{3R^2}} + \frac{N_{xx}\left(1-\nu^2\right)}{Eh}} \tag{4.12}$$

When no axial prestress is present:

$$v_{c0} = \left[\frac{E^2h^2}{3\rho^2R^2\left(1-\nu^2\right)}\right]^{\frac{1}{4}} \tag{4.13}$$

4.3 Response to shock loading

4.3.1 Subcritical velocities

The solution has to remain bounded for $\overline{\eta} \to \pm\infty$. Furthermore, continuity conditions have to be satisfied at $\overline{\eta} = 0$ for displacement, rotation, moment and shear. A short derivation of the solution is given in appendix B. The result for the displacement $\overline{w}$ in the first region, $\overline{\eta} < 0$, and the second region, $\overline{\eta} \geq 0$ is:

$$\begin{aligned} \overline{w}^I = \Lambda_1^s \quad &- \quad \frac{\nu\beta\delta}{\sqrt{12}A_0} \\ &+ \quad (\Lambda_2^s - \Lambda_1^s)\left\{1 + \frac{1}{8}e^{n\overline{\eta}}\left[-4\cos(m\overline{\eta}) + 2\frac{n^2-m^2}{nm}\sin(m\overline{\eta})\right]\right\} \end{aligned} \tag{4.14}$$

$$\begin{aligned} \overline{w}^{II} = \Lambda_1^s \quad &- \quad \frac{\nu\beta\delta}{\sqrt{12}A_0} \\ &+ \quad (\Lambda_2^s - \Lambda_1^s)\left\{\frac{1}{8}e^{-n\overline{\eta}}\left[4\cos(m\overline{\eta}) + 2\frac{n^2-m^2}{nm}\sin(m\overline{\eta})\right]\right\} \end{aligned} \tag{4.15}$$

where [2]:

$$n = \frac{1}{2}\sqrt{\left(\frac{v_{c0}}{v_d}\right)^2 - \left(\frac{v}{v_d}\right)^2} \quad ; \quad m = \frac{1}{2}\sqrt{\left(\frac{v_{c0}}{v_d}\right)^2 + \left(\frac{v}{v_d}\right)^2} \tag{4.16}$$

$$\Lambda_i^s = \frac{\beta^2\left(1-\nu^2\right)}{A_0}\Lambda_i = \Lambda_i \tag{4.17}$$

The maximum amplitude occurs in region I, behind the pressure step. The dynamic amplification factor for this case is:

$$\Gamma = 1 + \frac{1}{2}e^{n\overline{\eta}_{max}}\left[-\frac{n}{\sqrt{n^2+m^2}} + \left(\frac{n^2-m^2}{2nm}\right)\frac{m}{\sqrt{n^2+m^2}}\right] \tag{4.18}$$

where $\overline{\eta}_{max}$ is the first solution for $\overline{\eta} < 0$ of:

$$\tan(m\overline{\eta}) = \frac{m}{n} \tag{4.19}$$

Note that the initial displacement due to the load p_1 does not affect the dynamic amplification factor, since this displacement is of a static nature. The axial prestress does not appear directly in expression (4.18). However, the axial prestress affects the dispersion equation and the values of n, m, and v_{c0}.

4.3.2 Critical velocity

The solution for this case can not be determined. In fact, as v approaches v_{c0}, the values for the displacement become unbounded for the sub and supercritical case: $n \to 0$ or $m_1 \to m_2$.

[2] Λ_i^s is introcuded to enable easy comparison with the model including shear deformation and rotatory inertia

4.3.3 Supercritical velocities

Due to the fact that the characteristic roots are purely imaginary, the solution is bounded for $\overline{\eta} \to \pm\infty$. In this case another condition is used to determine the solution. Energy has to flow away from the pressure step. Energy is transported at the group speed, v_g. In region II, ahead of the pressure step, the group speed has to exceed the phase speed. In region I, the phase speed of the waves should exceed the group speed. Furthermore, continuity conditions have to be satisfied at $\overline{\eta} = 0$ for displacement, rotation, moment and shear. A short derivation of the solution is given in appendix B. The results for the displacement $\overline{w}$ in the first and second region is:

$$\overline{w}^I = \Lambda_1^s - \frac{\nu\beta\delta}{\sqrt{12}A_0} + (\Lambda_2^s - \Lambda_1^s)\left\{1 + \left[\frac{m_2^2}{m_1^2 - m_2^2}\right]\cos(m_1\overline{\eta})\right\} \tag{4.20}$$

$$\overline{w}^{II} = \Lambda_1^s - \frac{\nu\beta\delta}{\sqrt{12}A_0} + (\Lambda_2^s - \Lambda_1^s)\left\{\left[\frac{m_1^2}{m_1^2 - m_2^2}\right]\cos(m_2\overline{\eta})\right\} \tag{4.21}$$

where:

$$m_1 = \frac{1}{2}\left[\sqrt{\left(\frac{v}{v_d}\right)^2 + \left(\frac{v_{c0}}{v_d}\right)^2} - \sqrt{\left(\frac{v}{v_d}\right)^2 - \left(\frac{v_{c0}}{v_d}\right)^2}\right]$$

$$m_2 = \frac{1}{2}\left[\sqrt{\left(\frac{v}{v_d}\right)^2 + \left(\frac{v_{c0}}{v_d}\right)^2} + \sqrt{\left(\frac{v}{v_d}\right)^2 - \left(\frac{v_{c0}}{v_d}\right)^2}\right] \tag{4.22}$$

The dynamic amplification factor for supercritical velocities is:

$$\Gamma = 1 - \left[\frac{m_2^2}{m_1^2 - m_2^2}\right] \tag{4.23}$$

4.4 Response to detonation loading

4.4.1 Subcritical velocities

The solution for subcritical velocities is:

$$\begin{aligned}
\overline{w}^{I} &= \Lambda_1^s - \frac{\nu\beta\delta}{\sqrt{12}A_0} \\
&+ \left(\Lambda_\infty^s - \Lambda_1^s\right)\left\{1 + \frac{1}{8}e^{n\overline{\eta}}\left[-4\cos\left(m\overline{\eta}\right) + 2\frac{n^2-m^2}{nm}\sin\left(m\overline{\eta}\right)\right]\right\} \\
&+ \left(\Lambda_2^d - \Lambda_\infty^d\right)e^{\frac{\overline{\eta}}{\overline{\eta}_0}} \\
&+ \left(\Lambda_2^d - \Lambda_\infty^d\right)\frac{1}{4}e^{n\overline{\eta}}\left\{\left[-2 + \left(\frac{1}{\overline{\eta}_0}\right)\frac{m^2-3n^2}{n\left(n^2+m^2\right)} + \left(\frac{1}{\overline{\eta}_0}\right)^3\frac{1}{n\left(n^2+m^2\right)}\right]\cos\left(m\overline{\eta}\right)\right. \\
&+ \left.\left[\frac{n^2-m^2}{mn} + \left(\frac{1}{\overline{\eta}_0}\right)\frac{n^2-3m^2}{m\left(n^2+m^2\right)} - \left(\frac{1}{\overline{\eta}_0}\right)^2\frac{1}{mn} - \left(\frac{1}{\overline{\eta}_0}\right)^3\frac{1}{m\left(n^2+m^2\right)}\right]\sin\left(m\overline{\eta}\right)\right\}
\end{aligned} \tag{4.24}$$

$$\begin{aligned}
\overline{w}^{II} &= \Lambda_1^s - \frac{\nu\beta\delta}{\sqrt{12}A_0} \\
&+ \left(\Lambda_\infty^s - \Lambda_1^s\right)\left\{\frac{1}{8}e^{-n\overline{\eta}}\left[4\cos\left(m\overline{\eta}\right) + 2\frac{n^2-m^2}{nm}\sin\left(m\overline{\eta}\right)\right]\right\} \\
&+ \left(\Lambda_2^d - \Lambda_\infty^d\right)\frac{1}{4}e^{-n\overline{\eta}}\left\{\left[2 + \left(\frac{1}{\overline{\eta}_0}\right)\frac{m^2-3n^2}{n\left(n^2+m^2\right)} + \left(\frac{1}{\overline{\eta}_0}\right)^3\frac{1}{n\left(n^2+m^2\right)}\right]\cos\left(m\overline{\eta}\right)\right. \\
&+ \left.\left[\frac{n^2-m^2}{mn} - \left(\frac{1}{\overline{\eta}_0}\right)\frac{n^2-3m^2}{m\left(n^2+m^2\right)} - \left(\frac{1}{\overline{\eta}_0}\right)^2\frac{1}{mn} + \left(\frac{1}{\overline{\eta}_0}\right)^3\frac{1}{m\left(n^2+m^2\right)}\right]\sin\left(m\overline{\eta}\right)\right\}
\end{aligned}$$

where:

$$\Lambda_i^d = \frac{\beta^2\left(1-\nu^2\right)}{A_4\left(\frac{1}{\overline{\eta}_0}\right)^4 + A_2\left(\frac{1}{\overline{\eta}_0}\right)^2 + A_0}\Lambda_i \tag{4.25}$$

4.4.2 Critical velocity

The solution of the problem can not be obtained when the velocity is equal to the critical velocity. The solution becomes unbounded when the velocity approaches the critical value.

4.4.3 Supercritical velocities

The solution for the supercritical case is:

$$\overline{w}^{I} = \Lambda_1^s - \frac{\nu\beta\delta}{\sqrt{12}A_0} \tag{4.26}$$

$$
\begin{aligned}
&+ \quad (\Lambda_\infty^s - \Lambda_1^s)\left\{1 + \left[\frac{m_2^2}{m_1^2 - m_2^2}\right]\cos(m_1\overline{\eta})\right\} \\
&+ \quad \left(\Lambda_2^d - \Lambda_\infty^d\right) e^{\frac{\overline{\eta}}{\overline{\eta}_0}} \\
&+ \quad \left(\Lambda_2^d - \Lambda_\infty^d\right) \frac{1}{m_1 m_2\left(m_1^2 - m_2^2\right)}\left\{m_1 m_2\left[m_2^2 + \left(\frac{1}{\overline{\eta}_0}\right)^2\right]\cos(m_1\overline{\eta})\right. \\
&+ \quad \left. m_2\left(\frac{1}{\overline{\eta}_0}\right)\left[m_2^2 - \left(\frac{1}{\overline{\eta}_0}\right)^2\right]\sin(m_1\overline{\eta})\right\}
\end{aligned}
$$

$$
\begin{aligned}
\overline{w}^{II} &= \Lambda_1^s - \frac{\nu\beta\delta}{\sqrt{12}A_0} \qquad (4.27) \\
&+ \quad (\Lambda_\infty^s - \Lambda_1^s)\left\{\left[\frac{m_1^2}{m_1^2 - m_2^2}\right]\cos(m_2\overline{\eta})\right\} \\
&+ \quad \left(\Lambda_2^d - \Lambda_\infty^d\right) \frac{1}{m_1 m_2\left(m_1^2 - m_2^2\right)}\left\{m_1 m_2\left[m_2^2 + \left(\frac{1}{\overline{\eta}_0}\right)^2\right]\cos(m_2\overline{\eta})\right. \\
&- \quad \left. m_1\left(\frac{1}{\overline{\eta}_0}\right)\left[m_1^2 + \left(\frac{1}{\overline{\eta}_0}\right)^2\right]\sin(m_2\overline{\eta})\right\} \qquad (4.28)
\end{aligned}
$$

4.5 Response to arbitrary loading

In the sections 4.3 and 4.4 the response of the shell to shock and detonation loading was described analytically. It is possible to develop a model for the description of the response to arbitrary loading profiles. Consider a loading profile that is made up of different intervals (see figure 4.2). In each interval, the loading is described by a function $F(\overline{\eta})$. The loading pattern propagates down the tube at a constant velocity v. The tube is assumed to be infinite in length.

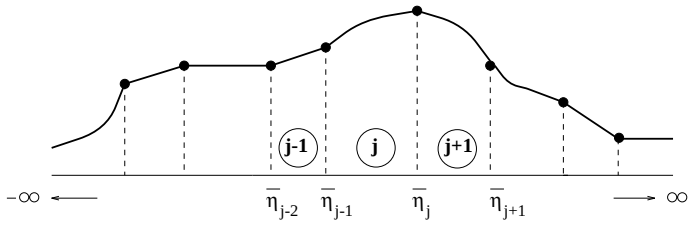

Figure 4.2: Arbitrary loading profile

For the calculation of the response, the tube is divided in intervals. Interval j covers the range $\left[\overline{\eta}_{j-1}, \overline{\eta}_j\right]$. For the intervals $j-1$ and j the general solution can be written as:

$$\overline{w}^{j-1} = C_1^{j-1} e^{\alpha_1 \overline{\eta}} + C_2^{j-1} e^{\alpha_2 \overline{\eta}} + C_3^{j-1} e^{\alpha_3 \overline{\eta}} + C_4^{j-1} e^{\alpha_4 \overline{\eta}} + \overline{w}_p^{j-1} - \frac{\nu\beta\delta}{\sqrt{12}A_0} \quad (4.29)$$

$$\overline{w}^{j} = C_1^{j} e^{\alpha_1 \overline{\eta}} + C_2^{j} e^{\alpha_2 \overline{\eta}} + C_3^{j} e^{\alpha_3 \overline{\eta}} + C_4^{j} e^{\alpha_4 \overline{\eta}} + \overline{w}_p^{j} - \frac{\nu\beta\delta}{\sqrt{12}A_0} \quad (4.30)$$

where the roots $\alpha_1, \alpha_2, \alpha_3$ and α_4 can be calculated from the dispersion equation and $\overline{w}_p^j$ is a particular solution for interval j due to the pressure loading. Next, the continuity conditions have to be satisfied for each interface. For the intervals $j-1$ and j this gives the following matrix-vector expression:

$$\left[A\left(\overline{\eta}_{j-1}\right)\right]\left\{C^{j-1}\right\} + \left\{\overline{W}_p^{j-1}\left(\overline{\eta}_{j-1}\right)\right\} = \left[A\left(\overline{\eta}_{j-1}\right)\right]\left\{C^{j}\right\} + \left\{\overline{W}_p^{j-1}\left(\overline{\eta}_{j}\right)\right\} \quad (4.31)$$

where:

$$\left[A\left(\overline{\eta}_{j-1}\right)\right] = \begin{bmatrix} e^{\alpha_1\overline{\eta}_{j-1}} & e^{\alpha_2\overline{\eta}_{j-1}} & e^{\alpha_3\overline{\eta}_{j-1}} & e^{\alpha_4\overline{\eta}_{j-1}} \\ \alpha_1 e^{\alpha_1\overline{\eta}_{j-1}} & \alpha_2 e^{\alpha_2\overline{\eta}_{j-1}} & \alpha_3 e^{\alpha_3\overline{\eta}_{j-1}} & \alpha_4 e^{\alpha_4\overline{\eta}_{j-1}} \\ (\alpha_1)^2 e^{\alpha_1\overline{\eta}_{j-1}} & (\alpha_2)^2 e^{\alpha_2\overline{\eta}_{j-1}} & (\alpha_3)^2 e^{\alpha_3\overline{\eta}_{j-1}} & (\alpha_4)^2 e^{\alpha_4\overline{\eta}_{j-1}} \\ (\alpha_1)^3 e^{\alpha_1\overline{\eta}_{j-1}} & (\alpha_2)^3 e^{\alpha_2\overline{\eta}_{j-1}} & (\alpha_3)^3 e^{\alpha_3\overline{\eta}_{j-1}} & (\alpha_4)^3 e^{\alpha_4\overline{\eta}_{j-1}} \end{bmatrix} \quad (4.32)$$

$$\left\{C^{j-1}\right\} = \left\{\begin{array}{c} C_1^{j-1} \\ C_2^{j-1} \\ C_3^{j-1} \\ C_4^{j-1} \end{array}\right\} \tag{4.33}$$

$$\left\{\overline{W}_p^{j-1}\left(\overline{\eta}_{j-1}\right)\right\} = \left\{\begin{array}{c} \overline{w}_p^{j-1}\left(\overline{\eta}_{j-1}\right) \\ \frac{\partial \overline{w}_p^{j-1}}{\partial \overline{\eta}}\Big|_{\overline{\eta}_{j-1}} \\ \frac{\partial^2 \overline{w}_p^{j-1}}{\partial \overline{\eta}^2}\Big|_{\overline{\eta}_{j-1}} \\ \frac{\partial^3 \overline{w}_p^{j-1}}{\partial \overline{\eta}^3}\Big|_{\overline{\eta}_{j-1}} \end{array}\right\} \tag{4.34}$$

Successively applying this relation gives the following relation between the constants in the first interval and the last interval:

$$\{C^n\} = \left\{C^1\right\} + \sum_{j=1}^{n-1} \left[A\left(\overline{\eta}_j\right)\right]^{-1} \left[\left\{\overline{W}_p^j\left(\overline{\eta}_j\right)\right\} - \left\{\overline{W}_p^{j+1}\left(\overline{\eta}_j\right)\right\}\right] \tag{4.35}$$

When the values of 4 constants are known, all other constants can be calculated. The boundary conditions for $\overline{\eta} \pm \infty$ still have to be satisfied. Based on "boundedness" of the solution or the group velocity concept, 4 constants can be eliminated. The other constants can then be determined from expression (4.35). Thus, the total solution of the problem is obtained.

4.6 Damping

In order to account for damping effects, a damping term can be added to the differential equation (see Appendix C). In general, the damping term causes the characteristic roots to be complex for all velocities. The characteristic roots can be determined with straightforward procedures for polynomials.

As in most structural dynamics problems, the estimation and prediction of damping is difficult. The question remains how to determine the value of the damping constant that is used in the model. A theoretical prediction of the damping constant for detonation and shock tubes is very difficult. The damping depends on for instance the clamping conditions and the use of rubber rings. The quantitative predictability of the damping is therefore not very good. However, there is a way to determine the order of magnitude of the damping constant at least. By measuring the modal properties of the tube or a tube section, one can make an estimation of the amount of damping in the system. In appendix C a short description of the damping model is given.

Chapter 5

Flexural model: thin infinite shell including rotatory inertia and shear deformation

5.1 Basic equations

The model is based on the following assumptions, see *e.g.* Tang [12]:

- rotatory symmetry
- tube of infinite length
- linear elastic theory
- no axial prestress

Dimensionless quantities and a moving co-ordinate system are introduced according to (see figure 5.1):

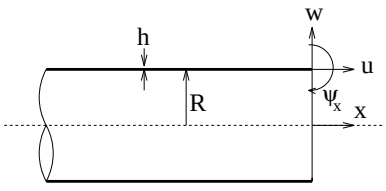

Figure 5.1: Flexural model including shear and rotatory inertia

$$\overline{u} = \frac{u}{h} \quad ; \quad \overline{w} = \frac{w}{h}$$

$$\overline{\eta} = \frac{\sqrt{12}}{h}\left[x - vt\right] \quad ; \quad \overline{\psi}_x = \frac{1}{\sqrt{12}}\psi_x \tag{5.1}$$

$$\tag{5.2}$$

The displacement is split up into two parts:

$$\overline{w} = \overline{w}_b + \overline{w}_s \quad ; \quad \overline{\psi}_x = -\frac{\partial \overline{w}_b}{\partial \overline{\eta}} \tag{5.3}$$

The following parameters are used in this model:

$$\begin{aligned}
&\Lambda_i = \frac{\left(p_i - p_{atm}\right) R^2}{Eh^2} && \text{: excitation parameter} \\
&v_d = \sqrt{\frac{E}{\rho\left(1-\nu^2\right)}} && \text{: dilatational wave velocity in a shell} \\
&v_s = \sqrt{\frac{\kappa G}{\rho}} && \text{: shear wave velocity in a shell} \\
&\beta = \frac{h}{\sqrt{12}R} && \text{: non dimensional shell thickness parameter}
\end{aligned} \tag{5.4}$$

The following equations are obtained (see appendix D):

$$\overline{w}_s = -\left(\frac{v_d}{v_s}\right)^2 \left[1 - \left(\frac{v}{v_d}\right)^2\right] \frac{\partial^2 \overline{w}_b}{\partial \overline{\eta}^2} \tag{5.5}$$

$$\frac{\partial \overline{u}}{\partial \overline{\eta}} = \frac{\nu\beta}{\left[\left(\frac{v}{v_d}\right)^2 - 1\right]} \left[\overline{w}_b + \overline{w}_s\right] \tag{5.6}$$

The final result for this model is the following differential equation:

$$A_4 \frac{\partial^4 \overline{w}_b}{\partial \overline{\eta}^4} + A_2 \frac{\partial^2 \overline{w}_b}{\partial \overline{\eta}^2} + A_0 \overline{w}_b = F\left(\overline{\eta}\right) \tag{5.7}$$

where:

$$\begin{aligned}
A_4 &= \left[\left(\frac{v}{v_d}\right)^2 - 1\right]\left[\left(\frac{v}{v_s}\right)^2 - 1\right] \\
A_2 &= \left(\frac{v}{v_d}\right)^2 \left[1 + \beta^2 \left(\frac{v_d}{v_s}\right)^2\right] - \beta^2\left(1-\nu^2\right)\left(\frac{v_d}{v_s}\right)^2
\end{aligned} \tag{5.8}$$

$$A_0 = \beta^2 \left[1 + \frac{\nu^2}{\left[\left(\frac{v}{v_d} \right)^2 - 1 \right]} \right]$$

$$\text{shock} : \mathrm{F}(\overline{\eta}) = \beta^2 \left(1 - \nu^2\right) \left\{ \Lambda_1 + (\Lambda_2 - \Lambda_1) \left[1 - H(\overline{\eta}) \right] \right\}$$

$$\begin{aligned} \text{detonation} : \mathrm{F}(\overline{\eta}) &= \beta^2 \left(1 - \nu^2\right) \left\{ \Lambda_1 + (\Lambda_\infty - \Lambda_1) \left[1 - H(\overline{\eta}) \right] \right\} \\ &+ \beta^2 \left(1 - \nu^2\right) \left\{ (\Lambda_2 - \Lambda_\infty) \left[1 - H(\overline{\eta}) \right] e^{\frac{\overline{\eta}}{\eta_0}} \right\} \end{aligned}$$

Note that the differential equation shows a strong resemblance with the differential equation for the thin shell model. In fact, upon taking $v_s \to \infty$ and $\frac{v}{v_d} \ll 1$, the model degenerates to the thin shell model.

5.2 Dispersion equation

The dispersion equation for this model is:

$$A_4 \ \alpha^4 + A_2 \ \alpha^2 + A_0 = 0 \tag{5.9}$$

where α is related to the wave number k through:

$$k = \frac{\sqrt{12}\alpha}{ih} \tag{5.10}$$

The values of the characteristic roots for each value of v can be determined with straightforward procedures for polynomials. No closed-form solution will be used in the present report. Five cases can be distinguished:

- case 1: $v < v_{c0}$
  values of α are complex: $\alpha = \pm n \pm im$
- case 2: $v_{c0} < v < v_{c1}$
  values of α are purely imaginary: $\alpha = \pm im_1$ and $\alpha = \pm im_2$
- case 3: $v_{c1} < v < v_{c2}$
  values of α are real or imaginary: $\alpha = \pm n$ and $\alpha = \pm im$
- case 4: $v_{c2} < v < v_{c3}$
  values of α are purely real: $\alpha = \pm n_1$ and $\alpha = \pm n_2$
- case 5: $v_{c3} < v$
  values of α are purely imaginary: $\alpha = \pm im_1$ and $\alpha = \pm im_2$

In this model there are four "critical velocities". The velocities are:

- v_{c0}
  the characteristic roots are found from:

$$\alpha^2 = \frac{1}{2}\left[-A_2 \pm \sqrt{{A_2}^2 - 4A_0A_4}\right]$$

  The critical velocity v_{c0} can now be calculated from:

$$A_2^2 - 4A_0A_4 = 0$$

- $v_{c1} = v_s$
  shear wave speed
- $v_{c2} = v_d\sqrt{1-\nu^2}$
  dilatational wave speed in a bar
- $v_{c3} = v_d$
  dilatational wave speed

When the shock speed is equal to one of the critical velocities, a solution for the problem can not be obtained.

5.3 Response to shock loading

A short derivation of the solution is given in appendix D.

5.3.1 Case 1: $0 < v < v_{c0}$

$$\overline{w}_b^I = \Lambda_1^s + (\Lambda_2^s - \Lambda_1^s)\left\{1 + \frac{1}{8}e^{n\overline{\eta}}\left[-4\cos(m\overline{\eta}) + 2\frac{n^2-m^2}{nm}\sin(m\overline{\eta})\right]\right\} \quad (5.11)$$

$$\overline{w}_b^{II} = \Lambda_1^s + (\Lambda_2^s - \Lambda_1^s)\left\{\frac{1}{8}e^{-n\overline{\eta}}\left[4\cos(m\overline{\eta}) + 2\frac{n^2-m^2}{nm}\sin(m\overline{\eta})\right]\right\} \quad (5.12)$$

where [1]:

$$\Lambda_i^s = \frac{\beta^2\left(1-\nu^2\right)}{A_0}\Lambda_i \quad (5.13)$$

The displacement $\overline{w}_s$ follows from expression (D.7) and the axial displacement follows directly from expression (D.8). The total radial deflection is then simply $\overline{w} = \overline{w}_b + \overline{w}_s$. The maximum displacement, $\overline{w}_{max}$, is obtained for $\overline{\eta}_{max}$. It is the first solution for $\overline{\eta} < 0$ of:

$$\tan(m\overline{\eta}) = \frac{m}{n} \quad (5.14)$$

The dynamic amplification factor can then be calculated from:

$$\Gamma = \frac{1}{\Lambda_2 - \Lambda_1}\left[\overline{w}_{max} - \Lambda_1^s\right] \quad (5.15)$$

[1] For $\frac{v}{v_d} \ll 1$: $\Lambda_i^s = \Lambda_i$

5.3.2 Case 2: $v_{c0} < v < v_{c1}$

$$\overline{w}_b^I = \Lambda_1^s + (\Lambda_2^s - \Lambda_1^s)\left\{1 + \left[\frac{m_2^2}{m_1^2 - m_2^2}\right]\cos(m_1\overline{\eta})\right\} \tag{5.16}$$

$$\overline{w}_b^{II} = \Lambda_1^s + (\Lambda_2^s - \Lambda_1^s)\left[\frac{m_1^2}{m_1^2 - m_2^2}\right]\cos(m_2\overline{\eta}) \tag{5.17}$$

The maximum amplitude is:

$$\overline{w}_{max} = \Lambda_1^s + (\Lambda_2^s - \Lambda_1^s)\left\{1 - \left[1 + m_1^2\left(\frac{v_d}{v_s}\right)^2\left[1 - \left(\frac{v}{v_d}\right)^2\right]\right]\left[\frac{m_2^2}{m_1^2 - m_2^2}\right]\right\} \tag{5.18}$$

The dynamic amplification factor is:

$$\Gamma = \left[\frac{\Lambda_2^s - \Lambda_1^s}{\Lambda_2 - \Lambda_1}\right]\left\{1 - \left[1 + m_1^2\left(\frac{v_d}{v_s}\right)^2\left[1 - \left(\frac{v}{v_d}\right)^2\right]\right]\left[\frac{m_2^2}{m_1^2 - m_2^2}\right]\right\} \tag{5.19}$$

5.3.3 Case 3: $v_{c1} < v < v_{c2}$

$$\overline{w}_b^I = \Lambda_1^s + (\Lambda_2^s - \Lambda_1^s)\left\{1 - \left[\frac{1}{n^2 + m^2}\right]\left[\frac{1}{2}m^2 e^{n\overline{\eta}} + n^2\cos(m\overline{\eta})\right]\right\} \tag{5.20}$$

$$\overline{w}_b^{II} = \Lambda_1^s + (\Lambda_2^s - \Lambda_1^s)\left[\frac{1}{n^2 + m^2}\right]\frac{1}{2}m^2 e^{-n\overline{\eta}} \tag{5.21}$$

5.3.4 Case 4: $v_{c2} < v < v_{c3}$

$$\overline{w}_b^I = \Lambda_1^s + (\Lambda_2^s - \Lambda_1^s)\left\{1 + \frac{1}{2}\left[\frac{1}{n_1^2 - n_2^2}\right]\left[n_2^2 e^{n_1\overline{\eta}} - n_1^2 e^{n_2\overline{\eta}}\right]\right\} \tag{5.22}$$

$$\overline{w}_b^{II} = \Lambda_1^s + (\Lambda_2^s - \Lambda_1^s)\left\{-\frac{1}{2}\left[\frac{1}{n_1^2 - n_2^2}\right]\left[n_2^2 e^{-n_1\overline{\eta}} - n_1^2 e^{-n_2\overline{\eta}}\right]\right\} \tag{5.23}$$

5.3.5 Case 5: $v_{c3} < v$

$$\overline{w}_b^I = \Lambda_1^s + (\Lambda_2^s - \Lambda_1^s)\left\{1 + \left[\frac{1}{m_1^2 - m_2^2}\right]\left[m_2^2\cos(m_1\overline{\eta}) - m_1^2\cos(m_2\overline{\eta})\right]\right\} \tag{5.24}$$

$$\overline{w}_b^{II} = 0 \tag{5.25}$$

The last result shows that there are no waves ahead of the pressure front when the shock speed exceeds the dilatational wave speed.

5.4 Response to detonation loading

A short derivation of the solution is given in appendix D. Note that for $\frac{v}{vd} \ll 1$, $\Lambda_2^d = \Lambda_1^d$ and $\overline{\eta}_0 \to \infty$, the solution of the detonation model reduces to the solution of the shock problem.

5.4.1 Case 1: $0 < v < v_{c0}$

$$\begin{aligned}
\overline{w}_b^I &= \Lambda_1^s + (\Lambda_\infty^s - \Lambda_1^s)\left\{1 + \frac{1}{8}e^{n\overline{\eta}}\left[-4\cos(m\overline{\eta}) + 2\frac{n^2-m^2}{nm}\sin(m\overline{\eta})\right]\right\} \\
&+ \left(\Lambda_2^d - \Lambda_\infty^d\right)e^{\frac{\overline{\eta}}{\overline{\eta}_0}} \\
&+ \left(\Lambda_2^d - \Lambda_\infty^d\right)\frac{1}{4}e^{n\overline{\eta}}\left\{\left[-2 + \left(\frac{1}{\overline{\eta}_0}\right)\frac{m^2-3n^2}{n\left(n^2+m^2\right)} + \left(\frac{1}{\overline{\eta}_0}\right)^3\frac{1}{n\left(n^2+m^2\right)}\right]\cos(m\overline{\eta})\right. \\
&+ \left.\left[\frac{n^2-m^2}{mn} + \left(\frac{1}{\overline{\eta}_0}\right)\frac{n^2-3m^2}{m\left(n^2+m^2\right)} - \left(\frac{1}{\overline{\eta}_0}\right)^2\frac{1}{mn} - \left(\frac{1}{\overline{\eta}_0}\right)^3\frac{1}{m\left(n^2+m^2\right)}\right]\sin(m\overline{\eta})\right\}
\end{aligned} \tag{5.26}$$

$$\begin{aligned}
\overline{w}_b^{II} &= \Lambda_1^s + (\Lambda_\infty^s - \Lambda_1^s)\left\{\frac{1}{8}e^{-n\overline{\eta}}\left[4\cos(m\overline{\eta}) + 2\frac{n^2-m^2}{nm}\sin(m\overline{\eta})\right]\right\} \\
&+ \left(\Lambda_2^d - \Lambda_\infty^d\right)\frac{1}{4}e^{-n\overline{\eta}}\left\{\left[2 + \left(\frac{1}{\overline{\eta}_0}\right)\frac{m^2-3n^2}{n\left(n^2+m^2\right)} + \left(\frac{1}{\overline{\eta}_0}\right)^3\frac{1}{n\left(n^2+m^2\right)}\right]\cos(m\overline{\eta})\right. \\
&+ \left.\left[\frac{n^2-m^2}{mn} - \left(\frac{1}{\overline{\eta}_0}\right)\frac{n^2-3m^2}{m\left(n^2+m^2\right)} - \left(\frac{1}{\overline{\eta}_0}\right)^2\frac{1}{mn} + \left(\frac{1}{\overline{\eta}_0}\right)^3\frac{1}{m\left(n^2+m^2\right)}\right]\sin(m\overline{\eta})\right\}
\end{aligned} \tag{5.27}$$

where [2]:

$$\Lambda_i^d = \frac{\beta^2\left(1-\nu^2\right)}{A_4\left(\frac{1}{\overline{\eta}_0}\right)^4 + A_2\left(\frac{1}{\overline{\eta}_0}\right)^2 + A_0}\Lambda_i \tag{5.28}$$

5.4.2 Case 2: $v_{c0} < v < v_{c1}$

$$\begin{aligned}
\overline{w}_b^I &= \Lambda_1^s + (\Lambda_\infty^s - \Lambda_1^s)\left\{1 + \left[\frac{m_2^2}{m_1^2 - m_2^2}\right]\cos(m_1\overline{\eta})\right\} \\
&+ \left(\Lambda_2^d - \Lambda_\infty^d\right)e^{\frac{\overline{\eta}}{\overline{\eta}_0}} \\
&+ \left(\Lambda_2^d - \Lambda_\infty^d\right)\left[\frac{1}{m_1 m_2\left(m_1^2 - m_2^2\right)}\right]\left\{m_1 m_2\left[m_2^2 + \left(\frac{1}{\overline{\eta}_0}\right)^2\right]\cos(m_1\overline{\eta})\right. \\
&+ \left. m_2\left(\frac{1}{\overline{\eta}_0}\right)\left[m_2^2 - \left(\frac{1}{\overline{\eta}_0}\right)^2\right]\sin(m_1\overline{\eta})\right\}
\end{aligned} \tag{5.29}$$

$$\overline{w}_b^{II} = \Lambda_1^s + (\Lambda_\infty^s - \Lambda_1^s)\left[\frac{m_1^2}{m_1^2 - m_2^2}\right]\cos(m_2\overline{\eta}) \tag{5.30}$$

[2] For $\frac{v}{v_d} \ll 1$ and $\overline{\eta}_0 \to \infty$: $\Lambda_i^d = \Lambda_i$

$$
\begin{aligned}
&+ \quad \left(\Lambda_2^d - \Lambda_\infty^d\right)\left[\frac{1}{m_1 m_2\left(m_1^2 - m_2^2\right)}\right]\left\{m_1 m_2\left[m_2^2 + \left(\frac{1}{\overline{\eta}_0}\right)^2\right]\cos\left(m_2\overline{\eta}\right)\right. \\
&- \quad \left. m_1\left(\frac{1}{\overline{\eta}_0}\right)\left[m_1^2 + \left(\frac{1}{\overline{\eta}_0}\right)^2\right]\sin\left(m_2\overline{\eta}\right)\right\}
\end{aligned}
$$

5.4.3 Case 3: $v_{c1} < v < v_{c2}$

$$
\begin{aligned}
\overline{w}_b^I &= \Lambda_1^s + \left(\Lambda_\infty^s - \Lambda_1^s\right)\left\{1 - \left[\frac{1}{n^2+m^2}\right]\left[\frac{1}{2}m^2 e^{n\overline{\eta}} + n^2\cos\left(m\overline{\eta}\right)\right]\right\} \\
&+ \left(\Lambda_2^d - \Lambda_\infty^d\right)e^{\frac{\overline{\eta}}{\overline{\eta}_0}} \qquad (5.31) \\
&+ \left(\Lambda_2^d - \Lambda_\infty^d\right)\left[\frac{1}{nm\left(n^2+m^2\right)}\right]\left\{-\frac{1}{2}m\left[+nm^2 + \left(\frac{1}{\overline{\eta}_0}\right)m^2 + \left(\frac{1}{\overline{\eta}_0}\right)^2 n + \left(\frac{1}{\overline{\eta}_0}\right)^3\right]e^{n\overline{\eta}}\right. \\
&+ \left. nm\left[-m^2 + \left(\frac{1}{\overline{\eta}_0}\right)^2\right]\cos\left(m\overline{\eta}\right) + \left(\frac{1}{\overline{\eta}_0}\right)n\left[-n^2 + \left(\frac{1}{\overline{\eta}_0}\right)^2\right]\sin\left(m\overline{\eta}\right)\right\}
\end{aligned}
$$

$$
\begin{aligned}
\overline{w}_b^{II} &= \Lambda_1^s + \left(\Lambda_\infty^s - \Lambda_1^s\right)\left[\frac{1}{n^2+m^2}\right]\frac{1}{2}m^2 e^{-n\overline{\eta}} \qquad (5.32) \\
&+ \left(\Lambda_2^d - \Lambda_\infty^d\right)\left[\frac{1}{nm\left(n^2+m^2\right)}\right]\left\{-\frac{1}{2}m\left[-nm^2 + \left(\frac{1}{\overline{\eta}_0}\right)m^2 - \left(\frac{1}{\overline{\eta}_0}\right)^2 n + \left(\frac{1}{\overline{\eta}_0}\right)^3\right]e^{-n\overline{\eta}}\right\}
\end{aligned}
$$

5.4.4 Case 4: $v_{c2} < v < v_{c3}$

$$
\begin{aligned}
\overline{w}_b^I &= \Lambda_1^s + \left(\Lambda_\infty^s - \Lambda_1^s\right)\left\{1 + \frac{1}{2}\left[\frac{1}{n_1^2 - n_2^2}\right]\left[n_2^2 e^{n_1\overline{\eta}} - n_1^2 e^{n_2\overline{\eta}}\right]\right\} \\
&+ \left(\Lambda_2^d - \Lambda_\infty^d\right)e^{\frac{\overline{\eta}}{\overline{\eta}_0}} \qquad (5.33) \\
&+ \left(\Lambda_2^d - \Lambda_\infty^d\right)\left[\frac{1}{n_1 n_2\left(n_1^2 - n_2^2\right)}\right]\left\{\frac{1}{2}n_2\left[n_1 n_2^2 + \left(\frac{1}{\overline{\eta}_0}\right)n_2^2 - \left(\frac{1}{\overline{\eta}_0}\right)^2 n_1 - \left(\frac{1}{\overline{\eta}_0}\right)^3\right]e^{n_1\overline{\eta}}\right. \\
&- \left.\frac{1}{2}n_1\left[n_1^2 n_2 + \left(\frac{1}{\overline{\eta}_0}\right)n_1^2 - \left(\frac{1}{\overline{\eta}_0}\right)^2 n_2 - \left(\frac{1}{\overline{\eta}_0}\right)^3\right]e^{n_2\overline{\eta}}\right\}
\end{aligned}
$$

$$
\begin{aligned}
\overline{w}_b^{II} &= \Lambda_1^s + \left(\Lambda_2^\infty - \Lambda_1^s\right)\left\{-\frac{1}{2}\left[\frac{1}{n_1^2 - n_2^2}\right]\left[n_2^2 e^{-n_1\overline{\eta}} - n_1^2 e^{-n_2\overline{\eta}}\right]\right\} \qquad (5.34) \\
&+ \left(\Lambda_2^d - \Lambda_\infty^d\right)\left[\frac{1}{n_1 n_2\left(n_1^2 - n_2^2\right)}\right]\left\{-\frac{1}{2}n_2\left[n_1 n_2^2 - \left(\frac{1}{\overline{\eta}_0}\right)n_2^2 - \left(\frac{1}{\overline{\eta}_0}\right)^2 n_1 + \left(\frac{1}{\overline{\eta}_0}\right)^3\right]e^{-n_1\overline{\eta}}\right. \\
&- \left.\frac{1}{2}n_1\left[n_1^2 n_2 - \left(\frac{1}{\overline{\eta}_0}\right)n_1^2 - \left(\frac{1}{\overline{\eta}_0}\right)^2 n_2 + \left(\frac{1}{\overline{\eta}_0}\right)^3\right]e^{-n_2\overline{\eta}}\right\}
\end{aligned}
$$

5.4.5 Case 5: $v_{c3} < v$

$$\begin{aligned}
\overline{w}_b^I &= \Lambda_1^s + (\Lambda_\infty^s - \Lambda_1^s)\left\{1 + \left[\frac{1}{m_1^2 - m_2^2}\right]\left[m_2^2\cos(m_1\overline{\eta}) - m_1^2\cos(m_2\overline{\eta})\right]\right\} \\
&+ \left(\Lambda_2^d - \Lambda_\infty^d\right)e^{\frac{\overline{\eta}}{\overline{\eta}_0}} \qquad (5.35) \\
&+ \left(\Lambda_2^d - \Lambda_\infty^d\right)\left[\frac{1}{m_1 m_2\left(m_1^2 - m_2^2\right)}\right]\left\{m_1 m_2\left[m_2^2 + \left(\frac{1}{\overline{\eta}_0}\right)^2\right]\cos(m_1\overline{\eta})\right. \\
&+ m_2\left(\frac{1}{\overline{\eta}_0}\right)\left[m_2^2 + \left(\frac{1}{\overline{\eta}_0}\right)^2\right]\sin(m_1\overline{\eta}) \\
&- m_1 m_2\left[m_2^2 + \left(\frac{1}{\overline{\eta}_0}\right)^2\right]\cos(m_2\overline{\eta}) \\
&+ \left. m_2\left(\frac{1}{\overline{\eta}_0}\right)\left[m_2^2 + \left(\frac{1}{\overline{\eta}_0}\right)^2\right]\sin(m_2\overline{\eta})\right\} \\
&\overline{w}_b^{II} = 0 \qquad (5.36)
\end{aligned}$$

5.5 Response to arbitrary loading

In the two previous sections the response of the shell to shock and detonation loading was described analytically. For the model including rotatory inertia and shear deformation, it is also possible to develop a model for the description of the response to arbitrary loading profiles. The procedure is similar to the procedure for the thin shell model. For the model including rotatory inertia and shear deformation only another dispersion equation has to be used. The other formulas are the same as for the thin shell model. For the sake of brevity, the derivation is not repeated here.

5.6 Damping

As in the simple thin shell model, a damping term can be added to the differential equation. For a further description of damping, the reader is referred to section 4.6 and appendix D.

Chapter 6

Flexural model: thick infinite shell

6.1 Basic equations

This model was described by Mirsky and Hermann [21] and Simkins [13]. The basic equations for this model are listed in appendix E. Dimensionless quantities are introduced according to:

$$\begin{aligned} &\overline{u} = \frac{u}{h} \quad ; \qquad \overline{w} = \frac{w}{h} \quad ; \quad \overline{\eta} = \frac{\sqrt{12}}{h}\,[x - vt] \\ &\overline{\psi}_x = \frac{\psi_x}{\sqrt{12}} \quad ; \quad \overline{\psi}_z = \frac{\psi_z}{\sqrt{12}} \end{aligned} \tag{6.1}$$

The basic equations finally result in a matrix-vector equation:

$$[A]\,\{\boldsymbol{x}\} = \{b\} \tag{6.2}$$

where:

$$[A] = \begin{bmatrix} C_1\dfrac{\partial^2}{\partial\overline{\eta}^2} - C_2 & -C_3\dfrac{\partial}{\partial\overline{\eta}} & C_4\dfrac{\partial}{\partial\overline{\eta}} \\ C_5\dfrac{\partial}{\partial\overline{\eta}} & C_6\dfrac{\partial^2}{\partial\overline{\eta}^2} + C_7 & C_8\dfrac{\partial^2}{\partial\overline{\eta}^2} + C_9 \\ C_{10}\dfrac{\partial}{\partial\overline{\eta}} & C_{11}\dfrac{\partial^2}{\partial\overline{\eta}^2} + C_{12} & C_{13}\dfrac{\partial^2}{\partial\overline{\eta}^2} + C_{14} \end{bmatrix} \tag{6.3}$$

$$\{\boldsymbol{x}\} = \begin{Bmatrix} \overline{\psi}_x \\ \overline{w} \\ \overline{\psi}_z \end{Bmatrix} \tag{6.4}$$

$$\{b\} = \left\{ \begin{array}{c} 0 \\ \dfrac{\left[1-\sqrt{3}\beta\right] p_0}{12\rho v_d^2} \\ -\dfrac{\left[1-\sqrt{3}\beta\right] p_0}{4\sqrt{3}\rho v_d^2} \end{array} \right\} \tag{6.5}$$

where the elements depend on the following parameters:

$$\begin{aligned} v_d &= \sqrt{\frac{E}{\rho\left(1-\nu^2\right)}} \\ v_s &= \sqrt{\frac{\kappa G}{\rho}} \\ \beta &= \frac{h}{\sqrt{12}R} \\ \overline{\sigma} &= \frac{1}{\sqrt{12}} \log\left[\frac{1+\sqrt{3}\beta}{1-\sqrt{3}\beta}\right] \\ S_{xx} &= \left[\sigma_{xx}\left(1+\frac{z}{R}\right)\right]_{-\frac{h}{2}}^{\frac{h}{2}} \\ m_{xx} &= \left[\sigma_{xx} z\left(1+\frac{z}{R}\right)\right]_{-\frac{h}{2}}^{\frac{h}{2}} \\ q &= \left[p\left(1+\frac{z}{R}\right)\right]_{-\frac{h}{2}}^{\frac{h}{2}} \\ m_{zz} &= \left[pz\left(1+\frac{z}{R}\right)\right]_{-\frac{h}{2}}^{\frac{h}{2}} \end{aligned} \tag{6.6}$$

6.2 Dispersion equation

The dispersion equation can be obtained from the homogeneous equation, assuming exponential behaviour of the quantities. The determinant should be zero, resulting in a quite lengthy sixth order dispersion equation (see appendix E). For each value of the velocity v, the characteristic roots can be determined from this equation. The roots appear in pairs of complex conjugates. The corresponding eigenvectors are used to obtain the solution of the problem.

6.3 Solution of the problem

The response of the system is written as the sum of a homogeneous solution and a particular solution. The homogeneous part is a linear combination of eigenvectors. The particular solution is a constant solution. The participation factors for each eigenvector are determined from the continuity conditions and the fact that the solution has to remain bounded. A complete derivation of the solution is given in appendix E.

Chapter 7

Transient analytical model: thin shell

7.1 Basic equations

Consider a thin shell with length L (see figure 7.1): As a starting point for the

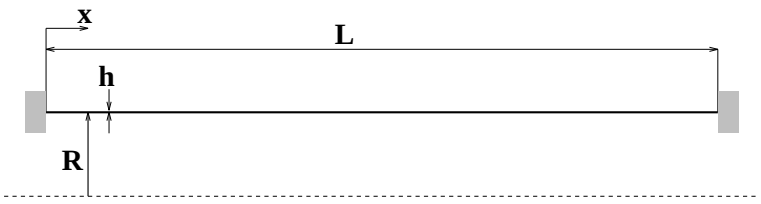

Figure 7.1: Thin shell of finite length

analytical transient model, the following equation is used (see section 4):

$$\frac{\partial^4 w}{\partial x^4} + \left(\frac{12}{v_d^2 h^2}\right)\frac{\partial^2 w}{\partial t^2} + \frac{12^2\beta^2\left(1-\nu^2\right)}{h^4}w = \frac{12^2}{h^3}F(x,t) \tag{7.1}$$

where $F(x,t)$ is the excitation function, see section 4.1. The analytical solution assumes that for each time t, the radial displacement is written as the sum of eigenmodes $\phi_k(x)$. The participation factors now have to be calculated. The total solution is obtained by superimposing two parts:

- static solution corresponding to the initial load
- dynamic solution for an advancing load

7.1.1 Static solution

The static equation is obtained by setting the time derivative zero:

$$\frac{\partial^4 w}{\partial x^4} + \frac{12^2\beta^2\left(1-\nu^2\right)}{h^4}w = \frac{12^2}{h^3}F_s(x) \tag{7.2}$$

where $F_s(x)$ is the static loading. The radial displacement is written as the sum of eigenmodes $\phi_q(x)$:

$$w(x,t) = \sum_{q=1,2..}^{\infty} a_q\phi_q(x) \tag{7.3}$$

Inserting this expression into the differential equation gives, dropping the (x) notation:

$$\sum_{q=1,2..}^{\infty}\left[\frac{\partial^4\phi_q}{\partial x^4} + \frac{12^2\beta^2\left(1-\nu^2\right)}{h^4}\phi_q\right]a_q = \frac{12^2}{h^3}F_s(x) \tag{7.4}$$

Since the functions ϕ_q are eigenmodes, one can write:

$$\sum_{q=1,2..}^{\infty}\omega_q^2 a_q\phi_q = \frac{12^2}{h^3}F_s(x,t) \tag{7.5}$$

where ω_q is the eigenfrequency for mode q. The eigenmodes are orthonormal:

$$\int_0^L \phi_q\phi_r dx = \begin{cases} 0 & \text{for } q \neq r \\ 1 & \text{for } q = r \end{cases} \tag{7.6}$$

Multiplying equation (7.4) by eigenmode r, integrating with respect to x and using the orthonormality finally gives:

$$a_q = \frac{12v_d^2}{\omega_q^2 h}\int_0^L \phi_q F_s(x)dx \tag{7.7}$$

For instance for a constant load, the participation factors can easily be calculated.

7.1.2 Dynamic solution

As a starting point for the analytical transient model, the following equation is used (see section 4):

$$\frac{\partial^4 w}{\partial x^4} + \left(\frac{12}{v_d^2 h^2}\right)\frac{\partial^2 w}{\partial t^2} + \frac{12^2\beta^2\left(1-\nu^2\right)}{h^4}w = \frac{12^2}{h^3}F_d(x,t) \tag{7.8}$$

where $F_d(x,t)$ is the dynamic loading of the shell. The radial displacement for each time t is written as the sum of eigenmodes $\phi_k(x)$:

$$w(x,t) = \sum_{q=1,2..}^{\infty} b_q(t)\phi_q(x) \tag{7.9}$$

Note that the participation factors are now a function of time. Using this expression, multiplying the equation (7.8) by eigenmode r, integrating with respect to x and using the orthonormality properties finally gives:

$$\frac{\partial^2 b_q}{\partial t^2} + \omega_q^2 b_q = \frac{12 v_d^2}{h} \int_0^L \phi_q F_d(x,t) dx \tag{7.10}$$

This is a simple second order differential equation in terms of the participation factor b_q. In the next sections solutions will be presented for simply supported shells and clamped shell subjected to shock or detonation loading.

7.1.3 Total solution

The total solution is obtained by superimposing the static and the dynamic solutions:

$$w(x,t) = \sum_{q=1,2..}^{\infty} \left[a_q + b_q(t)\right] \phi_q(x) \tag{7.11}$$

7.2 Simply supported shell

The modes of a simply supported shell are:

$$\phi_q = \sqrt{\frac{2}{L}} \sin\left(\frac{q\pi x}{L}\right) \qquad q = 1, 2..\infty \tag{7.12}$$

The corresponding eigenfrequencies are:

$$\omega_q^2 = \left(\frac{v_d^2 h^2}{12}\right)\left[\left(\frac{q\pi}{L}\right)^4 + \frac{12^2\beta^2\left(1-\nu^2\right)}{h^4}\right] \tag{7.13}$$

7.2.1 Response to shock loading

Static solution

The static loading is constant:

$$F_s(x) = \beta^2\left(1-\nu^2\right)\Lambda_1 \tag{7.14}$$

The static participation factors are simply:

$$a_q = \sqrt{\frac{2}{L}}\frac{12 v_d^2}{h}\beta^2\left(1-\nu^2\right)\left(\frac{L}{q\pi}\right)\left(\frac{\Lambda_1}{\omega_q^2}\right)\left[1-\cos\left(q\pi\right)\right] \tag{7.15}$$

Dynamic solution

The dynamic loading function is:

$$F_d(x,t) = \beta^2\left(1-\nu^2\right)\left(\Lambda_2-\Lambda_1\right)\left[1-H(x-vt)\right] \tag{7.16}$$

Because of the step function the equation for b_q can be written as:

$$\frac{\partial^2 b_q}{\partial t^2} + \omega_q^2 b_k = \sqrt{\frac{2}{L}}\left(\Lambda_2-\Lambda_1\right)\frac{12\beta^2\left(1-\nu^2\right)v_d^2}{h}\int_0^{vt}\sin\left(\frac{q\pi x}{L}\right)dx \tag{7.17}$$

This finally gives the following differential equation for b_q:

$$\frac{\partial^2 b_q}{\partial t^2} + \omega_q^2 a_q = \sqrt{\frac{2}{L}}\left(\Lambda_2-\Lambda_1\right)\frac{12\beta^2\left(1-\nu^2\right)v_d^2}{h}\left(\frac{L}{q\pi}\right)\left[1-\cos(vt)\right] \tag{7.18}$$

The boundary conditions are:

$$a_q(0) = 0 \quad ; \quad \left.\frac{\partial a_q}{\partial t}\right|_0 = 0 \tag{7.19}$$

The final solution is:

$$\begin{aligned} b_q \quad = \quad & \sqrt{\frac{2}{L}}\frac{12 v_d^2}{h}\beta^2\left(1-\nu^2\right)\left(\frac{L}{q\pi}\right)\left\{\frac{\Lambda_2-\Lambda_1}{\omega_q^2}\left[1-\cos\left(\omega_q t\right)\right]\right. \\ & \left. + \frac{\Lambda_2-\Lambda_1}{\left(\frac{q\pi v}{L}\right)^4-\omega_q^2}\left[\cos\left(\frac{q\pi v t}{L}\right)-\cos\left(\omega_q t\right)\right]\right\} \end{aligned} \tag{7.20}$$

7.2.2 Response to detonation loading

Static solution

The static loading is constant:

$$F_s(x) = \beta^2 \left(1 - \nu^2\right) \Lambda_1 \tag{7.21}$$

The static participation factors are simply:

$$a_q = \sqrt{\frac{2}{L}} \frac{12 v_d^2}{h} \beta^2 \left(1 - \nu^2\right) \left(\frac{L}{q\pi}\right) \left(\frac{\Lambda_1}{\omega_q^2}\right) \left[1 - \cos\left(q\pi\right)\right] \tag{7.22}$$

Dynamic solution

The dynamic loading function is:

$$F_d(x,t) = \beta^2 \left(1 - \nu^2\right) \left[1 - H(x - vt)\right] \left\{ \left(\Lambda_\infty - \Lambda_1\right) + \left(\Lambda_2 - \Lambda_\infty\right) e^{\left[\frac{x - vt}{vT}\right]} \right\} \tag{7.23}$$

The final solution for the dynamic participation factors is:

$$\begin{aligned} b_q \quad = \quad & \sqrt{\frac{2}{L}} \frac{12 v_d^2}{h} \beta^2 \left(1 - \nu^2\right) \left(\frac{L}{q\pi}\right) \left\{ \frac{\Lambda_2 - \Lambda_1}{\omega_q^2} \left[1 - \cos\left(\omega_q t\right)\right] \right. \\ & + \frac{\Lambda_2 - \Lambda_1}{\left(\frac{q\pi v}{L}\right)^4 - \omega_q^2} \left[\cos\left(\frac{q\pi v t}{L}\right) - \cos\left(\omega_q t\right) \right] \\ & + \frac{\Lambda_2 - \Lambda_\infty}{1 + \left(\frac{L}{q\pi}\right)^2 \left(\frac{1}{vT}\right)^2} \left[\frac{\cos\left(\frac{q\pi v t}{L}\right) - \sin\left(\frac{q\pi v t}{L}\right) + \left(\frac{q\pi v}{L}\right) \frac{1}{\omega_q} \sin\left(\omega_q t\right)}{\left(\frac{q\pi v}{L}\right)^2 - \omega_q^2} \right] \\ & \left. + \frac{\Lambda_2 - \Lambda_\infty}{1 + \left(\frac{L}{q\pi}\right)^2 \left(\frac{1}{vT}\right)^2} \left[\frac{e^{-\frac{t}{T}} + \frac{1}{\omega_q} \frac{1}{T} \sin\left(\omega_q t\right) - \cos\left(\omega_q t\right)}{\left(\frac{1}{T}\right)^2 + 1} \right] \right\} \end{aligned} \tag{7.24}$$

Chapter 8

Transient finite element model

One of the basic assumptions in the simplest analytical models is that the tube is infinite in length. This greatly simplifies the analysis and enables straightforward analytical solutions for this *steady state* problem. However, in reality end effects will affect the behaviour of the system. In fact, due to the reflection of structural waves at the end of a tube very high strains and stresses might result. Therefore it is interesting to analyze the *transient* behaviour of the shell in more detail. In the previous chapter an analytical model was developed to describe the transient behaviour of finite length shells. An alternative is offered by the finite element method. The finite element method enables a realistic modelling of geometries and boundary conditions. However, the generality of the packages also usually implies a large amount of overhead.

8.1 Flexural models

8.1.1 Mesh

The finite element model can be constructed with different kinds of elements. For a thin shell, rotatory symmetric 2 noded Mindlin type shell elements can be used (see figure 8.1). This element accounts for transverse shear deformation. A thick shell can be modelled with rotatory symmetric solid elements (see figure 8.2).

8.1.2 Boundary conditions

The finite element model enables a realistic modelling of boundary conditions and end effects. In the simplest situation the ends of a tube are for instance fully clamped, simply supported or free. However, it is also possible to introduce for instance an elastic clamping condition.

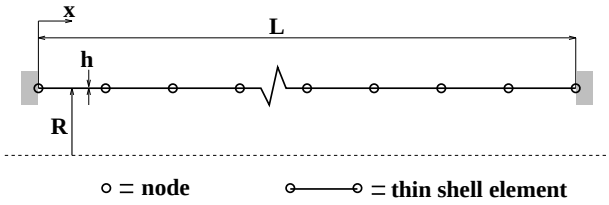

Figure 8.1: Mesh with rotatory symmetric 2 noded Mindlin elements

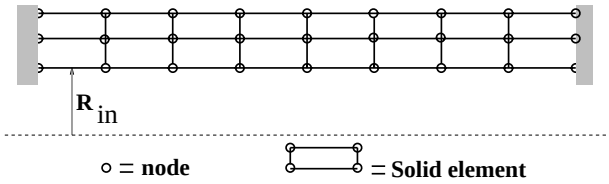

Figure 8.2: Mesh with rotatory symmetric solid elements

8.1.3 Structural response

In order to calculate the structural response, the problem can be split up into two parts: a static calculation and a dynamic calculation. The static deformation corresponding to the initial pressure difference across the shell is calculated with a linear elastic static model. The dynamical response to a shock or detonation travelling at speed v is then calculated with a transient linear elastic finite element model. Both results are superimposed to obtain the final solution. The load as a function of time is prescribed in each node. The response was calculated with a normal mode superposition technique. The modes of vibration of the shell were calculated first. These eigenmodes were then used to calculate the transient shell response.

Chapter 9

Practical considerations

When calculating the structural response of shells to moving loads, one has to be aware of the limitations and restrictions of interest. Some points of interest are:

- limits of predictability
  The critical velocity concept usually implies large speed for shells, of the order of magnitude of for instance 1000 m/s. The resulting structural vibrations are high frequency signals, with typical frequencies ranging from 5 kHz upto 50 kHz. The behaviour of structures at these high frequencies is sensitive to variation in the input data. As a consequence, a small variation in material or geometrical properties can lead to relatively large changes in the final result. For the designer this aspect should be of concern regarding design tolerances and variation in material properties.

- damping
  As already stated, the prediction of damping is difficult. Structural damping may be introduced by the material itself, but this amount of damping is usually relatively small. Other damping mechanisms are the damping in connections, seals and joints. Damping will be a restricting factor at resonance, thus providing an extra margin of safety.

- end effects
  The reflection and interference of structural waves can be important. Especially around the critical velocity there is a relatively strong precursor wave. Reflection of this precursor wave and interference with the bulk signal can lead to very high strains.

- non-linear effects
  The models presented so far are all based on linear theory. Any material or geometrical nonlinearity is therefore neglected. The linear models are only valid for small disturbances. When comparing calculations and experiments, it has to be ensured that the experimental results are in the

linear range. What tube design is concerned, the design will usually be based on the fact that the structure should be operated within the linear elastic regime.

- computational costs
  An issue that is strongly related to the limited predictability is the computational cost. Numerical models are able to describe the response in detail. When an increasing number of elements is used, finer scales can be resolved. However, due to the variation in input data and the increase in computational cost very large calculations do not add much practical value. Furthermore, more sophisticated material models should be used for detailed analysis.

Conclusions

Several models were developed to describe the response of shells to shock or detonation loading:

- analytical steady state models (infinite shells)
  - thin shell model
  - thin shell model including rotatory inertia and transverse shear
  - thick shell model

  The steady state models show the importance of the critical velocity concept. The radial deflection becomes unbounded when the velocity of the load is equal to the critical velocity. Damping and transient effects are not taken into account. For a finite length shell, the amplitude of the radial motion will increase with distance since the tube is initially at rest. This development of the profile and the reflection and interference of waves can not be desribed with the steady state models. For the designer however these are important issues.

- analytical transient models
  - thin shell model

  The transient models are able to describe the development, reflection and interference of waves. The analytical approaches however are limited to thin walled tubes with simple boundary conditions.

- transient finite element models
  - thin shell model
  - thick shell model

  The transient finite models are able to model arbitrary shells with more complicated boundary conditions. The calculation times however are significant.

Bibliography

[1] J. Mackerle. Structural response to impact, blast and shock loadings. a FE/BE bibliography (1993–1995). *Finite Elements in Analysis and Design*, 24:95–110, 1996.

[2] J.E. Rieker, Y.H. Lin, and M.W. Trethewey. Discretization considerations in moving load finite element beam models. *Finite elements in analysis and design*, 21:129–144, 1996.

[3] S.F. Felszeghy. The Timoshenko beam on an elastic foundation and subject to a moving step load, part I: steady-state response. *Journal of Vibration and Acoustics*, 118:277–284, 1996.

[4] S.F. Felszeghy. The Timoshenko beam on an elastic foundation and subject to a moving step load, part II: transient response. *Journal of Vibration and Acoustics*, 118:285–291, 1996.

[5] T.P. Chang and Y.N. Liu. Dynamic finite element analysis of a nonlinear beam subjected to a moving load. *International journal Solids and Structures*, 33(12):1673–1688, 1996.

[6] S. Ḿuller, T. Kryżyński, and H. Ilias. Comparison os semi-analytical methods of analyzing periodic structures under a moving load. *Vehicle system dynamics supplement*, 24:325–339, 1995.

[7] H.A. Dieterman and A.V. Metrikine. Steady-state displacements of a beam on an elastic half-space due to a uniformly moving constant load. *European Journal of Mechanics, A/solids*, 16(2):295–306, 1997.

[8] H.A. Dieterman and A. Metrikine. The equivalent stiffness of a half-space interacting with a beam. critical velocities of a moving load along the beam. *European Journal of Mechanics, A/Solids*, 15(1):67–90, 1996.

[9] G. Pan, H. Okada, and S.N. Atluri. Nonlinear transient dynamic analysis of soil-pavement interaction under moving load: a coupled BEM-FEM approach. *Engineering Analysis with Boundary Elements*, 14:99–112, 1994.

[10] H. Reismann. Response of a pre-stressed cylindrical shell to moving pressure load. In S. Ostrach and R.H. Scanlon, editors, *Eighth Midwest Mechanics Conference*, pages 349–363. Pergamon Press, 1965.

[11] M.C. de Malherbe, R.D. Wing, A.J. Laderman, and A.K. Oppenheim. Response of a cylindrical shell to internal blast loading. *Journal of Mechanical Engineering Science*, 8(1):91–98, 1966.

[12] S. Tang. Dynamic response of a tube under moving pressure. In *Proceedings of the American Society of Civil Engineers*, volume 5, pages 97–122. Engineering Mechanics Division, October 1965.

[13] T.E. Simkins. Resonance of flexural waves in gun tubes. Technical Report ARCCB–TR–87008, US Army Armament Research, Development and Engineering Center, Watervliet, N.Y. 12189–4050, July 1987.

[14] J.E. Shepherd. Pressure loads and structural response on the BNL high-temperature detonation tube. Technical Report A-3991, Brookhaven National Laboratory, Upton, New York 11973, September 1992.

[15] Q.M. Li and N. Jones. Blast loading of a "short" cylindrical shell with transverse shear effects. *International journal impact engineering*, 16(2):331–353, 1995.

[16] A.I. Bezverkhii and V.P. Mukoid. Reaction of a thick-walled cylindrical shell to a suddenly applied internal load. *International journal Applied Mechanics*, 30(6):441–445, 1994.

[17] N.S. Remez and I.A. Luchko. Deformation of a thick-walled cylindrical shell with a porous filler under an internal blast loading. *International journal Applied Mechanics*, 31(9):742–746, 1995.

[18] M.D. Olson. Efficient modelling of blast loaded stiffened plate and cylindrical shell structures. *Computers and structures*, 40(5):1139–1149, 1991.

[19] D.W. Tennant. Response and failure of internal structural subsystems under blast and shock loading. *Journal of pressure vessel technology*, 116:409–418, 1994.

[20] G. Mareska, P.P. Millela, and G. Pino. Structural response of a nuclear power plant steel containment under H2 detonation. *Nuclear engineering and design*, 40:119–126, 1993.

[21] I. Mirsky and G. Herrmann. Axially symmetric motions of thick cylindrical shells. *Journal of Applied Mechanics*, 1958.

[22] E. Burcsu and L. Zuhal. Effect of shock loading on circular tubes. Technical Report Ae 104 c, California Institute of Technology, Galcit, Pasadena 91125, 1997.

[23] M. El-Raheb and P. Wagner. Harmonic response of cylindrical and toroidal shells to an internal acoustic field. part i: Theory. *Journal of the Acoustical Society of America*, 78(2), 1985.

[24] M. El-Raheb and P. Wagner. Acoustic radiation from a shell with internal structures. *Journal of the Acoustical Society of America*, 85(6):2452–2464, 1989.

[25] E. Schultz. Strain measurements in detonation experiments. Technical report, California institute of technology, GALCIT, Pasadena 91125, 1997. Internal report.

[26] M.R. Eslami, M. Shakeri, and R. Sedaghatti. Coupled thermoelasticity of an axially symmetric cylindrical shell. *Journal of thermal stresses*, 17:115–135, 1994.

[27] A.V. Metrikin. Stationary waves in a nonlinear elastic system interacting with a moving load. *Acoustical physics*, 40(4):573–576, 1994.

[28] J. Pitk´aranta, Y. Leino, O. Ovaskainen, and J. Piila. Shell deformation states and the finite element method: a benchmark study of cylindrical shells. *Computational Methods in Applied Mechanical Engineering*, 128:81–121, 1995.

[29] K.R Sivadas and N. Ganesan. Axisymmetric vibration analysis of thick cylindrical shell with variable thickness. *Journal of sound and vibration*, 160(3):387–400, 1993.

[30] P.W. Smith, J.G. McDaniel, K.D. LePage, and R. Barile. Structural wave reflection coefficients of cylindrical shell terminations: numerical extraction and reciprocity constraints. *Journal of the acoustical society of America*, 101(2):900–908, 1997.

[31] J. Jiang and M.D. Olson. Nonlinear dynamic analysis of blast loaded cylindrical shell. *Computers and structures*, 41(1):41–52, 1991.

[32] T.J. Anderson and E.K. Dabora. Measurements of normal detonation wave structure using rayleigh imaging. *24th Symp. Int. Combust. Proc.*, pages 1853–1860, 1992.

[33] H.O. Barthel. Predicted spacings in hydrogen-oxygen-argon detonations. *Phys. Fluids*, 17(8):1547–1553, 1974.

[34] R.K. Kumar. Detonation cell widths in hydrogen-oxygen-diluent mixtures. *Combust. Flame*, 80(2):157–169, 1990.

[35] J.H Lee and H. Matsui. A comparison of the critical energies for direct initiation of spherical detonation in acetylene-oxygen mixtures. *Combust. Flame*, 28(1):61–66, 1977.

[36] R.A. Strehlow. Transverse waves in detonations: Ii. structure and spacing in h_2-o_2, c_2h_2-o_2, c_2h_4-o_2 and ch_4-o_2 systems. *AIAA Journal*, 7(3):492–496, 1969.

[37] R.A. Strehlow, R. Liangminas, R.H. Watson, and J.R. Eyman. Transverse wave structure in detonations. *11th Symp. Int. Combust. Proc.*, pages 683–692, 1967.

[38] R.A. Strehlow, R.E. Maurer, , and S. Rajan. Transverse waves in detonations: I. spacings in the hydrogen-oxygen system. *AIAA Journal*, 2(7):323–328, 1969.

Appendix A

Cross-sectional models

A.1 Basic equations

The basic equations, governing the response of the cross-sectional model are, see De Malherbe & Wing & Laderman & Oppenheim [11] and Shepherd [14]:

$$-\frac{N_{\theta\theta}}{R} + \left[1 - \frac{1}{2}\frac{h}{R}\right] p\,(t) = \rho h \frac{\partial^2 w}{\partial t^2} \tag{A.1}$$

where the stress resultant $N_{\theta\theta}$ is defined as:

$$N_{\theta\theta} = Eh\frac{w}{R} \tag{A.2}$$

The positive direction of the displacement is given in figure A.1. This gives

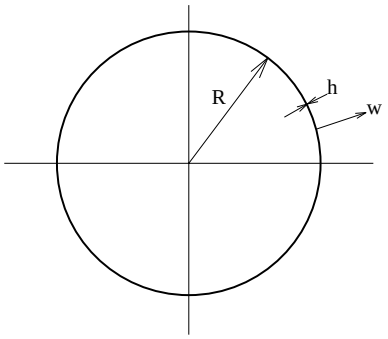

Figure A.1: Cross-sectional model

the following differential equation:

$$\frac{\partial^2 w}{\partial t^2} + \frac{E}{\rho R^2} w = \left[1 - \frac{1}{2}\frac{h}{R}\right] \frac{p\,(t)}{\rho h} \tag{A.3}$$

For a thin shell, $\frac{h}{R} \ll 1$:

$$\frac{\partial^2 w}{\partial t^2} + \Omega^2 w = \frac{p\,(t)}{\rho h} \tag{A.4}$$

where Ω is the frequency for radial (breathing) motion of the cross-section:

$$\Omega = \sqrt{\frac{E}{\rho R^2}} \tag{A.5}$$

The response of the tube to selected pressure histories can be obtained by Laplace transform. The Laplace transform $W = \mathcal{L}(w)$ of the displacement w is obtained from:

$$W = \mathcal{L}(w) = \int_0^\infty w e^{-st} dt \tag{A.6}$$

In a similar way for the pressure:

$$P = \mathcal{L}(p) = \int_0^\infty p e^{-st} dt \tag{A.7}$$

The differential equation now reduces to the following relation between the Laplace transforms:

$$W = \frac{1}{s^2 + \Omega^2} P \tag{A.8}$$

By taking the inverse Laplace transform of W, the structural response of the tube is obtained.

A.2 Response to detonation loading

Another example of the response to detonation loading:

$$p\,(t) = \begin{cases} p_1 & \text{for } t \leq 0 \\ p_2 & \text{for } 0 < t \leq \Delta t \\ (p_2 - p_\infty)\, e^{-\frac{t}{T}} + p_\infty & \text{for } t > \Delta t \end{cases} \tag{A.9}$$

$$w = \begin{cases} \Lambda_1 & \text{for } t \leq 0 \\ \Lambda_1 + (\Lambda_2 - \Lambda_1)\,[1 - \cos(\Omega t)] & \text{for } 0 < t \leq \Delta t \\ \Lambda_1 + (\Lambda_2 - \Lambda_1)\,[1 - \cos(\Omega t)] & \\ \quad + (\Lambda_\infty - \Lambda_2)\,[1 - \cos(\Omega\,(t - \Delta t))] & \\ \quad + (\Lambda_2 - \Lambda_\infty)\left[\dfrac{\Omega^2 T^2}{1 + \Omega^2 T^2}\right] & \\ \quad \left[\dfrac{1}{\Omega T}\sin(\Omega\,(t - \Delta t)) - \cos(\Omega\,(t - \Delta t)) + e^{-\frac{t - \Delta t}{T}}\right] & \text{for } t > \Delta t \end{cases} \tag{A.10}$$

Evidently, by taking $\Delta t \to 0$, the last expression degenerates to the solution of the first detonation problem (see chapter 3).

Appendix B

Thin shell equations

B.1 Basic equations

The basic equations for the thin shell model are [1], see *e.g* Simkins [13], Reismann [10], El-Raheb & Wagner [23, 24]:

$$\begin{gathered}\frac{\partial N_{xx}}{\partial x} = \rho h \frac{\partial^2 u}{\partial t^2} \\ \frac{\partial}{\partial x}\left[Q_x + N_{xx}\frac{\partial w}{\partial x}\right] - \frac{N_{\theta\theta}}{R} + \left[1 - \frac{1}{2}\frac{h}{R}\right] p_0 = \rho h \frac{\partial^2 w}{\partial t^2} \\ \frac{\partial M_{xx}}{\partial x} - Q_x = 0\end{gathered} \tag{B.1}$$

where the stress resultants N_{xx}, $N_{\theta\theta}$ and M_{xx} are defined as:

$$\begin{aligned}N_{xx} &= \frac{Eh}{1-\nu^2}\left[\frac{\partial u}{\partial x} + \nu\frac{w}{R}\right] \\ N_{\theta\theta} &= \frac{Eh}{1-\nu^2}\left[\nu\frac{\partial u}{\partial x} + \frac{w}{R}\right] \\ M_{xx} &= -\frac{Eh^3}{12\left(1-\nu^2\right)}\frac{\partial^2 w}{\partial x^2}\end{aligned} \tag{B.2}$$

The directions for the displacements and stress resultants are given in figure B.1.

Inserting the expression for N_{xx} into equation (B.1) gives:

$$\frac{Eh}{1-\nu^2}\left[\frac{\partial^2 u}{\partial x^2} + \nu\frac{1}{R}\frac{\partial w}{\partial x}\right] = \rho h \frac{\partial^2 u}{\partial t^2} \tag{B.3}$$

[1] The term $N_{xx}\frac{\partial w}{\partial x}$ is included to account for axial prestress effects

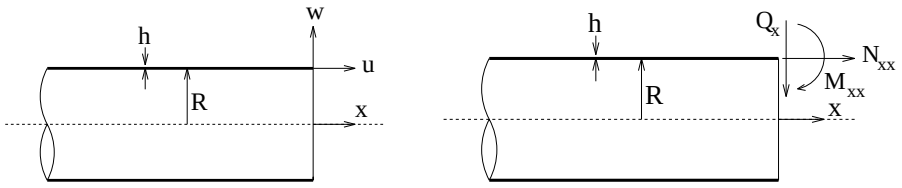

Figure B.1: Flexural model: displacements and stress resultants

Dimensionless quantities are introduced according to [2]:

$$\overline{u} = \frac{u}{h} \quad ; \quad \overline{w} = \frac{w}{h} \quad ; \quad \overline{\eta} = \frac{\sqrt{12}}{h}\left[x - vt\right] \tag{B.4}$$

The following parameters are used in the analysis:

$$\begin{aligned}
&\Lambda_i = \frac{\left(p_i - p_{atm}\right) R^2}{Eh^2} && \text{: excitation parameter} \\
&v_d = \sqrt{\frac{E}{\rho\left(1-\nu^2\right)}} && \text{: dilatational wave velocity in a shell} \\
&\beta = \frac{h}{\sqrt{12}R} && \text{: non dimensional shell thickness parameter} \\
&\delta = \frac{N_{xx}\left(1-\nu^2\right)}{Eh} && \text{: prestress parameter}
\end{aligned} \tag{B.5}$$

The equation for N_{xx} can now be written as:

$$\left[1 - \left(\frac{v}{v_d}\right)^2\right] \frac{\partial^2 \overline{u}}{\partial \overline{\eta}^2} + \nu\beta \frac{\partial \overline{w}}{\partial \overline{\eta}} = 0 \tag{B.6}$$

Integrating with respect to η and solving for $\dfrac{\partial \overline{u}}{\partial \overline{\eta}}$:

$$\frac{\partial \overline{u}}{\partial \overline{\eta}} = -\frac{\nu\beta}{\left[1 - \left(\frac{v}{v_d}\right)^2\right]} \overline{w} + \hat{C} \tag{B.7}$$

where C is an arbitrary constant. Inserting this into the expression for N_{xx} gives:

$$N_{xx} = \sqrt{12}\frac{Eh}{1-\nu^2}\left[-\frac{\nu\beta}{\left[1 - \left(\frac{v}{v_d}\right)^2\right]} \overline{w} + \nu\beta\overline{w} + \hat{C}\right] \tag{B.8}$$

[2] This choice is made is order to enable direct comparison with the other models

If one now assumes:

- $\dfrac{v}{v_d} \ll 1$: shock speed is low compared to dilatational wave speed

the following result for N_{xx} is obtained:

$$N_{xx} = C \tag{B.9}$$

The axial stress resultant is a constant, resulting from axial prestress. This result is not too surprizing, because the assumption implies that the velocity is small compared to the dilatational wave speed. For the dilatational waves, the motion is predominantly axial. Now using the fact that the axial stress resultant is a constant, the second equation in (B.1) can be written as (neglecting higher order terms in β):

$$A_4 \frac{\partial^4 \overline{w}}{\partial \overline{\eta}^4} + A_2 \frac{\partial^2 \overline{w}}{\partial \overline{\eta}^2} + A_0 \overline{w} = F\left(\overline{\eta}\right) \tag{B.10}$$

where:

$$A_4 = 1 \quad ; \quad A_2 = \left[\left(\frac{v}{v_d} \right)^2 - \delta \right] \quad ; \quad A_0 = \beta^2 \left(1 - \nu^2\right) \tag{B.11}$$

When dynamic terms, prestress and flexural terms are neglected, the model evidently degenerates to the static cross-sectional model.

B.2 Continuity conditions

The following quantities have to be continuous at $\overline{\eta} = 0$:

- displacement: $\overline{w}^I(0) = \overline{w}^{II}(0)$
- rotation: $\left.\dfrac{\partial \overline{w}^I}{\partial \overline{\eta}}\right|_0 = \left.\dfrac{\partial \overline{w}^{II}}{\partial \overline{\eta}}\right|_0$
- moment: $\left.\dfrac{\partial^2 \overline{w}^I}{\partial \overline{\eta}^2}\right|_0 = \left.\dfrac{\partial^2 \overline{w}^{II}}{\partial \overline{\eta}^2}\right|_0$
- shear: $\left.\dfrac{\partial^3 \overline{w}^I}{\partial \overline{\eta}^3}\right|_0 = \left.\dfrac{\partial^3 \overline{w}^{II}}{\partial \overline{\eta}^3}\right|_0$

B.3 Dispersion equation

The dispersion equation for the problem is:

$$A_4 \alpha^4 + A_2 \alpha^2 + A_0 = 0 \tag{B.12}$$

where α is related to the wave number k through:

$$k = \frac{\sqrt{12}\alpha}{ih} \tag{B.13}$$

B.4 Group velocity

An important quantity that will be used in futher analysis is the group velocity. The group velocity v_g is the speed at which energy is transported. It is related to the phase speed v of the wave as:

$$v_g = k\frac{\partial v}{\partial k} + k \tag{B.14}$$

The partial derivative of v with respect to k can be determined by for instance differentiating the dispersion equation with respect to k. The final result is expressed in terms of α:

$$v_g = v_d \frac{2\left(\frac{\alpha}{i}\right)}{\sqrt{1+\left(\frac{i}{\alpha}\right)^2 \beta\left(1-\nu^2\right)}} \tag{B.15}$$

B.5 Response to shock loading

The solution for shock loading is obtained from [3] the differential equation (B.10) with right hand side function:

$$\begin{aligned} F\left(\overline{\eta}\right) &= \beta^2\left(1-\nu^2\right)\left\{\Lambda_1 + \left(\Lambda_2 - \Lambda_1\right)\left[1 - H\left(\overline{\eta}\right)\right]\right\} \\ &- \frac{\nu\beta\delta}{\sqrt{12}} \end{aligned} \tag{B.16}$$

The general solution for the two regions can be written as:

$$\begin{aligned} \overline{w}^I &= C_1^I e^{\alpha_1\overline{\eta}} + C_2^I e^{\alpha_2\overline{\eta}} + C_3^I e^{\alpha_3\overline{\eta}} + C_4^I e^{\alpha_4\overline{\eta}} + \Lambda_1^s - \frac{\nu\beta\delta}{\sqrt{12}A_0} \\ \overline{w}^{II} &= C_1^{II} e^{\alpha_1\overline{\eta}} + C_2^{II} e^{\alpha_2\overline{\eta}} + C_3^{II} e^{\alpha_3\overline{\eta}} + C_4^{II} e^{\alpha_4\overline{\eta}} + \Lambda_\infty^s - \frac{\nu\beta\delta}{\sqrt{12}A_0} \end{aligned} \tag{B.17}$$

where:

$$\Lambda_i^s = \frac{\beta^2\left(1-\nu^2\right)}{A_0}\Lambda_i \tag{B.18}$$

B.5.1 Subcritical velocities

The characteristic roots for the subcritical case are:

$$\alpha_1 = n - im \quad ; \quad \alpha_2 = n + im \quad ; \quad \alpha_3 = -n + im \quad ; \quad \alpha_4 = -n - im \tag{B.19}$$

$$n = \frac{1}{2}\sqrt{\left(\frac{v_{c0}}{v_d}\right)^2 - \left(\frac{v}{v_d}\right)^2} \quad ; \quad m = \frac{1}{2}\sqrt{\left(\frac{v_{c0}}{v_d}\right)^2 + \left(\frac{v}{v_d}\right)^2} \tag{B.20}$$

[3] The solution for the static problem is simply obtained by taking $v = 0$ in the solution for the subcritical case

The solution has to remain bounded for $\overline{\eta} \to \pm\infty$: $C_3^I = C_4^I = C_1^{II} = C_2^{II} = 0$. Furthermore the displacement, rotation, moment and shear have to be continuous for $\overline{\eta} = 0$. The constants can be solved with these conditions. The final result is given in the main text.

B.5.2 Critical velocity

When the velocity v is equal to the critical velocity, there are double roots. In this case one has:

$$\alpha_1 = -im \quad ; \quad \alpha_2 = im \quad ; \quad \alpha_3 = im \quad ; \quad \alpha_4 = -im \tag{B.21}$$

where:

$$m = \frac{1}{2}\sqrt{2}\left(\frac{v_{c0}}{v_d}\right) \tag{B.22}$$

However, the solution for this case can not be determined. In fact, as v approaches v_{c0}, the values for the displacement become unbounded for the sub and supercritical case: $n \to 0$ or $m_1 \to m_2$.

B.5.3 Supercritical velocities

In the supercritical case, there are four purely imaginary roots:

$$\alpha_1 = -im_1 \quad ; \quad \alpha_2 = im_1 \quad ; \quad \alpha_3 = -im_2 \quad ; \quad \alpha_4 = im_2 \tag{B.23}$$

where m_1 and m_2 are real valued quantities according to::

$$m_1 = \frac{1}{2}\left[\sqrt{\left(\frac{v}{v_d}\right)^2 + \left(\frac{v_{c0}}{v_d}\right)^2} - \sqrt{\left(\frac{v}{v_d}\right)^2 - \left(\frac{v_{c0}}{v_d}\right)^2}\right]$$

$$m_2 = \frac{1}{2}\left[\sqrt{\left(\frac{v}{v_d}\right)^2 + \left(\frac{v_{c0}}{v_d}\right)^2} + \sqrt{\left(\frac{v}{v_d}\right)^2 - \left(\frac{v_{c0}}{v_d}\right)^2}\right] \tag{B.24}$$

Due to the fact that the characteristic roots are purely imaginary, the solution is bounded for $\overline{\eta} \to \pm\infty$. However, in this case another condition can be used to determine the solution. Energy has to flow away from the pressure step. The energy is transported at the group speed, v_g. In region 2, ahead of the pressure step, the group speed therefore has to exceed the phase speed. In region 1, the phase speed of the waves should exceed the group speed. This gives: $C_3^I = C_4^I = C_1^{II} = C_2^{II} = 0$. Furthermore, continuity conditions have to be satisfied at $\overline{\eta} = 0$ for displacement, rotation, moment and shear. The final result is given in the main text.

B.6 Response to detonation loading

The solution of the detonation problem is obtained from the same differential equation (B.10), with a different forcing function:

$$\begin{aligned} \text{detonation} : \mathrm{F}(\overline{\eta}) &= \beta^2\left(1-\nu^2\right)\left\{\Lambda_1 + \left(\Lambda_\infty - \Lambda_1\right)\left[1 - H\left(\overline{\eta}\right)\right]\right\} \\ &+ \beta^2\left(1-\nu^2\right)\left\{\left(\Lambda_2 - \Lambda_\infty\right)\left[1 - H\left(\overline{\eta}\right)\right] e^{\frac{\overline{\eta}}{\overline{\eta}_0}}\right\} \\ &- \frac{\nu\beta\delta}{\sqrt{12}} \end{aligned} \tag{B.25}$$

The general solution for the two regions can be written as:

$$\begin{aligned} \overline{w}^I &= C_1^I e^{\alpha_1\overline{\eta}} + C_2^I e^{\alpha_2\overline{\eta}} + C_3^I e^{\alpha_3\overline{\eta}} + C_4^I e^{\alpha_4\overline{\eta}} \\ &+ \left(\Lambda_2^d - \Lambda_\infty^d\right) e^{\frac{\overline{\eta}}{\overline{\eta}_0}} + \Lambda_\infty^s - \frac{\nu\beta\delta}{\sqrt{12}A_0} \end{aligned} \tag{B.26}$$

$$\begin{aligned} \overline{w}^{II} &= C_1^{II} e^{\alpha_1\overline{\eta}} + C_2^{II} e^{\alpha_2\overline{\eta}} + C_3^{II} e^{\alpha_3\overline{\eta}} + C_4^{II} e^{\alpha_4\overline{\eta}} \\ &+ \Lambda_1^s - \frac{\nu\beta\delta}{\sqrt{12}A_0} \end{aligned} \tag{B.27}$$

where:

$$\Lambda_i^d = \frac{\beta^2\left(1-\nu^2\right)}{A_4\left(\frac{1}{\overline{\eta}_0}\right)^4 + A_2\left(\frac{1}{\overline{\eta}_0}\right)^2 + A_0}\Lambda_i \tag{B.28}$$

Due to the fact that the right hand side forcing function is now a function of the $\overline{\eta}$ co-ordinate, the continuity conditions are somewhat more complicated than for the shock tube problem. However, the solution procedure is exactly the same. Therefore the whole derivation will not be repeated in this section. The results are given in the main text.

Appendix C

Flexural model: thin infinite shell including damping

C.1 Basic equations

In order to investigate the influence of damping on the structural response of the tube, a damping term is added to the thin shell equation (4.4). The damping term is proportional to the radial velocity, corresponding to viscous damping. The damping constant c_d is introduced according to:

$$c_d = \frac{c}{\sqrt{12}\rho} \tag{C.1}$$

where c is the damping constant that remains to be determined. The thin shell equation including damping can be written as:

$$\frac{\partial^4 \overline{w}}{\partial \overline{\eta}^4} + \left[\left(\frac{v}{v_d} \right)^2 - \delta \right] \frac{\partial^2 \overline{w}}{\partial \overline{\eta}^2} - \left(\frac{c_d}{v_d} \right) \left(\frac{v}{v_d} \right) \frac{\partial \overline{w}}{\partial \overline{\eta}} + \beta^2 \left(1 - \nu^2 \right) w = F\left(\overline{\eta} \right) \tag{C.2}$$

C.2 Dispersion equation

The dispersion equation for this problem is:

$$\alpha^4 + \left[\left(\frac{v}{v_d} \right)^2 - \delta \right] \alpha^2 - \left(\frac{c_d}{v_d} \right) \left(\frac{v}{v_d} \right) \alpha + \beta^2 \left(1 - \nu^2 \right) = 0 \tag{C.3}$$

In general, the damping term causes the roots to be complex for all velocities. This implies that there is no unbounded behaviour: the damping forces restrict the response to remain bounded. The characteristic roots can be determined with straightforward procedures for polynomials.

C.3 Determination of the damping constant

As in most structural dynamics problems, the estimation and prediction of damping is difficult. The question now remains how to determine the value of the damping constant c that is used in the model.

A theoretical prediction of the damping constant for detonation and shock tubes is very difficult. The damping depends heavily on for instance the clamping conditions and the use of rubber rings. The quantative predictability of the damping is therefore not very good. However, there is a way to determine the order of magnitude of the damping constant at least. By measuring the modal properties of the tube or a tube section, one can make an estimation of the amount of damping in the system. Note however that this method is inconstistent with the model assumptions. The damping will be determined for a tube of finite length, whereas the theory assumes a tube of infinite length.

Consider the differential equation for the tube motion, without damping and without loading. The eigenfrequencies of the tube can be determined by assuming harmonic motion and using the appropriate boundary conditions. For a tube with length l the eigenfrequencies ω can be calculated from [1]:

$$[\tan(\varepsilon) + \tanh(\varepsilon)][\tan(\varepsilon) - \tanh(\varepsilon)] = 0 \tag{C.4}$$

where:

$$\varepsilon = \frac{l}{2h}\left[\frac{12\omega^2 h^2}{v_d^2} - 12\beta^2\left(1-\nu^2\right)\right]^{\frac{1}{4}} \tag{C.5}$$

For a given tube geometry and material properties, the eigenfrequencies can be calculated from this equation. Because there is no damping in the system, the eigenfrequencies are *real* valued.

If there is damping in the system, the eigenfrequencies become complex:

$$\omega = \omega_0\left[\sqrt{1-\xi^2} + i\xi\right] \tag{C.6}$$

where ω_0 is the eigenfrequency of the undamped system and ξ is the dimensionless viscous damping coefficient. The quantities ω_0 and ξ can be measured or estimated. For lightly damped structures, ξ is of the order of magnitude of 0.005. For more heavily damped systems a typical value for ξ is 0.05.

For the damped system, the eigenfrequencies follow from:

$$[\tan(\hat{\varepsilon}) + \tanh(\hat{\varepsilon})][\tan(\hat{\varepsilon}) - \tanh(\hat{\varepsilon})] = 0 \tag{C.7}$$

where:

$$\hat{\varepsilon} = \frac{l}{2h}\left[\frac{12\omega^2 h^2}{v_d^2} + i\frac{12\omega c h}{\rho v_d^2} - 12\beta^2\left(1-\nu^2\right)\right]^{\frac{1}{4}} \tag{C.8}$$

Suppose the value of ω (complex) is known. With this equation the value of c can then be calculated.

[1] The two parts correspond to symmetric and asymmetric modes respectively

Appendix D

Thin shell equations including rotatory inertia and shear deformation

D.1 Basic equations

The basic equations for this model are (no prestress):

$$\begin{aligned} \frac{\partial N_{xx}}{\partial x} &= \rho h \frac{\partial^2 u}{\partial t^2} \\ \frac{\partial Q_x}{\partial x} - \frac{N_{\theta\theta}}{R} + \left[1 - \frac{1}{2}\frac{h}{R}\right] p_0 &= \rho h \frac{\partial^2 w}{\partial t^2} \\ \frac{\partial M_{xx}}{\partial x} - Q_x &= \rho h^3 \frac{\partial^2 \psi_x}{\partial t^2} \end{aligned} \tag{D.1}$$

where the stress resultants N_{xx}, $N_{\theta\theta}$ and M_{xx} are defined as:

$$\begin{aligned} N_{xx} &= \frac{Eh}{1-\nu^2}\left[\frac{\partial u}{\partial x} + \nu\frac{w}{R}\right] \\ N_{\theta\theta} &= \frac{Eh}{1-\nu^2}\left[\nu\frac{\partial u}{\partial x} + \frac{w}{R}\right] \\ M_{xx} &= \frac{Eh^3}{12\left(1-\nu^2\right)}\frac{\partial \psi_x}{\partial x} \\ Q_x &= \kappa G h\left[\psi_x + \frac{\partial w}{\partial x}\right] \end{aligned} \tag{D.2}$$

where κ is the shear correction factor and ψ_x is the rotation around the x-axis. The value of the shear correction factor is determined that waves with

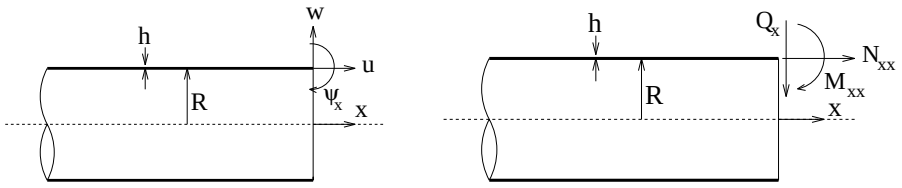

Figure D.1: Flexural model: displacements and stress resultants

small wavelengths travel at the speed of Rayleigh waves. The directions for the displacements and stress resultants are given in figure D.1.

Dimensionless quantitities are introduced according to:

$$\overline{u} = \frac{u}{h} \quad ; \quad \overline{w} = \frac{w}{h} \quad ; \quad \overline{\psi}_x = \frac{1}{\sqrt{12}}\psi_x \quad ; \quad \overline{\eta} = \frac{\sqrt{12}}{h}\left[x - vt\right] \tag{D.3}$$

The following parameters are used in the analysis:

$$\begin{aligned}
\Lambda &= \frac{p_0 R^2}{Eh^2} && \text{: excitation parameter} \\
v_d &= \sqrt{\frac{E}{\rho\left(1-\nu^2\right)}} && \text{: dilatational wave velocity in a shell} \\
v_s &= \sqrt{\frac{\kappa G}{\rho}} && \text{: shear wave velocity in a shell} \\
\beta &= \frac{h}{\sqrt{12}R} && \text{: non dimensional shell thickness parameter}
\end{aligned} \tag{D.4}$$

The basic equations can be written as:

$$\begin{gathered}
\left[1 - \left(\frac{v}{v_d}\right)^2\right] \frac{\partial^2 \overline{u}}{\partial \overline{\eta}^2} + \nu\beta \frac{\partial \overline{w}}{\partial \overline{\eta}} = 0 \\
-\nu\beta\left(\frac{v_d}{v_s}\right)\frac{\partial \overline{u}}{\partial \overline{\eta}} + \left[1 - \left(\frac{v}{v_s}\right)^2\right]\frac{\partial^2 \overline{w}}{\partial \overline{\eta}^2} - \beta^2\left(\frac{v_d}{v_s}\right)^2 \overline{w} + \frac{\partial \overline{\psi}_x}{\partial \overline{\eta}} = \left[\sqrt{3}\beta - 1\right]\left(\frac{p_0}{12\kappa G}\right) \\
-\left(\frac{v_s}{v_d}\right)^2 \frac{\partial \overline{w}}{\partial \overline{\eta}} + \left[1 - \left(\frac{v}{v_s}\right)^2\right]\frac{\partial^2 \overline{\psi}_x}{\partial \overline{\eta}^2} - \left(\frac{v_s}{v_d}\right)^2 \overline{\psi}_x = 0
\end{gathered} \tag{D.5}$$

The first equation is used to eliminate the axial displacement $\overline{u}$. The displacement is now split up into two parts:

$$\begin{aligned}
\overline{w} &= \overline{w}_b + \overline{w}_s \\
\overline{\psi}_x &= -\frac{\partial \overline{w}_b}{\partial \overline{\eta}}
\end{aligned} \tag{D.6}$$

Inserting these expressions into the equations, and integrating the last equation with respect to $\overline{\eta}$ finally gives [1]:

$$\overline{w}_s = -\left(\frac{v_d}{v_s}\right)^2 \left[1 - \left(\frac{v}{v_d}\right)^2\right] \frac{\partial^2 \overline{w}_b}{\partial \overline{\eta}^2} \tag{D.7}$$

The axial displacement follows from:

$$\frac{\partial \overline{u}}{\partial \overline{\eta}} = \frac{\nu\beta}{\left[\left(\frac{v}{v_d}\right)^2 - 1\right]} \left[\overline{w}_b + \overline{w}_s\right] \tag{D.8}$$

The final result for this model is the following differential equation:

$$A_4 \frac{\partial^4 \overline{w}_b}{\partial \overline{\eta}^4} + A_2 \frac{\partial^2 \overline{w}_b}{\partial \overline{\eta}^2} + A_0 \overline{w}_b = F\left(\overline{\eta}\right) \tag{D.9}$$

where $F\left(\overline{\eta}\right)$ is the right hand side function and:

$$\begin{aligned} A_4 &= \left[\left(\frac{v}{v_d}\right)^2 - 1\right]\left[\left(\frac{v}{v_s}\right)^2 - 1\right] \\ A_2 &= \left(\frac{v}{v_d}\right)^2 \left[1 + \beta^2 \left(\frac{v_d}{v_s}\right)^2\right] - \beta^2 \left(1 - \nu^2\right) \left(\frac{v_d}{v_s}\right)^2 \\ A_0 &= \beta^2 \left[1 + \frac{\nu^2}{\left[\left(\frac{v}{v_d}\right)^2 - 1\right]}\right] \end{aligned} \tag{D.10}$$

D.2 Continuity conditions

The following quantities have to be continuous at $\overline{\eta} = 0$:

- displacement: $\overline{w}_b^I(0) + \overline{w}_s^I(0) = \overline{w}_b^{II}(0) + \overline{w}_s^{II}(0)$
- rotation: $\overline{\psi}_x^I(0) = \overline{\psi}_x^{II}(0)$
- moment: $\left.\frac{\partial \overline{\psi}_x^I}{\partial \overline{\eta}}\right|_0 = \left.\frac{\partial \overline{\psi}_x^{II}}{\partial \overline{\eta}}\right|_0$
- shear: $\overline{\psi}_x^I(0) + \left.\frac{\partial \overline{w}_b^I}{\partial \overline{\eta}}\right|_0 + \left.\frac{\partial \overline{w}_s^I}{\partial \overline{\eta}}\right|_0 = \overline{\psi}_x^{II}(0) + \left.\frac{\partial \overline{w}_b^{II}}{\partial \overline{\eta}}\right|_0 + \left.\frac{\partial \overline{w}_s^{II}}{\partial \overline{\eta}}\right|_0$

[1] neglecting the $\sqrt{3}\beta$ term on the right hand side

However, since $\overline{w}_b$ and $\overline{w}_s$ are directly related, see (D.7). The quantity $\overline{\psi}_x$ can be expressed in terms of derivatives of $\overline{w}_b$. Finally, the continuity conditions can be expressed in terms of $\overline{w}_b$ only:

- displacement: $\overline{w}_b^I(0) = \overline{w}_b^{II}(0)$
- rotation: $\left.\frac{\partial \overline{w}_b^I}{\partial \overline{\eta}}\right|_0 = \left.\frac{\partial \overline{w}_b^{II}}{\partial \overline{\eta}}\right|_0$
- moment: $\left.\frac{\partial^2 \overline{w}_b^I}{\partial \overline{\eta}^2}\right|_0 = \left.\frac{\partial^2 \overline{w}_b^{II}}{\partial \overline{\eta}^2}\right|_0$
- shear: $\left.\frac{\partial^3 \overline{w}_b^I}{\partial \overline{\eta}^3}\right|_0 = \left.\frac{\partial^3 \overline{w}_b^{II}}{\partial \overline{\eta}^3}\right|_0$

D.3 Dispersion equation

The dispersion equation for this model is:

$$A_4\ \alpha^4 + A_2\ \alpha^2 + A_0 = 0 \tag{D.11}$$

where α is related to the wave number k through:

$$k = \frac{\sqrt{12}\alpha}{ih} \tag{D.12}$$

The values of the characteristic roots for each value of v can be determined with straightforward procedures for polynomials. No closed-form solution will be used in the present report.

D.4 Group velocity

An important quantity that will be used in futher analysis is the group velocity. The group velocity v_g is the speed at which energy is transported. It is related to the phase speed of the wave v as:

$$v_g = k\frac{\partial v}{\partial k} + k \tag{D.13}$$

The partial derivative of v with respect to k can be determined by for instance differentiating the dispersion equation with respect to k.

D.5 Response to shock loading

The solution for the shock problem is obtained from [2] the differential equation with forcing function:

$$F(\overline{\eta}) \quad = \quad \beta^2\left(1-\nu^2\right)\left\{\Lambda_1 + (\Lambda_2 - \Lambda_1)\left[1 - H(\overline{\eta})\right]\right\}$$

[2] The solution for the static problem is simply obtained by taking $v = 0$ in the solution for the subcritical case

The general solution for the two regions can be written as:

$$\overline{w}^I = C_1^I e^{\alpha_1 \overline{\eta}} + C_2^I e^{\alpha_2 \overline{\eta}} + C_3^I e^{\alpha_3 \overline{\eta}} + C_4^I e^{\alpha_4 \overline{\eta}} + \Lambda_1^s$$

$$\overline{w}^{II} = C_1^{II} e^{\alpha_1 \overline{\eta}} + C_2^{II} e^{\alpha_2 \overline{\eta}} + C_3^{II} e^{\alpha_3 \overline{\eta}} + C_4^{II} e^{\alpha_4 \overline{\eta}} + \Lambda_2^s \tag{D.14}$$

where:

$$\Lambda_i^s = \frac{\beta^2 \left(1 - \nu^2\right)}{A_0} \Lambda_i \tag{D.15}$$

D.5.1 Case 1: $0 < v < v_{c0}$

The characteristic roots for case 1 are all complex:

$$\alpha_1 = n - im \quad ; \quad \alpha_2 = n + im \quad ; \quad \alpha_3 = -n + im \quad ; \quad \alpha_4 = -n - im \tag{D.16}$$

The solution has to remain bounded for $\overline{\eta} \pm \infty$: $C_3^I = C_4^I = C_1^{II} = C_2^{II} = 0$. Furthermore the displacement, rotation, moment and shear have to be continuous for $\overline{\eta} = 0$. The final solution is given in the main text.

D.5.2 Case 2: $v_{c0} < v < v_{c1}$

In the second case, there are four purely imaginary roots:

$$\alpha_1 = -im_1 \quad ; \quad \alpha_2 = im_1 \quad ; \quad \alpha_3 = -im_2 \quad ; \quad \alpha_4 = im_2 \tag{D.17}$$

Due to the fact that the characteristic roots are purely imaginary, the solution is bounded for $\overline{\eta} \to \pm \infty$. Using the group speed concept gives: $C_3^I = C_4^I = C_1^{II} = C_2^{II} = 0$. Furthermore, continuity conditions have to be satisfied at $\overline{\eta} = 0$ for displacement, rotation, moment and shear. The final result is given in the main text.

D.5.3 Case 3: $v_{c1} < v < v_{c2}$

There are 4 characteristic roots, two real roots and two imaginary roots:

$$\alpha_1 = n \quad ; \quad \alpha_2 = -n \quad ; \quad \alpha_3 = im \quad ; \quad \alpha_4 = -im \tag{D.18}$$

The solution has to remain bounded: $C_2^I = C_1^{II} = 0$. The group velocity concept gives: $C_3^{II} = C_4^{II} = 0$. The final result can be found in the main text

D.5.4 Case 4: $v_{c2} < v < v_{c3}$

There are 4 characteristic roots, all real:

$$\alpha_1 = n_1 \quad ; \quad \alpha_2 = n_2 \quad ; \quad \alpha_3 = -n_1 \quad ; \quad \alpha_4 = -n_2 \tag{D.19}$$

The solution has to remain bounded: $C_3^I = C_4^I = C_1^{II} = C_2^{II} = 0$. The final result is given in the main text.

D.5.5 Case 5: $v_{c3} < v$

In the fifth case, there are four purely imaginary roots:

$$\alpha_1 = -im_1 \quad ; \quad \alpha_2 = im_1 \quad ; \quad \alpha_3 = -im_2 \quad ; \quad \alpha_4 = im_2 \tag{D.20}$$

The group velocity concept gives: $C_1^{II} = C_2^{II} = C_3^{II} = C_4^{II} = 0$. The result shows that there are no waves ahead of the pressure front when the shock speed exceeds the dilatational wave speed. The final expression for the displacement is given in the main text.

D.6 Response to detonation loading

The solution of the detonation problem is obtained from the same equation, with a different forcing function:

$$\begin{aligned} F(\overline{\eta}) &= \beta^2\left(1-\nu^2\right)\left\{\Lambda_1 + \left(\Lambda_\infty - \Lambda_1\right)\left[1 - H(\overline{\eta})\right]\right\} \\ &+ \beta^2\left(1-\nu^2\right)\left\{\left(\Lambda_2 - \Lambda_\infty\right)\left[1 - H(\overline{\eta})\right] e^{\frac{\overline{\eta}}{\overline{\eta}_0}}\right\} \end{aligned}$$

The general solution for the two regions can be written as:

$$\begin{aligned} \overline{w}_b^I &= C_1^I e^{\alpha_1\overline{\eta}} + C_2^I e^{\alpha_2\overline{\eta}} + C_3^I e^{\alpha_3\overline{\eta}} + C_4^I e^{\alpha_4\overline{\eta}} \\ &+ \left(\Lambda_2^d - \Lambda_\infty^d\right) e^{\frac{\overline{\eta}}{\overline{\eta}_0}} + \Lambda_\infty^s \end{aligned} \tag{D.21}$$

$$\overline{w}_b^{II} = C_1^{II} e^{\alpha_1\overline{\eta}} + C_2^{II} e^{\alpha_2\overline{\eta}} + C_3^{II} e^{\alpha_3\overline{\eta}} + C_4^{II} e^{\alpha_4\overline{\eta}} \tag{D.22}$$

$$+ \quad \Lambda_1^s \tag{D.23}$$

where:

$$\Lambda_i^d = \frac{\beta^2\left(1-\nu^2\right)}{A_4\left(\frac{1}{\overline{\eta}_0}\right)^4 + A_2\left(\frac{1}{\overline{\eta}_0}\right)^2 + A_0}\Lambda_i \tag{D.24}$$

Due to the fact that the right hand side forcing function is now a function of the $\overline{\eta}$ co-ordinate, the continuity conditions are somewhat more complicated than for the shock tube problem. However, the solution procedure is exactly the same. Therefore the whole derivation will not be repeated in this section. The results are given in the main text.

Appendix E

Thick shell equations

E.1 Basic equations

The basic equations for the thick shell model are:

$$\left[\frac{E\nu}{(1+\nu)(1-2\nu)}+\frac{E}{(1+\nu)}\right]\frac{\partial^2 u}{\partial x^2}-\rho\frac{\partial^2 u}{\partial t^2}+ \left\{\left[\frac{E\nu}{(1+\nu)(1-2\nu)}+\frac{E}{(1+\nu)}\right]\frac{\partial^2 \psi_x}{\partial x^2}-\rho\frac{\partial^2 \psi_x}{\partial t^2}\right\}\frac{h^2}{12R}+ \frac{1}{R}\left[\frac{E\nu}{(1+\nu)(1-2\nu)}\right]\frac{\partial w}{\partial x}+\left[\frac{E\nu}{(1+\nu)(1-2\nu)}\right]\frac{\partial \psi_z}{\partial x}=S_{xx} \tag{E.1}$$

$$\left\{\left[\frac{E\nu}{(1+\nu)(1-2\nu)}+\frac{E}{(1+\nu)}\right]\frac{\partial^2 u}{\partial x^2}-\rho\frac{\partial^2 u}{\partial t^2}\right\}\frac{h^2}{12R}+ \left[\frac{E\nu}{(1+\nu)(1-2\nu)}+\frac{E}{(1+\nu)}\right]\frac{h^2}{12}\frac{\partial^2 \psi_x}{\partial x^2}-\kappa\frac{E}{2(1+\nu)}\psi_x-\rho\frac{h^2}{12}\frac{\partial^2 \psi_x}{\partial t^2}- \kappa\frac{E}{2(1+\nu)}\frac{\partial w}{\partial x}+\left[\frac{2E\nu}{(1+\nu)(1-2\nu)}-\kappa\frac{E}{2(1+\nu)}\right]\frac{h^2}{12R}\frac{\partial \psi_z}{\partial x}=\frac{m_{xx}}{h} \tag{E.2}$$

$$-\frac{E\nu}{(1+\nu)(1-2\nu)}\frac{1}{R}\frac{\partial u}{\partial x}+\kappa G\frac{\partial \psi_x}{\partial x}+ \kappa G\frac{\partial^2 w}{\partial x^2}-\left[\frac{E\nu}{(1+\nu)(1-2\nu)}+\frac{E\nu}{(1+\nu)}\right]\frac{\sigma}{Rh}w-\rho\frac{\partial^2 w}{\partial t^2}+ \kappa G\frac{h^2}{12R}\frac{\partial^2 \psi_z}{\partial x^2}-\left[\frac{E\nu}{(1+\nu)(1-2\nu)}+\kappa\frac{E}{(1+\nu)}\right]\left[\frac{h-R\sigma}{Rh}\right]\psi_z- \frac{E\nu}{(1+\nu)(1-2\nu)}\frac{1}{R}\psi_z-\rho\frac{h^2}{12R}\frac{\partial^2 \psi_z}{\partial t^2}=\frac{q}{h} \tag{E.3}$$

$$
\begin{aligned}
&-\frac{E\nu}{(1+\nu)(1-2\nu)}\frac{\partial u}{\partial x}-\left[\frac{2E\nu}{(1+\nu)(1-2\nu)}-\kappa G\right]\frac{h^2}{12R}\frac{\partial \psi_x}{\partial x}+\\
&\kappa G\frac{h^2}{12R}\frac{\partial^2 w}{\partial x^2}-\left[\frac{E\nu}{(1+\nu)(1-2\nu)}+\frac{E\nu}{(1+\nu)}\right]\frac{h-R\sigma}{Rh}w-\\
&\frac{E\nu}{(1+\nu)(1-2\nu)}\frac{1}{R}w-\rho\frac{h^2}{12R}\frac{\partial^2 w}{\partial t^2}+\kappa G\frac{h^2}{12}\frac{\partial^2 \psi_z}{\partial x^2}-\\
&\left[\frac{E\nu}{(1+\nu)(1-2\nu)}+\kappa\frac{E}{(1+\nu)}\right]\left[1+\frac{\sigma R^2-Rh}{Rh}\right]\psi_z-\rho\frac{h^2}{12}\frac{\partial^2 \psi_z}{\partial t^2}=\frac{m_{zz}}{h}
\end{aligned}
\tag{E.4}
$$

Dimensionless quantities are introduced according to:

$$
\begin{aligned}
&\overline{u}=\frac{u}{h}\qquad \overline{w}=\frac{w}{h}\qquad \overline{\eta}=\frac{\sqrt{12}}{h}\left[x-vt\right]\\
&\overline{\psi}_x=\frac{\psi_x}{\sqrt{12}}\quad \overline{\psi}_z=\frac{\psi_z}{\sqrt{12}}
\end{aligned}
\tag{E.5}
$$

The following quantities are used in further analysis:

$$
\begin{aligned}
v_d &= \sqrt{\frac{E}{\rho\left(1-\nu^2\right)}}\\
v_s &= \sqrt{\frac{\kappa G}{\rho}}\\
\beta &= \frac{h}{\sqrt{12}R}\\
\overline{\sigma} &= \frac{1}{\sqrt{12}}\log\left[\frac{1+\sqrt{3}\beta}{1-\sqrt{3}\beta}\right]\\
S_{xx} &= \left[\sigma_{xx}\left(1+\frac{z}{R}\right)\right]_{-\frac{h}{2}}^{\frac{h}{2}}\\
m_{xx} &= \left[\sigma_{xx}z\left(1+\frac{z}{R}\right)\right]_{-\frac{h}{2}}^{\frac{h}{2}}\\
q &= \left[p\left(1+\frac{z}{R}\right)\right]_{-\frac{h}{2}}^{\frac{h}{2}}\\
m_{zz} &= \left[pz\left(1+\frac{z}{R}\right)\right]_{-\frac{h}{2}}^{\frac{h}{2}}
\end{aligned}
\tag{E.6}
$$

The equations are written in a dimensionless form and the axial displacement is eliminated. The following assumptions are introduced:

- no axial prestress: $S_{xx}=0$
- internal overpressure only: $q=p_0\left[1-\sqrt{3}\beta\right]$

The equations can be written in the following matrix form:

$$[A]\{\boldsymbol{x}\} = \{b\} \tag{E.7}$$

where:

$$[A] = \begin{bmatrix} C_1\dfrac{\partial^2}{\partial\overline{\eta}^2} - C_2 & -C_3\dfrac{\partial}{\partial\overline{\eta}} & C_4\dfrac{\partial}{\partial\overline{\eta}} \\ C_5\dfrac{\partial}{\partial\overline{\eta}} & C_6\dfrac{\partial^2}{\partial\overline{\eta}^2} + C_7 & C_8\dfrac{\partial^2}{\partial\overline{\eta}^2} + C_9 \\ C_{10}\dfrac{\partial}{\partial\overline{\eta}} & C_{11}\dfrac{\partial^2}{\partial\overline{\eta}^2} + C_{12} & C_{13}\dfrac{\partial^2}{\partial\overline{\eta}^2} + C_{14} \end{bmatrix} \tag{E.8}$$

$$\{\boldsymbol{x}\} = \begin{Bmatrix} \overline{\psi}_x \\ \overline{w} \\ \overline{\psi}_z \end{Bmatrix} \tag{E.9}$$

$$\{b\} = \begin{Bmatrix} 0 \\ \dfrac{\left[1-\sqrt{3}\beta\right]p_0}{12\rho v_d^2} \\ -\dfrac{\left[1-\sqrt{3}\beta\right]p_0}{4\sqrt{3}\rho v_d^2} \end{Bmatrix} \tag{E.10}$$

and:

$$
\begin{aligned}
C_1 &= \left[\frac{(1-\nu)^2}{1-2\nu}\right]\left[1-\beta^2\right] \\
C_2 &= \left(\frac{v_s}{v_d}\right)^2 \\
C_3 &= \left(\frac{v_s}{v_d}\right)^2 + \beta^2\frac{\nu\,(1-\nu)}{1-2\nu} \\
C_4 &= \beta\left[\frac{\nu\,(1-\nu)}{1-2\nu} - \left(\frac{v_s}{v_d}\right)^2\right] \\
C_5 &= \left(\frac{v_s}{v_d}\right)^2 + \beta^2\frac{\nu\,(1-\nu)}{1-2\nu} \\
C_6 &= \left(\frac{v_s}{v_d}\right)^2\left[1-\left(\frac{v}{v_s}\right)^2\right] \\
C_7 &= \beta^2\frac{\left[\frac{\nu(1-\nu)}{1-2\nu}\right]^2}{\frac{(1-\nu)^2}{1-2\nu}-\left(\frac{v}{v_d}\right)^2} - \beta\overline{\sigma}\frac{(1-\nu)^2}{1-2\nu} \\
C_8 &= \beta\left(\frac{v_s}{v_d}\right)^2\left[1-\left(\frac{v}{v_s}\right)^2\right] \\
C_9 &= \beta\frac{\left[\frac{\nu(1-\nu)}{1-2\nu}\right]^2}{\frac{(1-\nu)^2}{1-2\nu}-\left(\frac{v}{v_d}\right)^2} - \beta\left[\frac{(1-\nu)^2}{1-2\nu}\right]\left[1-\frac{\overline{\sigma}}{\beta}\right] - \beta\frac{\nu\,(1-\nu)}{1-2\nu} \\
C_{10} &= \beta\left[\left(\frac{v_s}{v_d}\right)^2 - \frac{\nu\,(1-\nu)}{1-2\nu}\right] \\
C_{11} &= \beta\left(\frac{v_s}{v_d}\right)^2\left[1-\left(\frac{v}{v_s}\right)^2\right] \\
C_{12} &= \beta\frac{\left[\frac{\nu(1-\nu)}{1-2\nu}\right]^2}{\frac{(1-\nu)^2}{1-2\nu}-\left(\frac{v}{v_d}\right)^2} - \beta\left[\frac{(1-\nu)^2}{1-2\nu}\right]\left[1-\frac{\overline{\sigma}}{\beta}\right] - \beta\frac{\nu\,(1-\nu)}{1-2\nu} \\
C_{13} &= \left(\frac{v_s}{v_d}\right)^2\left[1-\left(\frac{v}{v_s}\right)^2\right] \\
C_{14} &= \frac{\left[\frac{\nu(1-\nu)}{1-2\nu}\right]^2}{\frac{(1-\nu)^2}{1-2\nu}-\left(\frac{v}{v_d}\right)^2} - \left[\frac{(1-\nu)^2}{1-2\nu}\right]\frac{\overline{\sigma}}{\beta}
\end{aligned}
\tag{E.11}
$$

E.2 Dispersion equation

The dispersion equation is obtained from the homogeneous part of the equation by substituting:

$$\left\{ \begin{array}{c} \overline{\psi}_x \\ \\ \overline{w} \\ \\ \overline{\psi}_z \end{array} \right\} = \left\{ \begin{array}{c} X_1 \\ X_2 \\ X_3 \end{array} \right\} e^{\alpha \overline{\eta}} \tag{E.12}$$

The determinant of the matrix the should vanish, resulting in the following quite lengthy sixth order dispersion equation:

$$\begin{aligned} &[C_1C_6C_{13} - C_1C_9C_{11}]\,\alpha^6 + \\ &[C_1C_6C_{14} + C_1C_7C_{13} - C_1C_9C_{11} - C_1C_8C_{12} - C_2C_6C_{13} \\ &C_2C_8C_{11} + C_3C_5C_{13} - C_3C_8C_{10} + C_4C_5C_{11} - C_4C_6C_{10}]\,\alpha^4 \\ &[C_1C_7C_{14} - C_1C_9C_{12} - C_2C_6C_{14} - C_2C_7C_{13} + C_2C_9C_{11} \\ &C_2C_8C_{12} + C_3C_5C_{14} - C_3C_9C_{10} + C_4C_5C_{12} - C_4C_7C_{10}]\,\alpha^2 \\ &[-C_2C_7C_{14} + C_2C_9C_{12}] = 0 \end{aligned} \tag{E.13}$$

For every value of the velocity v, the six roots can be solved from this equation. The characteristic roots occur in pairs of complex conjugates. The eigenvector, corresponding to the characteristic root α_j is denoted as (third element is set to one for normalization):

$$\{\boldsymbol{e}_j\} = \left\{ \begin{array}{c} e_{j1} \\ e_{j2} \\ 1 \end{array} \right\} \tag{E.14}$$

E.3 Continuity conditions

The following continuity conditions have to be satisfied:

- $\overline{\psi}_x^I(0) = \overline{\psi}_x^{II}(0)$
- $\overline{w}^I(0) = \overline{w}^{II}(0)$
- $\overline{\psi}_z^I(0) = \overline{\psi}_z^{II}(0)$
- $\left.\dfrac{\partial \overline{\psi}_x^I}{\partial \overline{\eta}}\right|_0 = \left.\dfrac{\partial \overline{\psi}_x^{II}}{\partial \overline{\eta}}\right|_0$

- $\left.\dfrac{\partial \overline{w}^I}{\partial \overline{\eta}}\right|_0 = \left.\dfrac{\partial \overline{w}^{II}}{\partial \overline{\eta}}\right|_0$
- $\left.\dfrac{\partial \overline{\psi}_z^I}{\partial \overline{\eta}}\right|_0 = \left.\dfrac{\partial \overline{\psi}_z^{II}}{\partial \overline{\eta}}\right|_0$

E.4 Solution of the problem

The response is written as:

$$\left\{ \begin{array}{c} \overline{\psi}_x \\ \overline{w} \\ \overline{\psi}_z \end{array} \right\}^I = \sum_{j=1}^{6} C_j^I \left\{ \begin{array}{c} e_{j1} \\ e_{j2} \\ 1 \end{array} \right\} e^{\alpha_j \overline{\eta}} + \left\{ \begin{array}{c} \overline{\psi}_x \\ \overline{w} \\ \overline{\psi}_z \end{array} \right\}_p^I \tag{E.15}$$

$$\left\{ \begin{array}{c} \overline{\psi}_x \\ \overline{w} \\ \overline{\psi}_z \end{array} \right\}^{II} = \sum_{j=1}^{6} C_j^{II} \left\{ \begin{array}{c} e_{j1} \\ e_{j2} \\ 1 \end{array} \right\} e^{\alpha_j \overline{\eta}} + \left\{ \begin{array}{c} \overline{\psi}_x \\ \overline{w} \\ \overline{\psi}_z \end{array} \right\}_p^{II} \tag{E.16}$$

The first part in the solution is a linear combination of the eigenvectors, while the second part accounts for a particular solution. The particular solutions are:

$$\left\{ \begin{array}{c} \overline{\psi}_x \\ \overline{w} \\ \overline{\psi}_z \end{array} \right\}_p^I = \left\{ \begin{array}{c} 0 \\ 0 \\ 0 \end{array} \right\} \tag{E.17}$$

$$\left\{ \begin{array}{c} \overline{\psi}_x \\ \overline{w} \\ \overline{\psi}_z \end{array} \right\}_p^{II} = \left\{ \begin{array}{c} 0 \\ 0 \\ 0 \end{array} \right\} \tag{E.18}$$

The solution has to remain bounded and continuity conditions have to be satisfied at $\overline{\eta} = 0$. This gives:

$$C_4^I = C_5^I = C_6^I = C_1^{II} = C_2^{II} = C_3^{II} = 0 \tag{E.19}$$

and:

$$\left[\begin{array}{cccccc} e_{11} & e_{21} & e_{31} & -e_{41} & -e_{51} & -e_{61} \\ \alpha_1 e_{11} & \alpha_2 e_{21} & \alpha_3 e_{31} & -\alpha_4 e_{41} & -\alpha_5 e_{51} & -\alpha_6 e_{61} \\ e_{12} & e_{22} & e_{32} & -e_{42} & -e_{52} & -e_{62} \\ \alpha_1 e_{12} & \alpha_2 e_{22} & \alpha_3 e_{32} & -\alpha_4 e_{42} & -\alpha_5 e_{52} & -\alpha_6 e_{62} \\ 1 & 1 & 1 & -1 & -1 & -1 \\ \alpha_1 & \alpha_2 & \alpha_3 & -\alpha_4 & -\alpha_5 & -\alpha_6 \end{array} \right] \left\{ \begin{array}{c} C_1^I \\ C_2^I \\ C_3^I \\ C_4^{II} \\ C_5^{II} \\ C_6^{II} \end{array} \right\} = \left\{ \begin{array}{c} 0 \\ 0 \\ -\overline{w}_p^I \\ 0 \\ -\overline{\psi}_{zp}^I \\ 0 \end{array} \right\} \tag{E.20}$$

Once the constants are determined, the solution is known.

University of Twente
The Netherlands

Structural response of shells to detonation and shock loading, part II: shock loading of a thin aluminum tube

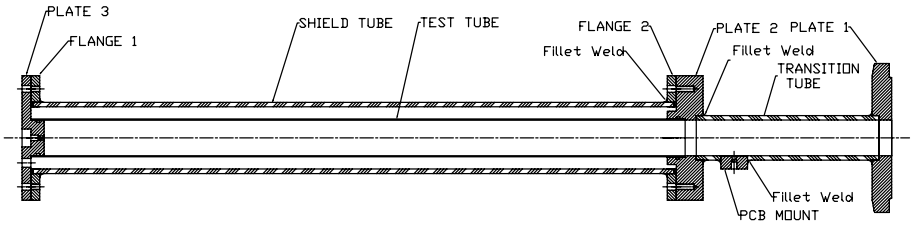

W.M. Beltman
University of Twente
Faculty of Mechanical Engineering
P.O. Box 217, 7500 AE Enschede
The Netherlands

E.N. Burcsu
California Institute of Technology
Graduate Aeronautical Laboratories
Pasadena, CA 91125
U.S.A.

J.E. Shepherd
California Institute of Technology
Graduate Aeronautical Laboratories
Pasadena, CA 91125
U.S.A.

L. Zuhal
California Institute of Technology
Graduate Aeronautical Laboratories
Pasadena, CA 91125
U.S.A.

April 6, 1998

Summary

The internal shock loading of cylindrical shells can be represented as a step load advancing at constant speed. Several analytical models are available to calculate the structural response of shells to this type of loading. These models show that the speed of the shock wave is an important parameter. In fact, for a linear model of a shell of infinite length, the amplitude of the radial deflection becomes unbounded when the speed of the shock wave is equal to a critical velocity. It is evident that simple (static) design formulas are no longer accurate in this case. The present paper deals with a numerical and experimental study on the structural response of a thin aluminum cylindrical shell to shock loading. Transient finite element calculations were carried out for a range of shock speeds. The results were compared to experimental results obtained with the GALCIT 6-inch shock tube facility. Both the experimental and the numerical results show an increase in amplitude near the critical velocity, as predicted by simple steady state models for shells of infinite length. However, the finite length of the shell results in some transient phenomena. These phenomena are related to the reflection of structural waves and the development of the deflection profile when the shock wave enters the shell.

Nomenclature

E	Young's modulus	N/m^2
G	shear modulus	N/m^2
N_{xx}	axial stress resultant	N/m
$N_{\theta\theta}$	circumferential stress resultant	N/m
M_{xx}	moment resultant	N
Q_x	shear stress resultant	N/m
R	shell mean radius	m
f	frequency	Hz
h	shell thickness	m
i	imaginary unit	
k	wave number	$1/m$
l	shell length	m
m, m_1, m_2	characteristic roots	
n	characteristic root	
p_1	pre-shock pressure	Pa
p_2	post-shock pressure	Pa
p_{atm}	atmospheric pressure	Pa
t	time	s
u	axial deflection	m
$\overline{u}$	dimensionless axial deflection	
v	shock speed	m/s
v_d	dilatational wave speed	m/s
v_s	shear wave speed	m/s
w	radial deflection	m
$\overline{w}$	dimensionless radial deflection	
$\overline{w}_b$	dimensionless radial deflection, bending	
$\overline{w}_b^I$	dimensionless radial deflection region I	
$\overline{w}_b^{II}$	dimensionless radial deflection region II	
x	axial coordinate	m
α	characteristic root	
β	shell thickness parameter	
$\overline{\eta}$	dimensionless (moving) axial coordinate	

Δp	pressure difference across shell	Pa
κ	shear correction factor	
ν	Poisson's ratio	
ρ	density	kg/m^3
ψ	rotation	
$\overline{\psi}$	rotation	
Λ_j	excitation parameter (j=1,2)	
Λ_j^s	excitation parameter (j=1,2)	

Contents

List of Figures

List of Tables

Acknowledgments

This report is the result of a six months stay at the Graduate Aeronautical Laboratories of the California Institute of Technology. I was offered the possibility to join Caltech as a "Visitor in Aeronautics" during this period. This stay would not have been possible without the help of several persons and institutions. First of all I thank my advisor in The Netherlands, Prof. Tijdeman, for his continuing efforts to support me and other students. He made it possible to interrupt my PhD project at the University of Twente for a stay at Caltech. The generous support from the department of Applied Mechanics and the Faculty of Mechanical Engineering enabled a good quality of life in beautiful sunny (?, El Nino) Southern California. In this respect I also thank Prof. Huetink and Prof. Grootenboer.

The work at Caltech was both challenging and rewarding. I thank my colleagues at the Explosion Dynamics Group and my advisor, Prof. Shepherd, for creating a very stimulating and pleasant environment both inside and outside the lab. The work could not have been completed without the help of Raza, Mike and Eric in the Guggenheim sub-basement lab.

This research was sponsored by the Netherlands Organization for Scientific Research (NWO). Their support is gratefully acknowledged.

Pasadena, April 6, 1998

Marco Beltman

Chapter 1

Introduction

1.1 General introduction

At the Aeronautics department of the California Institute of Technology the behaviour of shock waves and detonations is studied. A detonation test tube facility and several shock tube facilities are available for laboratory experiments. During a shock or detonation test, the tube is exposed to high pressures. The detonation or shock wave propagates down the tube and therefore the tube is subjected to a moving pressure load. The problem has a strong dynamic nature. This report deals with the structural response of cylindrical shells to moving pressure loads. The results can be used for the analysis of tube systems, both in industrial and military applications.

1.1.1 Shock tube

Shock tubes are used to investigate shock wave propagation. A shock is created by the driver of the shock tube. The shock wave then travels down the tube at a nearly constant speed. A typical measured pressure history for a point in the tube is given in figure 1.1. The figure shows the measured pressure versus time for a thin aluminium tube in the GALCIT 6 inch shock tube facility. The character of the shock loading is a stepwise varying pressure, advancing at constant speed. Therefore the loading for a shock tube will be represented by a step profile in this report. The load is characterized by the pre-shock pressure p_1, the post-shock pressure p_2 and the velocity v (see figure 1.1)

1.1.2 Detonation tube

A detonation consists of a shock wave and a reaction zone that are tightly coupled. For prompt detonation, at one side of the detonation tube an explosion is initiated by a high explosive. The detonation then travels down the tube at a nearly constant speed: the Chapman-Jouguet velocity. The pressure history for this type of loading can be characterized by the initial pressure p_1, the peak

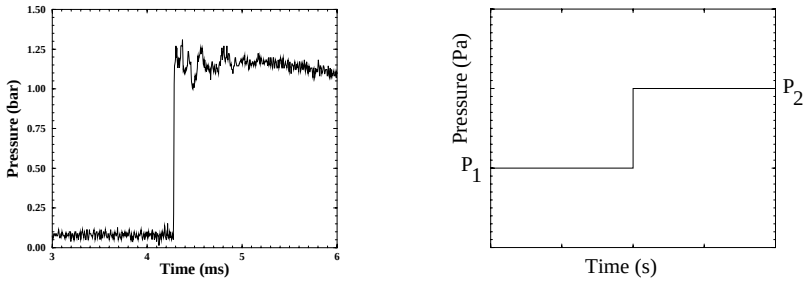

Figure 1.1: Pressure versus time for shock loading

pressure p_2, the final pressure p_∞ and the exponential decay factor T (see figure 1.2).

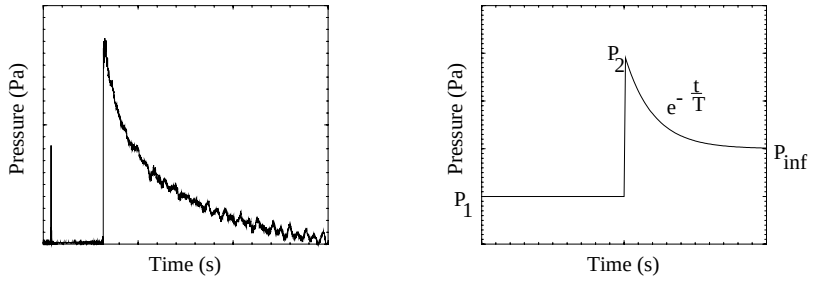

Figure 1.2: Pressure versus time for detonation loading

For the prompt detonation case the pressure loads are well defined. However, the case of deflagration to detonation (DDT) is more complex. In the deflagration to detonation case there intitially is no detonation but only a propagating flame. The flame compresses the unreacted gas ahead of the flame and a spontaneous explosion can occur in this unreacted gas. This can lead to extremely high pressures. However, for a properly operated detonation facility the chance of a DDT event is very low.

1.1.3 Structural response

In figure 1.3 the measured circumferential strain versus time for shock loading of a thin aluminium tube is depicted.

The measured strain shows a sharp peak when the shock passes. For the shock under consideration, the strain exceeds the equivalent static strain by a factor 3. This example indicates that a simple static model of the tube cross

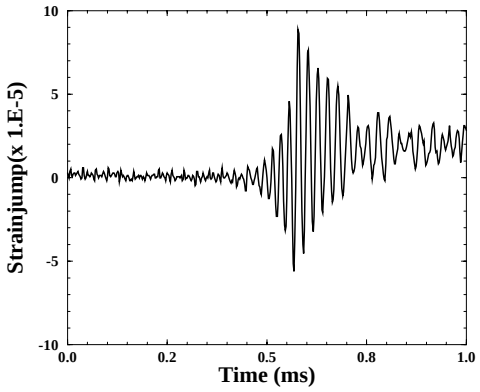

Figure 1.3: Strain history for shock loading

section is not sufficient to predict this large strain. One could calculate the maximum strains and stresses corresponding to the maximum load, but this would result in stresses and strains that are too low. The key question now is: what is the cause of the high strain? A somewhat more sophisticated model takes into account the step character of the loading. However, unfortunately the difference with the simple static cross-sectional model is small, even when the loading is located near a support.

It is now clear that the cause of the high strain is of a dynamic nature. The most simple dynamical model is the dynamical version of the cross-sectional model. This model describes the radial (breathing) motion of the cylinder cross-section. For shock loading, the maximum strain is twice the equivalent static strain. Although significantly higher strains are obtained with this model, it is clear that an essential mechanism is still missing.

Experiments on shock tubes and gun tubes revealed that the speed of propagation of the shock wave is an important parameter. The high strains in the experiments are due to flexural motion of the cylinder wall. Several models were developed to describe this phenomenon, some including for instance rotatory inertia and transverse shear deformation. The flexural models predict the existance of a so-called critical velocity. When the shock travels at the critical speed, the solution for the radial tube motion becomes unbounded. Evidently, damping, non-linearities and plastic deformation will be the controlling mechanisms in this case. Nevertheless, the flexural models are able to predict the high strains that were found in the experiments.

1.2 Formulation of the problem

The main aims of this study are:

- prediction of the structural reponse of a cylindrical tube to shock or detonation loading and comparison with experimental data
- development of design criteria and design methods for tubes that are subjected to shock or detonation loading

Special attention will be paid to the following subjects:

- end effects
  In most models the tube is assumed to be infinite in length. However, in practical situations one deals with short tube sections that are connected by flanges. This will have important implications for the structural response and the design of the tube.
- limits of predictability
  An important issue to keep in mind when developing models and design concepts, is the subject of "limited predictability". Due to variation in the input data, *e.g.* material properties or geometrical properties, there is a degree of uncertainty in the results.

1.3 Outline

This research is carried out in a number of steps. Accordingly, the report is divided into three parts. In part I, the general theory for the structural response of tubes to shock or detonation loading is presented. A number of analytical models is described. These models are not new. However, for the present study they were all rewritten into the same notation in order to put them into perspective. Simple analytical models were developed to describe the transient response of a finite length shell. Finally, in order to describe more complicated boundary conditions, a finite element model was developed.

In part II of this report an analysis is presented for the GALCIT 6 inch shock tube. Results from calculations and experiments are compared for a thin aluminium tube subject to shock loading. The shock tube problem is well defined and the important mechanisms and concepts can be analyzed for this setup.

Finally, an analysis of the detonation tube problem will be described in part III. The detonation tube is a thick walled tube that is constructed of relatively short segments, connected by flanges. Theory and experiments will be used to develop methods in the design process.

Chapter 2

Analytical models

The analytical model used in this section was presented by Tang (1965). His formulation was rewritten to enable an easy comparison with the model presented by Simkins (1987).

2.1 Basic equations

The basic equations for this model are

$$\frac{\partial N_{xx}}{\partial x} = \rho h \frac{\partial^2 u}{\partial t^2} \quad ; \quad \frac{\partial M_{xx}}{\partial x} - Q_x = \rho h^3 \frac{\partial^2 \psi}{\partial t^2}$$

$$\frac{\partial Q_x}{\partial x} - \frac{N_{\theta\theta}}{R} + \Delta p = \rho h \frac{\partial^2 w}{\partial t^2}. \tag{2.1}$$

The stress resultants N_{xx}, $N_{\theta\theta}$ and M_{xx} are

$$N_{xx} = \frac{Eh}{1-\nu^2}\left[\frac{\partial u}{\partial x} + \nu \frac{w}{R}\right] \quad ; \quad M_{xx} = \frac{Eh^3}{12\,(1-\nu^2)} \frac{\partial \psi}{\partial x}$$

$$N_{\theta\theta} = \frac{Eh}{1-\nu^2}\left[\nu \frac{\partial u}{\partial x} + \frac{w}{R}\right] \quad ; \quad Q_x = \kappa G h \left[\psi + \frac{\partial w}{\partial x}\right], \tag{2.2}$$

where κ is the shear correction factor and ψ is the rotation. The value of the shear correction factor is determined from the condition that waves with very small wave numbers propagate at the speed of Rayleigh waves. Rotary inertia and transverse shear deformation are included in the equations. Axial prestress is neglected. For a discussion on axial prestress the reader is referred to Reismann (1965).

We introduce the following dimensionless quantitities to facilitate discussion of these equations

$$\overline{u} = \frac{u}{h} \quad ; \quad \overline{w} = \frac{w}{h} \quad ; \quad \overline{\psi}_x = \frac{1}{\sqrt{12}} \psi_x \quad ; \quad \overline{\eta} = \frac{\sqrt{12}}{h}\left[x - vt\right]. \tag{2.3}$$

The following parameters are used in the analysis:

$$\begin{aligned}
\Lambda_j &= \frac{(p_j - p_{atm})\, R^2}{Eh^2} && : \text{excitation parameters (j} = 1, 2) \\
v_d &= \sqrt{\frac{E}{\rho\,(1-\nu^2)}} && : \text{dilatational wave velocity} \\
v_s &= \sqrt{\frac{\kappa G}{\rho}} && : \text{shear wave velocity} \\
\beta &= \frac{h}{\sqrt{12}R} && : \text{shell thickness parameter...}
\end{aligned} \tag{2.4}$$

The first relation in Eq. 1 is used to eliminate the axial displacement $\overline{u}$. The radial displacement $\overline{w}$ is now split up into two parts:

$$\overline{w} = \overline{w}_b + \overline{w}_s \quad ; \quad \overline{\psi}_x = -\frac{\partial \overline{w}_b}{\partial \overline{\eta}}. \tag{2.5}$$

Inserting these expressions into Eqs. 2.1 and 2.2, and integrating with respect to $\overline{\eta}$ gives

$$\overline{w}_s = -\left(\frac{v_d}{v_s}\right)^2 \left[1 - \left(\frac{v}{v_d}\right)^2\right] \frac{\partial^2 \overline{w}_b}{\partial \overline{\eta}^2}. \tag{2.6}$$

The final result for this model is the following differential equation:

$$A_4 \frac{\partial^4 \overline{w}_b}{\partial \overline{\eta}^4} + A_2 \frac{\partial^2 \overline{w}_b}{\partial \overline{\eta}^2} + A_0 \overline{w}_b = F\left(\overline{\eta}\right) \tag{2.7}$$

where

$$\begin{aligned}
A_4 &= \left[\left(\frac{v}{v_d}\right)^2 - 1\right]\left[\left(\frac{v}{v_s}\right)^2 - 1\right] \\
A_2 &= \left(\frac{v}{v_d}\right)^2 \left[1 + \beta^2 \left(\frac{v_d}{v_s}\right)^2\right] - \beta^2 \left(1 - \nu^2\right) \left(\frac{v_d}{v_s}\right)^2 \\
A_0 &= \beta^2 + \frac{\beta^2 \nu^2}{\left[\left(\frac{v}{v_d}\right)^2 - 1\right]} \\
F\left(\overline{\eta}\right) &= \beta^2 \left(1 - \nu^2\right) \left\{\Lambda_1 + \left(\Lambda_2 - \Lambda_1\right) \left[1 - H\left(\overline{\eta}\right)\right]\right\}.
\end{aligned} \tag{2.8}$$

For $v_s \to \infty$ and $\left(\frac{v}{v_d}\right) \ll 1$, the model reduces to that described by Simkins (1987). In the Simkins model, the effects of transverse shear and rotary inertia are neglected.

2.2 Dispersion equation

The solution of Eq. 2.7 is composed of a homogeneous and inhomogeneous part. By assuming an exponential dependence, $\overline{w} \sim exp(\alpha\overline{\eta})$, for the homogeneous part, the following dispersion equation is obtained:

$$A_4\ \alpha^4 + A_2\ \alpha^2 + A_0 = 0 \tag{2.9}$$

where α is related to the wave number k through

$$k = \frac{\sqrt{12}\alpha}{ih}. \tag{2.10}$$

The characteristic roots can be determined for each value of v by simply using the quadratic formula. Based on the values of the speed v, five different cases can be distinguished. In the present investigation, only the first two cases are relevant. In the first case, $0 < v < v_{c0}$, the values of α are complex: $\alpha = \pm n \pm im$. In the second case, $v_{c0} < v < v_{c1}$, the values of α are purely imaginary: $\alpha = \pm im_1$ and $\alpha = \pm im_2$. The speed v_{c0} is the first critical velocity. The values of each critical velocity can be calculated from the vanishing of the discriminant

$$A_2^2 - 4A_0A_4 = 0. \tag{2.11}$$

For the Tang model, there are four critical velocities. The other critical velocities are v_{c1}: the shear wave speed v_s, v_{c2}: the dilatational wave speed in a bar $v_d\sqrt{1-\nu^2}$, and v_{c3}: the dilatational wave speed v_d. For a more detailed discussion on these five cases, the reader is referred to Tang (1965).

2.3 Case 1: $0 < v < v_{c0}$

Case 1 is referred to as the subcritical case. The axial domain is split up into two regions. Region I is after the shock, $\overline{\eta} < 0$, and region II is before the shock, $\overline{\eta} \leq 0$. In the subcritical case there are four complex roots. Continuity conditions have to be satisfied at $\overline{\eta} = 0$ for displacement, rotation, moment, and shear. The solution also must remain bounded for $\overline{\eta} \to \pm\infty$. The final solution is

$$\begin{aligned} \overline{w}_b^I &= \Lambda_1^s - (\Lambda_2^s - \Lambda_1^s) \cdot \\ &\quad \left\{1 + \frac{1}{8}e^{n\overline{\eta}}\left[-4\cos(m\overline{\eta}) + 2\frac{n^2-m^2}{nm}\sin(m\overline{\eta})\right]\right\} \end{aligned} \tag{2.12}$$

$$\begin{aligned} \overline{w}_b^{II} &= \Lambda_1^s + (\Lambda_2^s - \Lambda_1^s) \cdot \\ &\quad \left\{\frac{1}{8}e^{-n\overline{\eta}}\left[4\cos(m\overline{\eta}) + 2\frac{n^2-m^2}{nm}\sin(m\overline{\eta})\right]\right\} \end{aligned} \tag{2.13}$$

where

$$\Lambda_i^s = \frac{\beta^2\left(1-\nu^2\right)}{A_0}\Lambda_i. \tag{2.14}$$

The solution is oscillatory with an exponential decay as distance increases from the shock wave. Note that there are waves (precursors) ahead of the pressure front. The frequency of these precursor waves is equal to the frequency of the main signal, which exists after the shock has passed. When the velocity approaches v_{c0}, the value of n goes to zero and the solution becomes unbounded.

2.4 Case 2: $v_{c0} < v < v_{c1}$

Case 2 is referred to as the supercritical case. In the supercritical case there are only purely imaginary roots. The axial domain is also split up into two regions for this case. Continuity conditions must also be satisfied at $\overline{\eta} = 0$. However, the solution always remains bounded for $\overline{\eta} \to \pm\infty$, so other conditions have to be used to solve the problem. The extra restrictions for this case are a radiation condition; energy has to flow away from the pressure step. By using the group velocity concept, one finally has

$$\overline{w}_b^I = \Lambda_1^s + (\Lambda_2^s - \Lambda_1^s) \left\{ 1 + \left[\frac{m_2^2}{m_1^2 - m_2^2} \right] \cos(m_1 \overline{\eta}) \right\} \tag{2.15}$$

$$\overline{w}_b^{II} = \Lambda_1^s + (\Lambda_2^s - \Lambda_1^s) \left[\frac{m_1^2}{m_1^2 - m_2^2} \right] \cos(m_2 \overline{\eta}) \,. \tag{2.16}$$

The supercritical solution is purely oscillatory. Both before and after the shock the amplitude of the signals is constant, but the frequencies are different. The precursor wave contains a higher frequency signal than the main wave. As the velocity approaches v_{c0}, m_1 approaches m_2 and the solution becomes unbounded.

Chapter 3

Finite element model

The finite element calculations were carried out with the commercial package, IDEAS. In order to calculate the structural response, the problem was split up into two parts: a static calculation and a dynamic calculation. The static deformation corresponding to the pressure difference $(p_1 - p_{atm})$ was calculated with a linear-elastic static model. The dynamical response to a pressure step with amplitude $(p_2 - p_1)$ travelling at speed v was calculated with a transient, linear-elastic, finite-element model. Both results were combined to obtain the final solution.

3.1 Static calculation

The static deformation due to a pressure difference $(p_1 - p_{atm})$ was calculated. Rotary-symmetric, Mindlin-type, two-noded shell elements were used. The tube of interest was divided into 1500 elements (see section 3.2). Both ends of the tube were assumed to be fully clamped. The material and geometrical data are given in section 4.4.

3.2 Dynamic calculation

A transient, linear-elastic calculation was carried out to determine the structural response to a moving pressure step with amplitude $(p_2 - p_1)$. For the tube of interest, 1500 elements were used in the axial direction. This number was determined by accuracy and calculation time considerations. A single case was computed at a number of different resolutions using from 500 to 1500 elements. The maximum strain at several locations was plotted vs. the number of elements, and it was apparent that little gain in accuracy would result from using more than 1500 elements. For the strain signals of interest, with a speed of approximately 1000 m/s and a frequency of 35 kHz, this means a resolution of about 50 elements per wavelength. The loading of the shell is highly transient. In each node, a force was prescribed as a function of time.

The force history for each point depends on its axial location, the speed of the shock wave and the amplitude of the pressure step. The response was calculated up to the time of reflection of the shock wave at the end of the tube. For the time integration, 1000 intervals were used. For the problem of interest this means approximately 30 steps per cycle. The response was calculated with a normal mode superposition technique. The modes of vibration of the shell were calculated first. These eigenmodes were then used as a basis to calculate the transient shell response. In the calculations, 230 modes were used. The eigenfrequencies of these modes range from 3 kHz to 150 kHz.

Chapter 4

Experimental setup

4.1 GALCIT 6-inch shock tube facility

The experiments were carried out with the GALCIT 6-inch shock tube. The gas in the driver and the driven sections were separated by a 0.010 inch-thick aluminum sheet. Both the driver and the driven sections of the shock tube were evacuated before each run. The driven section was then slowly filled with air until the desired pressure p_1 was reached. Next, helium was slowly released into the driver section until the diaphragm could not withstand the pressure and ruptured. The aluminum diaphragm ruptured at a pressure difference of approximately 275 kPa. Symmetric rupture of the diaphragm was ensured by the use of sharp blades placed inside the shock tube. A shock wave was then created in the vicinity of the diaphragm and propagated toward the test section.

4.2 Tube assembly

The test section consisted of a test tube, a transition tube, and a shield tube (see Fig. 4.1). One end of the test tube was inserted into a hole in a flange at the end of the transition tube. The other end was connected to a 1.27 cm thick end plate. O-rings were used at both ends to make gas-tight seal connections.

The transition tube was 0.260 m long and made of 6.35 mm thick steel with an inner diameter of 50.8 mm. The transition tube had two flanges at both ends. One end of the tube was connected to the driven section of the 6-inch shock tube. The purpose of this tube was to prevent the expansion wave, generated at the area change, from entering the test tube during the duration of the test. The shield tube was made of 6.35 mm thick steel with an inner diameter of 88.9 mm. One end of the shield tube was bolted to the end plate and the other end to one of the flanges of the transition tube. The shield tube was designed to contain fragments in case of a failure of the test tube.

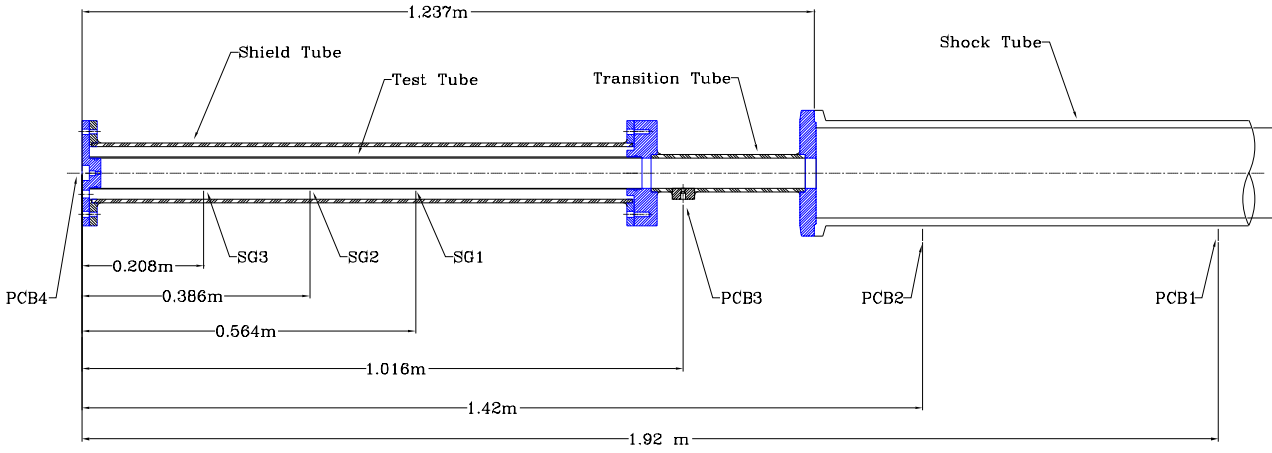

Figure 4.1: Tube assembly.

4.3 Instrumentation

PCB piezo-electric pressure transducers were used to determine the velocity and position of the shock wave. Two pressure transducers, 0.500 m apart, were installed near the end of the driven section of the shock tube. These transducers were used to measure the velocity in the shock tube. In addition, the output from the first transducer was used to trigger the data-acquisition system. Because the diameter of the test tube differs from the diameter of the shock tube, the shock wave travels at a different velocity inside the test tube. In order to determine the velocity of the shock wave inside the test tube, two additional pressure transducers were used. The third pressure transducer was installed near the end of the transition tube. The fourth pressure transducer was installed at the endplate, which was located 0.983 m from the third pressure transducer.

Three Micro Measurements strain gages were used to record the transient response of the test tube. The strain gages were installed 0.179 m apart, with the first strain gage located 0.382 m from the beginning of the test tube. The strain gages were mounted to measure the circumferential strain. The output from the strain gages was directed to unbalanced Wheatstone bridge circuits and amplified. The amplifiers were set at a gain of 100 and a bandwith of 100 kHz. In this way the jump in strain relative to the initial compressive strain was measured. The initial compressive strain was caused by the evacuation of the tube to the subatmospheric pressure p_1. Since the width of the strain gages is small compared to the structural wave length, the high frequency strain signals can be measured with sufficient accuracy.

4.4 Properties of the setup

The computed results are sensitive to variations in the input data. Therefore the material and geometrical properties of the tube were determined accurately. The inner diameter of the tube was measured at 8 points. The average inner diameter was 50.57 mm. The variation in inner diameter was smaller than 0.25 mm. The outer diameter of the test tube was measured at 12 equally spaced points. The average outer diameter was 53.77 mm, with a variation smaller than 0.25 mm. The total length of the tube was 0.933 m with a total mass of 0.679 kg. The effective length of the tube between the clamps is 0.889 m. The geometrical and material data that were used in the calculations are summarized in table 4.1.

R:	26.09	mm	ρ:	2773	kg/m^3
h:	1.601	mm	ν:	0.33	
l:	889.0	mm	E:	$72 \cdot 10^9$	N/m^2

Table 4.1: Geometrical and material properties

The critical velocity, calculated from the Tang model, is 963 m/s. Neglecting rotary inertia and transverse shear, the Simkins model, gives a critical velocity of 987 m/s.

4.5 Pressure traces

The initial pressure was varied between 6.8 kPa and 18.5 kPa in order to obtain different speed shock waves. This variation in pressure was accounted for in the data reduction by scaling the measured deformations with the equivalent static value based on the pressure jump across the shock. In Fig. 4.2 the pressure signal of the third transducer is plotted for a shock speed of 999.2 m/s.

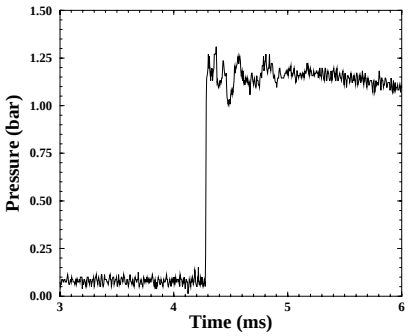

Figure 4.2: Pressure transducer 3 signal for $v = 999.2$ m/s.

Figure 4.2 shows that the pressure history is not a clearly defined step. After the shock has passed, the pressure gradually drops. Therefore it is difficult to clearly identify the post shock pressure p_2. The two PCB transducers in the driven section of the shock tube also show a slight decrease in pressure following the shock arrival. Due to the difficulty in defining the post-shock pressure, the shock wave arrival times were used to compute shock speed and then we back-calculated the pressure p_2 from the pressure p_1, the speed of the shock wave v, and the shock jump conditions.

Chapter 5

Results and discussion

5.1 Strain vs. time

In Fig. 5.1, the jump in circumferential strain vs. time is plotted for a subcritical shock speed of 967.8 m/s. In Fig. 5.2 the strain is plotted for a supercritical shock speed of 999.2 m/s. In both cases the strain significantly exceeds the equivalent static strains. There are some clear differences between the subcritical and the supercritical strain traces. For the subcritical case, the strain signal is oscillatory with an exponential decay, as predicted by the analytical models and the finite element model. The period of oscillation in the precursor wave and the bulk signal is approximately the same.

In the supercritical case, the frequency in the precursor wave is higher than the frequency of the bulk signal, as predicted by the theory. However, the analytical model predicts a constant amplitude in the precursor wave, which is clearly not the case in the experimental results. This is caused by transient effects due to the finite length of the tube. Initially the whole tube is at rest. Therefore it takes time for the deflection profile to develop. The fastest waves in the shell are the dilatational waves that travel at about 5000 m/s. Before these waves arrive, the shell is at rest. The finite element model is able to account for these transient effects. The shape of the envelope of the precursor wave is also an indication whether the speed of the shock wave is subcritical or supercritical.

Another transient effect is related to the reflection of structural waves at the end of the shell. Due to the reflections at the end, there will be an interference with forward travelling waves, which can lead to high strains especially near the critical velocity, when the precursor wave is relatively strong.

5.2 Dispersion curve

The experimental and finite element data are used to reconstruct the dispersion curve for this setup. First, the lowest critical velocity is computed from the

implicit solution of Eq. 2.11 by numerical iteration for the Tang model. The Simkins model is a special case for which an analytic solution can be found

$$v_{c0} = \sqrt{\frac{Eh}{\rho R}} \left[\frac{1}{3(1-\nu^2)} \right]^{1/4} . \tag{5.1}$$

The dispersion curve is computed from Eq. 2.9 and the frequency is defined by Eq. 2.10, where the wavenumber is given by $k = 2\pi f/v$ and f is the frequency.

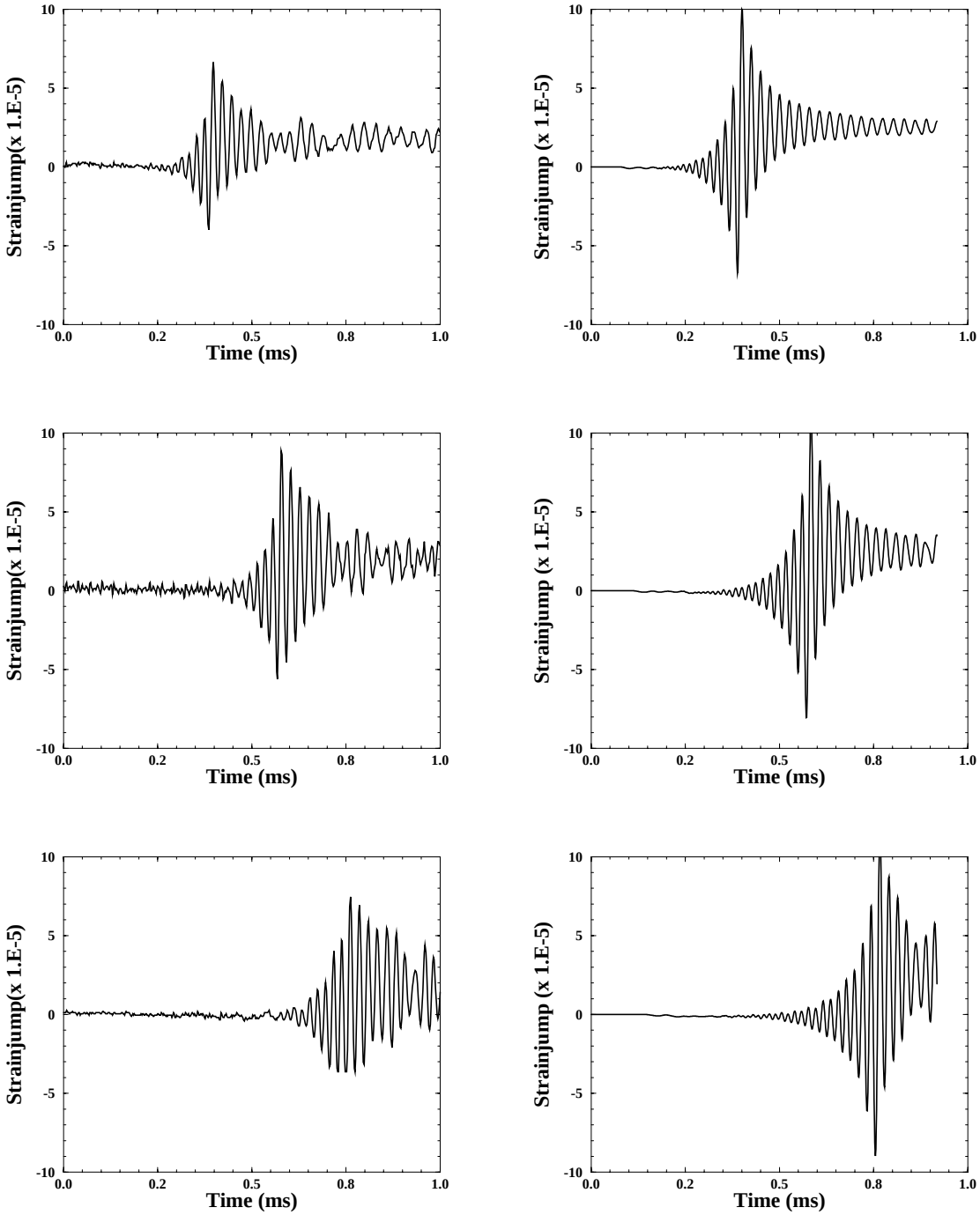

Figure 5.1: Strain vs. time for $v = 967.8\ m/s$. Left column: measurements. Right column: finite element results. Top: strain gage 1. Middle: strain gage 2. Bottom: strain gage 3.

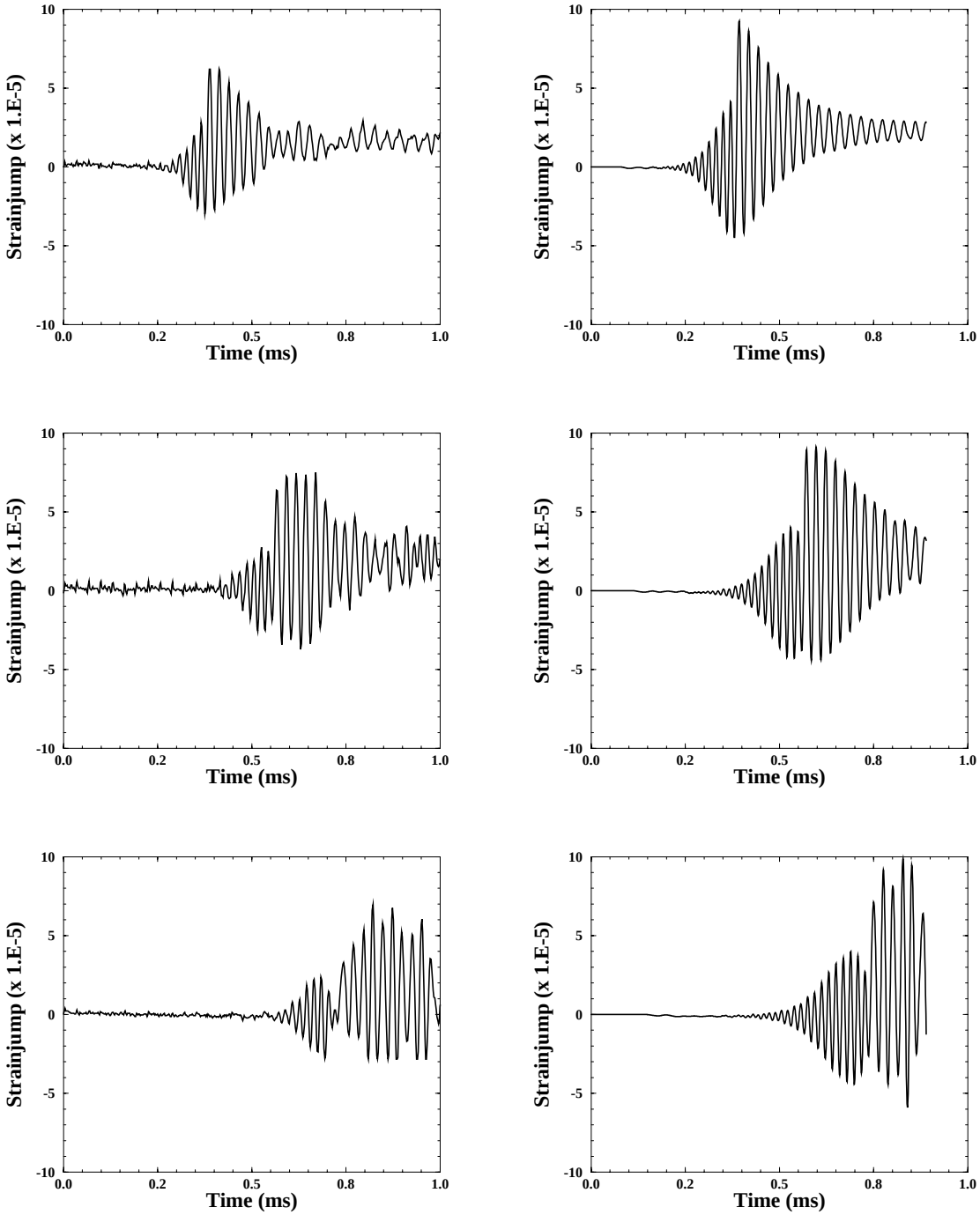

Figure 5.2: Strain vs. time for $v = 999.2\ m/s$. Left column: measurements. Right column: finite element results. Top: strain gage 1. Middle: strain gage 2. Bottom: strain gage 3.

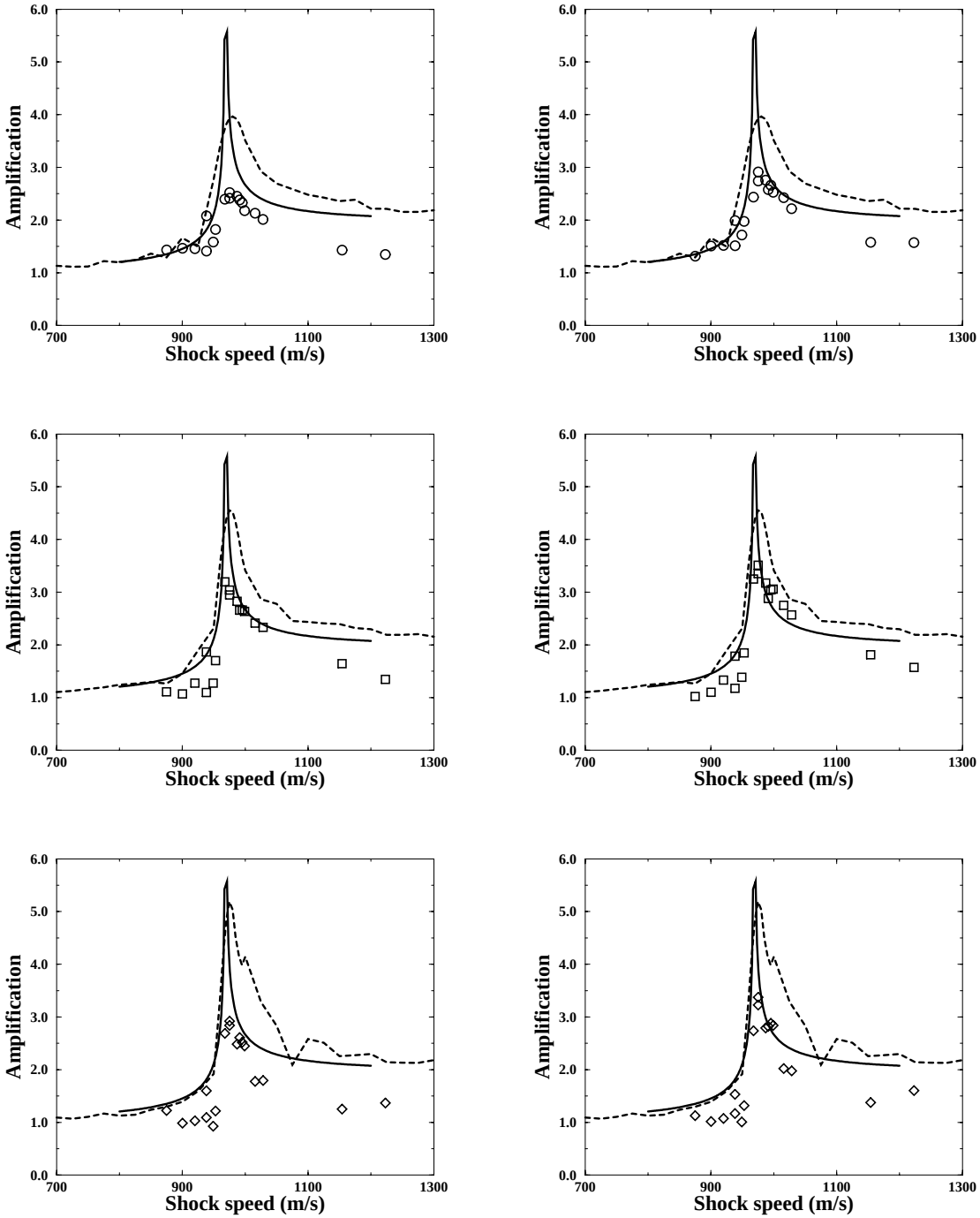

Figure 5.3: Amplification factor vs. velocity. Top: strain gage 1. Middle: strain gage 2. Bottom: strain gage 3. Left column: reference based on shock jump conditions. Right column: reference based on measured pressures. Solid line: Tang model. Dashed line: FEM. ○, □, ◇: Experiments.

The analytical expressions, given in Sections 2.3 and 2.4, for the strain history are used to curve fit the experimental data. The value(s) of the parameter m (subcritical case) or m_1 and m_2 (supercritical case) result from a nonlinear least-squares fitting procedure that minimized the deviations between model and experimental data over a portion of the strain history. These numbers represent the (dimensionless) frequency of oscillation. The values of these parameters are determined for each strain gage before and after the shock. For subcritical velocities, the curve fit is not very accurate. Due to the sharp exponential decay, the signal-to-noise ratio is poor and explains the large spread in results for these velocities. However, for velocities near the critical velocity or supercritical velocities, the frequency can be determined with a reasonable degree of accuracy.

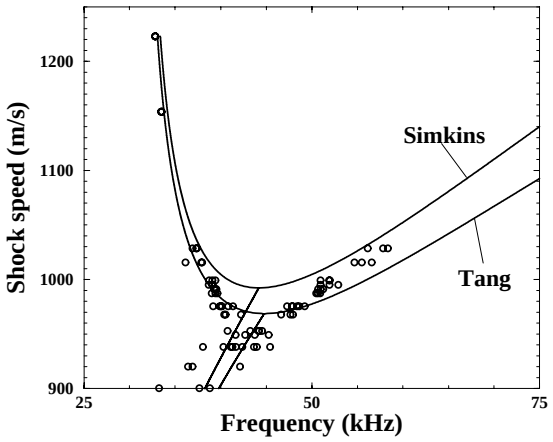

Figure 5.4: Dispersion curve.

The shock velocity is plotted vs. the frequency of oscillation in Fig. 5.4. The figure shows a clear branching of the dispersion curve as predicted by the analytical models. For supercritical velocities, the precursor wave contains the higher frequency signal (right branch), and the main wave contains the lower frequency signal (left branch). The dispersion curve offers an alternative way to extract the critical velocity from the experimental data. The branching in the experimental data occurs between 960 m/s and 970 m/s and is close to the values predicted by the analytical models. In general, the agreement between theory and experiment is reasonable.

5.3 Amplification Factor

The *dynamic amplification factor* is defined as the ratio between the maximum jump in strain from the initial state to the final state in the dynamical case and the static case. This dimensionless quantity indicates the degree of dynamic deformation; this is not affected by the initial prestress. The amplification factor is a function of shock speed v. For the analytical models presented in Section 2, the dynamic amplification factor becomes unbounded when the velocity of the shock wave is equal to the critical velocity.

The experimental and finite element results are now used to construct an amplification curve. When comparing these results to the results from the analytical models, one must be aware that certain transient phenomena are not included in the analytical models. Reflections will affect the strain history near the critical velocity, especially for the third strain gage. In the analytical models there is always a clear maximum. However, the experimental strain traces are more complicated due to the interference of the incident and reflected waves (see Fig. 5.1 and Fig. 5.2). It is therefore difficult to assign a peak value that is a consequence only of forward traveling waves, as in the analytical models. In the present investigation, the maximum jump in strain up to the time of reflection of the shock wave is used to calculate the amplification factor. This means that in some cases this value will include some contributions from reflected waves.

The calculated and measured amplification curves for the three strain gages are plotted in Fig. 5.3. In order to calculate the amplification factor, the maximum excursion in strain is divided by the static strain corresponding to the pressure difference $(p_2 - p_1)$. The left column of Fig. 5.3 is based on static strained computed from the initial pressure p_1, the shock speed v, and the shock jump conditions. The right column of Fig. 5.3 is based on the measured pressures. As shown, there are no visible differences between the two approaches.

The amplification curves clearly illustrate the importance of the critical velocity concept. For subcritical cases, the amplification factor is close to one, as expected for a uniform static load. For supercritical cases, the amplication factor is close to two, as expected for a suddenly-applied uniform load. The data show a maximum deflection near the critical velocity, however the measured maximum amplification factors are substantially lower than the values predicted by the finite element model. This discrepancy can partly be attributed to the fact that no damping was included in the calculations. The finite element model also predicts an increase of maximum amplification factor with distance (see Fig. 5.3). In the experimental results, the amplification factors for the first strain gage are lower than the following two gages, consistent with this prediction.

Conclusions

Calculations and experiments were carried out to study the structural response of a shell to internal shock loading. In the experiments, strains exceeding the static strain by a factor of up to 3.5 were obtained. The large strains can be explained with the critical velocity concept.

The general agreement between calculations and experiments is reasonable. The dispersion curve agrees well with the analytical predictions. The analytical models and the finite element model are able to predict the general shape of the amplification curves. However, near the critical velocity the predicted strains are too high.

Typical transient effects were observed in the experiments. These effects are related to the development of the deformation profile and the reflection of structural waves. These transient effects were taken into account in the finite element model.

This study provides a characterization only of the linear-elastic aspect of this problem. Plastic deformation and processes leading to material failure will be examined in future studies.

Acknowledgments

This research was sponsored by the Netherlands Organization for Scientific Research (NWO). Their support is gratefully acknowledged.

Bibliography

Reismann, H., 1965. Response of a pre-stressed cylindrical shell to moving pressure load. In S. Ostrach and R. Scanlon (Eds.), *Eighth Midwest Mechanics Conference*, pp. 349–363. Pergamon Press.

Simkins, T., 1987, July. Resonance of flexural waves in gun tubes. Technical Report ARCCB–TR–87008, US Army Armament Research, Development and Engineering Center, Watervliet, N.Y. 12189–4050.

Tang, S., 1965, October. Dynamic response of a tube under moving pressure. In *Proceedings of the American Society of Civil Engineers*, Volume 5, pp. 97–122. Engineering Mechanics Division.

Appendix A

Run conditions

Run	*V*	*P1*	*P2-c*	*P2-m*	*Patm*	*Tatm*
021	900.4	1.8478E+04	1.3978E+05	1.3629E+05	9.8292E+04	27.3
022	938.2	1.7237E+04	1.4164E+05	1.3318E+05	9.8305E+04	27.7
023	949.1	1.8064E+04	1.5198E+05	1.4134E+05	9.8285E+04	27.7
024	999.2	1.5237E+04	1.4238E+05	1.2474E+05	9.8258E+04	27.7
025	975.4	1.5789E+04	1.4055E+05	1.2549E+05	9.8258E+04	27.5
026	920.0	1.8892E+04	1.4934E+05	1.4398E+05	9.8258E+04	27.3
027	975.4	1.4479E+04	1.2911E+05	1.1373E+05	9.8285E+04	27.0
028	1015.7	1.3858E+04	1.3421E+05	1.1955E+05	9.8278E+04	27.0
029	1028.5	1.3100E+04	1.3023E+05	1.1947E+05	9.8285E+04	26.8
030	874.8	1.8064E+04	1.2916E+05	1.3884E+05	9.8518E+04	26.5
031	952.7	1.6616E+04	1.4122E+05	1.3143E+05	9.8532E+04	27.0
032	967.8	1.5927E+04	1.3977E+05	1.3770E+05	9.8512E+04	27.0
033	938.2	1.5237E+04	1.2550E+05	1.3041E+05	9.8498E+04	27.0
034	991.2	1.5168E+04	1.3962E+05	1.3013E+05	9.8498E+04	27.3
035	1223.0	6.8948E+03	9.7222E+04	0.8409E+05	9.8492E+04	27.4
036	1154.0	9.5837E+03	1.2009E+05	1.0992E+05	9.8492E+04	27.5
037	995.2	1.5513E+04	1.4378E+05	1.2767E+05	9.8492E+04	27.7
038	987.2	1.5513E+04	1.4129E+05	1.2753E+05	9.8492E+04	28.0

Table A.1: Test conditions

Appendix B

Curve fit data

Run	*B,A,T*	*V*	*Trans*	*C1*	*C2*	*n1,m1*	*m1,m2*	*offset*	*lower*	*upper*	*time*	*Notes*
021	B	900.4	1	-1.61E-5	2.56E-4	0.0438	0.1252	1.24E-3	1070	1085	1.67E-3	
021	B	900.4	2	-1.44E-5	4.40E-4	0.0457	0.1073	1.28E-3	1160	1185	1.85E-3	
021	B	900.4	3	-1.82E-5	1.19E-4	0.0355	0.1215	1.27E-3	1265	1283	2.05E-3	
021	A	900.4	1	-4.44E-5	4.85E-5	0.0099	0.1299	1.12E-3	1086	1130	1.70E-3	Bad fit
021	A	900.4	2	4.98E-6	1.17E-7	0.0008	0.1240	1.15E-3	1186	1250	1.85E-3	Bad fit
021	A	900.4	3	-4.79E-5	5.13E-5	0.0099	0.1324	1.08E-3	1284	1325	2.05E-3	Bad fit
021	T	900.4		-1.88E-5	2.86E-5	0.0357	0.1243					
022	B	938.2	1	-1.68E-5	8.11E-4	0.0182	0.1312	1.26E-3	1020	1061	1.6E-3	
022	B	938.2	2	-1.66E-5	8.51E-4	0.0256	0.1248	1.29E-3	1120	1155	1.85E-3	
022	B	900.4	3	-1.68E-5	1.30E-4	0.0322	0.1178	1.24E-3	1220	1251	2.E-3	
022	A	938.2	1	-1.50E-3	1.50E-5	0.0297	0.1410	1.10E-3	1060	1090	1.60E-3	Bad fit
022	A	938.2	2									Noisy data: no fit
022	A	938.2	3	-1.26E-5	1.40E-5	0.0066	0.1272	1.07E-3	1252	1320	2.00E-3	Bad fit
022	T	900.4		-1.91E-5	2.94E-5	0.0258	0.1268					
023	B	949.1	1	-1.60E-5	1.633E-5	0.0169	0.1339	1.22E-3	990	1063	1.60E-3	
023	B	949.1	2	-1.60E-5	1.26E-5	0.0168	0.1306	1.22E-3	1100	1155	1.81E-3	
023	B	949.1	3	-1.76E-5	5.57E-5	0.0154	0.1192	1.27E-3	1200	1250	2.00E-3	bad fit
023	A	949.1	1	-2.70E-5	3.19E-5	0.0172	0.1385	1.20E-3	1064	1100	1.60E-3	
023	A	949.1	2	-2.31E-5	2.81E-5	0.0068	0.1396	1.07E-3	1156	1200	1.81E-3	
023	A	949.1	3	-2.87E-6	4.17E-6	0.0043	0.1274	1.14E-3	1280	1330	2.00E-3	bad fit
023	T	949.1		-1.89E-5	3.16E-5	0.0220	0.1275					
024	B	999.2	1	-1.78E-5	2.82E-5	0.0985	0.1481	1.19E-3	1000	1025	1.50E-3	
024	B	999.2	2	-1.60E-5	2.56E-5	0.1003	0.1511	1.19E-3	1070	1115	1.8E-3	
024	B	999.2	3	-1.69E-5	2.80E-5	0.1006	0.1509	1.17E-3	1155	1185	1.85E-3	
024	A	999.2	1	-2.29E-5	2.39E-5	0.1146	0.1719	1.09E-3	1027	1060	1.50E-3	
024	A	999.2	2	-2.04E-5	2.30E-5	0.1136	0.1513	1.14E-3	1120	1170	1.7E-3	
024	A	999.2	3	-2.23E-6	2.15E-6	0.1126	0.1599	1.14E-3	1235	1300	1.85E-3	
024	T	999.2		-1.96E-5	3.00E-5	0.1115	0.1500					

Table B.1: Results curve fit

Run	*B,A,T*	*V*	*Trans*	*C1*	*C2*	*n1,m1*	*m1,m2*	*offset*	*lower*	*upper*	*time*	*Notes*
025	B	975.4	1	-1.73E-5	2.24E-4	0.0122	0.1440	1.28E-3	1000	1035	1.60E-3	
025	B	975.4	2	-1.82E-5	1.25E-5	0.0108	0.1427	1.26E-3	1090	1127	1.8E-3	
025	B	975.4	3	-1.75E-5	2.85E-5	0.0066	0.1408	1.24E-3	1160	1217	1.90E-3	
025	A	975.4	1	-2.00E-5	2.06E-5	0.0046	0.1188	1.07E-3	1035	1100	1.52E-3	
025	A	975.4	2	-7.90E-6	9.57E-6	0.0033	0.1195	1.15E-3	1126	1200	1.75E-3	
025	A	975.4	3	-6.85E-6	6.96E-6	0.0028	0.1216	1.15E-3	1216	1300	1.90E-3	
025	T	975.4		-1.95E-5	2.95E-5	0.0064	0.1292					
026	B	920.0	1	-1.67E-5	2.46E-9	0.0361	0.1330	1.25E-3	1070	1086	1.67E-3	
026	B	920.0	2	-1.56E-5	8.00E-6	0.0252	0.1165	1.28E-3	1160	1182	1.82E-3	
026	B	920.0	3	-1.70E-5	1.29E-4	0.0313	0.1150	1.28E-3	1260	1277	2.04E-3	
026	A	920.0	1	-2.10E-5	2.36E-5	0.0116	0.1033	1.27E-3	1120	1140	1.67E-3	Noisy data: bad fit
026	A	920.0	2									Noisy data: no fit
026	A	920.0	3	-9.19-6	1.05E-5	0.0116	0.1159	1.22E-3	1277	1310	2.00E-3	Noisy data: bad fit
026	T	920.0		-1.87E-5	3.08E-5	0.0310	0.1256					
027	B	975.4	1	-1.77E-5	2.00E-4	0.0107	0.1465	1.27E-3	990	1023	1.55E-3	
027	B	975.4	2	-1.84E-5	1.77E-5	0.0084	0.1448	1.17E-3	1080	1113	1.73E-3	
027	B	975.4	3	-1.79E-5	1.41E-5	0.0064	0.1424	1.17E-3	1140	1204	1.88E-3	
027	A	975.4	1	-1.47E-5	1.43E-5	0.0038	0.1167	1.05E-3	1023	1100	1.54E-3	
027	A	975.4	2	-5.55E-6	5.70E-6	0.0023	0.1192	1.13E-3	1113	1180	1.73E-3	
027	A	975.4	3	-5.10-6	5.11E-6	0.0023	0.1231	1.13E-3	1204	1250	1.91E-3	
027	T	975.4		-1.98E-5	2.71E-5	0.0064	0.1292					
028	B	1015.7	1	-1.80E-5	2.47E-5	0.0916	0.1564	1.17E-3	970	990	1.55E-3	
028	B	1015.7	2	-1.55E-5	2.33E-5	0.0969	0.1618	1.26E-3	1040	1070	1.81E-3	
028	B	1015.7	3	-1.73E-5	3.03E-5	0.0837	0.1587	1.19E-3	1130	1150	1.8E-3	
028	A	1015.7	1	-2.30E-7	-6.60E-7	0.1086	0.1077	1.19E-3	1020	1060	1.50E-3	
028	A	1015.7	2	-1.04E-5	1.32E-5	0.1083	0.1332	1.22E-3	1130	1200	1.70E-3	
028	A	1015.7	3	-2.09E-5	1.92EE-5	0.1033	0.2526	1.10E-3	1190	1250	1.80E-3	
028	T	1015.7		-1.99E-5	2.84E-5	0.1062	0.1576					

Table B.2: Results curve fit

Run	*B,A,T*	*V*	*Trans*	*C1*	*C2*	*n1,m1*	*m1,m2*	*offset*	*lower*	*upper*	*time*	*Notes*
029	B	1028.5	1	-1.77E-5	1.92E-5	0.0993	0.1585	1.14E-3	965	990	1.45E-3	
029	B	1028.5	2	-1.77E-5	3.15E-5	0.0777	0.1633	1.19E-3	1020	1065	1.75E-3	
029	B	1028.5	3	-1.79E-5	3.48E-5	0.0703	0.1648	1.12E-3	1100	1130	1.83E-3	
029	A	1028.5	1	-3.40E-6	7.37E-7	0.1042	0.1055	1.15E-3	1000	1100	1.50E-3	
029	A	1028.5	2	-2.23E-5	2.24E-5	0.1056	0.1714	1.20E-3	1140	1190	1.75E-3	
029	A	1028.5	3	-2.18E-5	1.98E-5	0.1054	0.1901	1.04E-3	1180	1220	1.80E-3	
029	T	1028.5		-2.01E-5	2.77E-5	0.1029	0.1626					
030	B	874.8	1	-1.65E-5	1.83E-5	0.0366	0.1293	1.23E-3	1070	1083	1.66E-3	
030	B	874.8	2	-1.83E-5	1.21E-5	0.0310	0.1529	1.23E-3	1170	1186	1.87E-3	Noisy data: bad fit
030	B	874.8	3	-1.65E-5	1.05E-4	0.0242	0.1360	1.23E-3	1270	1291	2.08E-3	
030	A	874.8	1									Noisy data: no fit
030	A	874.8	2	-2.20E-6	5.86E-6	0.0132	0.1432	1.21E-3	1186	1206	1.87E-3	Noisy data: bad fit
030	A	874.8	3	-3.60E-6	8.28E-6	0.0231	0.1447	1.24E-3	1288	1310	2.08E-3	
030	T	874.8		-1.90E-5	2.62E-5	0.0409	0.1227					
031	B	952.7	1	-1.71E-5	1.72E-5	0.0160	0.1358	1.20E-3	1015	1051	1.60E-3	
031	B	952.7	2	-1.78E-5	2.46E-5	0.0136	0.1348	1.22E-3	1100	1143	1.78E-3	
031	B	952.7	3	-1.71E-5	1.94E-5	0.0078	0.1243	1.27E-3	1210	1238	2.01E-3	
031	A	952.7	1	-8.04E-6	1.11E-5	0.0110	0.1319	1.20E-3	1050	1090	1.60E-3	
031	A	952.7	2	-4.62E-6	6.42E-6	0.0069	0.1346	1.20E-3	1142	1180	1.78E-3	
031	A	952.7	3	-2.68E-5	2.81E-5	0.0105	0.1697	1.09E-3	1236	1250	1.97E-3	Reflections: bad fit
031	T	975.4		-1.93E-5	2.94E-5	0.0206	0.1277					
032	B	967.8	1	-1.69E-5	2.70E-5	0.0123	0.1439	1.19E-3	1000	1036	1.56E-3	
032	B	967.8	2	-1.67E-5	1.99E-5	0.0110	0.1430	1.17E-3	1080	1127	1.75E-3	
032	B	967.8	3	-1.69E-5	2.11E-5	0.0069	0.1400	1.21E-3	1160	1219	1.92E-3	
032	A	967.8	1	-6.18E-6	7.90E-6	0.0050	0.1217	1.17E-3	1035	1085	1.56E-3	
032	A	967.8	2	-5.81E-6	9.03E-6	0.0038	0.1212	1.17E-3	1126	1200	1.75E-3	
032	A	967.8	3	-7.42E-7	3.22E-6	0.0019	0.1267	1.19E-3	1218	1250	1.92E-3	
032	T	967.8		-1.95E-5	2.92E-5	0.0130	0.1287					

Table B.3: Results curve fit

Run	*B,A,T*	*V*	*Trans*	*C1*	*C2*	*n1,m1*	*m1,m2*	*offset*	*lower*	*upper*	*time*	*Notes*
033	B	938.2	1	-1.72E-5	3.37E-5	0.0145	0.1361	1.18E-3	1000	1032	1.56E-3	
033	B	938.2	2	-1.54E-5	7.36E-6	0.0079	0.1278	1.18E-3	1090	1126	1.80E-3	
033	B	938.2	3	-1.74E-5	2.64E-6	0.0056	0.1406	1.14E-3	1150	1200	1.95E-3	
033	A	938.2	1	-2.00E-6	4.86E-6	0.0058	0.1351	1.15E-3	1031	1075	1.56E-3	
033	A	938.2	2	6.31E-6	-5.51E-7	-0.0019	0.1290	1.10E-3	1126	1175	1.80E-3	
029	A	938.2	3	-5.05E-5	5.85E-6	0.0076	0.1273	1.16E-3	1225	1260	1.95E-3	
033	T	938.2		-1.97E-5	2.60E-5	0.0258	0.1268					
034	B	991.2	1	-1.67E-5	3.26E-5	0.1004	0.1486	1.27E-3	1000	1023	1.55E-3	
034	B	991.2	2	-1.92E-5	1.88E-5	0.1167	0.1494	1.16E-3	1085	1115	1.75E-3	
034	B	991.2	3	-1.79E-5	2.83E-5	0.1020	0.1502	1.15E-3	1150	1180	1.90E-3	
034	A	991.2	1	1.92E-6	6.17E-7	0.1152	0.1160	1.18E-3	1022	1062	1.53E-3	
034	A	991.2	2	1.66E-7	4.43E-7	0.1155	0.1160	1.21E-3	1114	1164	1.75E-3	
034	A	991.2	3	-2.15E-5	2.26E-5	0.1158	0.1646	1.16E-3	1210	1260	1.90E-3	
034	T	991.2		-1.97E-5	2.94E-5	0.1150	0.1454					
035	B	1223	1									Noisy data: no fit
035	B	1223	2									Noisy data: no fit
035	B	1223	3									Noisy data: no fit
035	A	1223	1	-2.22E-5	1.41E-5	0.0779	0.9370	0.86E-3	870	1000	1.15E-3	
035	A	1223	2	-2.00E-6	1.27E-6	0.0779	0.3264	0.92E-3	940	1040	1.33E-3	
035	A	1223	3	-2.18E-5	1.30E-6	0.0779	0.2953	0.92E-3	1015	1200	1.50E-3	
035	T	975.4		-2.16E-5	2.13E-5	0.0777	0.2152					
036	B	1154	1	-1.75E-5	3.79E-5	0.0502	0.2081	1.08E-3	870	920	1.30E-3	Noisy data: bad fit
036	B	1154	2	-1.72E-5	1.75E-5	0.0781	0.2033	1.00E-3	980	1002	1.50E-3	Noisy data: bad fit
036	B	1154	3	-1.89E-5	3.42E-5	0.0542	0.2083	1.07E-3	1050	1077	1.65E-3	Noisy data: bad fit
036	A	1154	1	-5.60E-6	-7.87E-6	0.0842	0.0826	1.04E-3	925	1100	1.35E-3	
036	A	1154	2	-1.85E-5	1.54E-5	0.0843	0.2335	0.98E-3	1000	1200	1.45E-3	
036	A	1154	3	-1.96E-5	1.37E-5	0.0844	0.2464	1.01E-3	1075	1200	1.65E-3	
036	T	1154		-2.10E-5	2.61E-5	0.0841	0.1988					

Table B.4: Results curve fit

Run	*B,A,T*	*V*	*Trans*	*C1*	*C2*	*n1,m1*	*m1,m2*	*offset*	*lower*	*upper*	*time*	*Notes*
037	B	995.2	1	-1.66E-5	4.35E-5	0.0914	0.1487	1.22E-3	1000	1025	1.60E-3	
037	B	995.2	2	-1.69E-5	3.15E-5	0.1043	0.1544	1.29E-3	1080	1115	1.80E-3	
037	B	995.2	3	-1.68E-5	3.60E-5	0.0939	0.1516	1.16E-3	1150	1180	1.90E-3	
037	A	995.2	1	2.95E-5	-2.92E-5	0.1129	0.0847	1.18E-3	1030	1080	1.55E-3	
037	A	995.2	2	-2.30E-5	2.46E-5	0.1141	0.1523	1.19E-3	1130	1170	1.75E-3	
037	A	995.2	3	-2.04E-5	2.05E-5	0.1141	0.1528	1.16E-3	1230	1280	1.90E-3	
037	T	938.2		-1.96E-5	3.03E-5	0.1132	0.1478					
038	B	987.2	1	-1.79E-5	3.17E-5	0.1009	0.1485	1.16E-3	1010	1030	1.55E-3	
038	B	987.2	2	-1.86E-5	3.07E-5	0.1080	0.1491	1.19E-3	1090	1120	1.75E-3	
038	B	987.2	3	-1.85E-5	3.72E-5	0.0950	0.1498	1.24E-3	1160	1185	1.90E-3	
038	A	987.2	1	-1.91E-5	2.10E-5	0.1148	0.1780	1.09E-3	1040	1070	1.55E-3	
038	A	987.2	2	-2.08E-5	2.25E-5	0.1160	0.1505	1.17E-3	1120	1180	1.70E-3	
038	A	987.2	3	-2.18E-5	2.12E-5	0.1166	0.1549	1.17E-3	1210	1280	1.85E-3	
038	T	987.2		-1.96E-5	2.97E-5	0.1172	0.1427					

Table B.5: Results curve fit

Appendix C

Amplification data

Run	*V*	*Gage 1*	*Gage 2*	*Gage 3*	*Lamec*	*Amp1c*	*Amp2c*	*Amp3c*	*Lamem*	*Amp1m*	*Amp2m*	*Amp3m*
021	900.4	3.9809	2.9091	2.6794	2.7170	1.4650	1.0707	0.9862	2.6388	1.5086	1.1024	1.0154
022	938.2	3.9298	3.0558	3.0367	2.7864	1.4104	1.0967	1.0898	2.5969	1.5133	1.1767	1.1694
023	949.1	4.7464	3.8278	2.7815	2.9995	1.5824	1.2761	0.9273	2.7612	1.7190	1.3863	1.0074
024	999.2	6.2010	7.5024	6.9665	2.8478	2.1775	2.6345	2.4463	2.4527	2.5282	3.0588	2.8403
025	975.4	6.7368	8.2297	7.9298	2.7944	2.4108	2.9451	2.8377	2.4571	2.7418	3.3494	3.2273
026	920.0	4.2616	3.7257	3.0112	2.9218	1.4586	1.2751	1.0306	2.8018	1.5210	1.3298	1.0747
027	975.4	6.4689	7.8086	7.5024	2.5675	2.5195	3.0413	2.9221	2.2231	2.9099	3.5125	3.3747
028	1015.7	5.7416	6.5072	4.7847	2.6957	2.1299	2.4139	1.7749	2.3673	2.4254	2.7488	2.0212
029	1028.5	5.2823	6.1244	4.7081	2.6235	2.0135	2.3344	1.7946	2.3825	2.2171	2.5706	1.9761
030	874.8	3.5598	2.7624	3.0494	2.4853	1.4323	1.1115	1.2270	2.7052	1.3159	1.0211	1.1272
031	952.7	5.0781	4.7528	3.3939	2.7909	1.8195	1.7030	1.2161	2.5716	1.9747	1.8482	1.3198
032	967.8	6.6475	8.8612	7.4641	2.7739	2.3964	3.1945	2.6908	2.7275	2.4372	3.2488	2.7366
033	938.2	5.1356	4.6061	3.9490	2.4697	2.0794	1.8650	1.5990	2.5797	1.9908	1.7855	1.5308
034	991.2	6.6411	7.4131	7.2727	2.7875	2.3825	2.6594	2.6090	2.5750	2.5791	2.8789	2.8243
035	1223.0	2.7177	2.7177	2.7687	2.0232	1.3433	1.3433	1.3685	1.7290	1.5718	1.5718	1.6013
036	1154.0	3.5407	4.0702	3.0941	2.4752	1.4305	1.6444	1.2500	2.2474	1.5755	1.8111	1.3767
037	995.2	6.6858	7.6427	7.2344	2.8730	2.3271	2.6602	2.5181	2.5121	2.6614	3.0424	2.8798
038	987.2	6.9155	7.9617	6.9984	2.8172	2.4547	2.8261	2.4842	2.5090	2.7563	3.1733	2.7893

Table C.1: Experimental results. Strains have to be multiplied by $1 \cdot 10^{-5}$

Structural response of shells to detonation and shock loading, part III: the GALCIT detonation tube

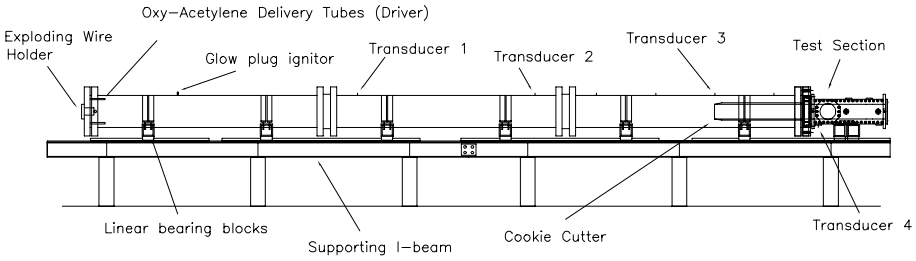

W.M. Beltman
University of Twente
Faculty of Mechanical Engineering
P.O. Box 217
7500 AE Enschede
The Netherlands

Advisor
Prof. J.E. Shepherd
California Institute of Technology
Graduate Aeronautical Laboratories
Pasadena, CA 91125
U.S.A.

May 17, 1999

Summary

The structural response of the GALCIT detonation tube to internal detonation loading was calculated and measured. Simple transient finite element models for clamped and simply supported thick walled tubes were developed for this purpose. The detonation tube was instrumented with a number of strain gages to monitor the circumferential strain as a function of time. A large number of experiments was carried out under different conditions. By varying the velocity of the detonation, the critical velocity of the tube was measured to be 1450 m/s. For this velocity strains were measured that exceed the equivalent static strain by a factor of about 4. This is an important result that has to be incorporated in future tube design. The detonation tube is constructed of three segments, connected by flanges and T-pieces. The reflection and interference of waves at flanges and at the end leads to high strains. The deflection profile has to develop as a function of distance. The connection between the tube parts cuts off this profile: in every tube section the build up of the profile starts over again. The tube can therefore be regarded as a series of three independant tube sections. The ratio between the cell size and the strutural wave length affects the maximum strain. When the cell size is of the same order of magnitude as the structural wave length, the flexural waves are excited well. Calculations and experiments show fair agreement: the finite element models are able to predict the maximum strains around the critical velocity.

Nomenclature

E	Young's modulus	N/m^2
GF	gage factor	
L	length of tube	m
P_{H2}	partial pressure H_2	Pa
P_{O2}	partial pressure O_2	Pa
P_{Ar}	partial pressure Ar	Pa
P_{cj}	Chapman-Jouguet detonation pressure	Pa
P_{for}	amplitude of forward travelling detonation ($=P_{cj}$)	Pa
P_{ref}	amplitude of reflected shock wave	Pa
P_{cj}	Chapman-Jouguet detonation pressure	Pa
R_1, R_2, R_3, R_4	resistor	Ω
R_g	resistance of strain gage	Ω
R_p	variable resistor	Ω
R_{in}	inner tube radius	m
R_{out}	outer tube radius	m
T	exponential decay factor	s
V_{in}	input voltage	V
V_{out}	output voltage	V
V_r	voltage difference	v
i	imaginary unit	
p_1	pre-shock pressure	Pa
p_2	post-shock pressure	Pa
p_{atm}	atmospheric pressure	Pa
p_∞	final pressure	Pa
t	time	s
v	load speed	m/s
v_{cr}	critical velocity	m/s
v_{cj}	Chapman-Jouguet detonation speed	m/s

x	axial coordinate	m
x_I	axial coordinate section I	m
x_{II}	axial coordinate section II	m
x_{III}	axial coordinate section III	m
ν	Poisson's ratio	
ρ	density	kg/m^3
λ	cell size	m
ε	circumferential strain	

Contents

List of Figures

List of Tables

Acknowledgments

This report is the result of a six months stay at the Graduate Aeronautical Laboratories of the California Institute of Technology. I was offered the possibility to join Caltech as a "Visitor in Aeronautics" during this period. This stay would not have been possible without the help of several persons and institutions. First of all I thank my advisor in The Netherlands, Prof. Tijdeman, for his continuing efforts to support me and other students. He made it possible to interrupt my PhD project at the University of Twente for a stay at Caltech. The generous support from the department of Applied Mechanics and the Faculty of Mechanical Engineering enabled a good quality of life in beautiful sunny (?, El Nino) Southern California. In this respect I also thank Prof. Huetink and Prof. Grootenboer.

The work at Caltech was both challenging and rewarding. I thank my colleagues at the Explosion Dynamics Group and my advisor, Prof. Shepherd, for creating a very stimulating and pleasant environment both inside and outside the lab. The work could not have been completed without the help of Raza, Mike and Eric in the Guggenheim sub-basement lab.

This research was sponsored by the Netherlands Organization for Scientific Research (NWO). Their support is gratefully acknowledged.

Pasadena, May 17, 1999

Marco Beltman

Chapter 1

Introduction

1.1 General introduction

At the Aeronautics department of the California Institute of Technology the behaviour of shock waves and detonations is studied. A detonation test tube facility and several shock tube facilities are available for laboratory experiments. During a shock or detonation test, the tube is exposed to high pressures. The detonation or shock wave propagates down the tube and therefore the tube is subjected to a moving pressure load. The problem has a strong dynamic nature. This report deals with the structural response of cylindrical shells to moving pressure loads. The results can be used for the analysis of tube systems, both in industrial and military applications.

1.1.1 Shock tube

Shock tubes are used to investigate shock wave propagation. A shock is created by the driver of the shock tube. The shock wave then travels down the tube at a nearly constant speed. A typical measured pressure history for a point in the tube is given in figure 1.1. The figure shows the measured pressure versus time for a thin aluminium tube in the GALCIT 6 inch shock tube facility. The character of the shock loading is a stepwise varying pressure, advancing at constant speed. Therefore the loading for a shock tube will be represented by a step profile in this report. The load is characterized by the pre-shock pressure p_1, the post-shock pressure p_2 and the velocity v (see figure 1.1)

1.1.2 Detonation tube

A detonation consists of a shock wave and a reaction zone that are tightly coupled. For prompt detonation, at one side of the detonation tube an explosion is initiated by a high explosive. The detonation then travels down the tube at a nearly constant speed: the Chapman-Jouguet velocity. The pressure history for this type of loading can be characterized by the initial pressure p_1, the peak

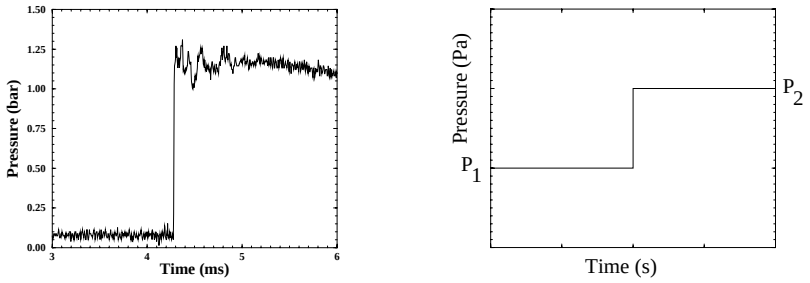

Figure 1.1: Pressure versus time for shock loading

pressure p_2, the final pressure p_∞ and the exponential decay factor T (see figure 1.2).

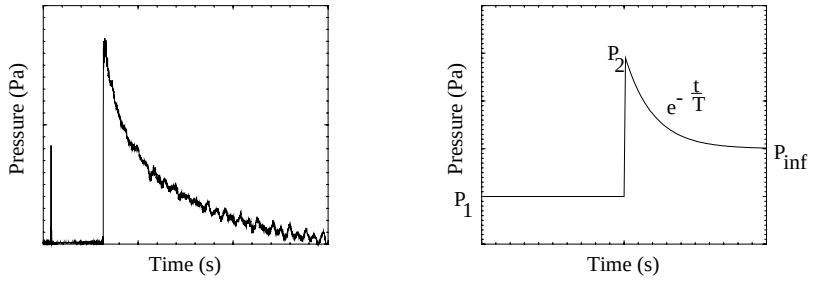

Figure 1.2: Pressure versus time for detonation loading

For the prompt detonation case the pressure loads are well defined. However, the case of deflagration to detonation (DDT) is more complex. In the deflagration to detonation case there intitially is no detonation but only a propagating flame. The flame compresses the unreacted gas ahead of the flame and a spontaneous explosion can occur in this unreacted gas. This can lead to extremely high pressures. However, for a properly operated detonation facility the chance of a DDT event is very low.

1.1.3 Structural response

In figure 1.3 the measured circumferential strain versus time for shock loading of a thin aluminium tube is depicted.

The measured strain shows a sharp peak when the shock passes. For the shock under consideration, the strain exceeds the equivalent static strain by a factor 3. This example indicates that a simple static model of the tube cross

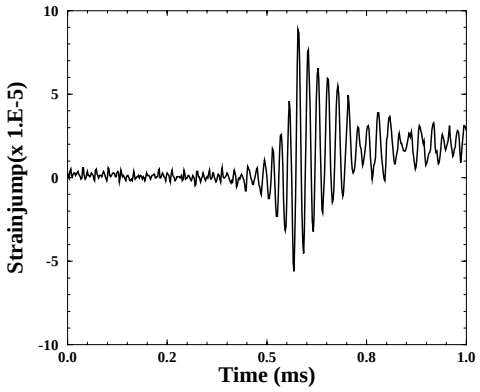

Figure 1.3: Strain history for shock loading

section is not sufficient to predict this large strain. One could calculate the maximum strains and stresses corresponding to the maximum load, but this would result in stresses and strains that are too low. The key question now is: what is the cause of the high strain? A somewhat more sophisticated model takes into account the step character of the loading. However, unfortunately the difference with the simple static cross-sectional model is small, even when the loading is located near a support.

It is now clear that the cause of the high strain is of a dynamic nature. The most simple dynamical model is the dynamical version of the cross-sectional model. This model describes the radial (breathing) motion of the cylinder cross-section. For shock loading, the maximum strain is twice the equivalent static strain. Although significantly higher strains are obtained with this model, it is clear that an essential mechanism is still missing.

Experiments on shock tubes and gun tubes revealed that the speed of propagation of the shock wave is an important parameter. The high strains in the experiments are due to flexural motion of the cylinder wall. Several models were developed to describe this phenomenon, some including for instance rotatory inertia and transverse shear deformation. The flexural models predict the existance of a so-called critical velocity. When the shock travels at the critical speed, the solution for the radial tube motion becomes unbounded. Evidently, damping, non-linearities and plastic deformation will be the controlling mechanisms in this case. Nevertheless, the flexural models are able to predict the high strains that were found in the experiments.

1.2 Formulation of the problem

The main aims of this study are:

- prediction of the structural reponse of a cylindrical tube to shock or detonation loading and comparison with experimental data
- development of design criteria and design methods for tubes that are subjected to shock or detonation loading

Special attention will be paid to the following subjects:

- end effects
  In most models the tube is assumed to be infinite in length. However, in practical situations one deals with short tube sections that are connected by flanges. This will have important implications for the structural response and the design of the tube.
- limits of predictability
  An important issue to keep in mind when developing models and design concepts, is the subject of "limited predictability". Due to variation in the input data, *e.g.* material properties or geometrical properties, there is a degree of uncertainty in the results.

1.3 Outline

This research is carried out in a number of steps. Accordingly, the report is divided into three parts. In part I, the general theory for the structural response of tubes to shock or detonation loading is presented. A number of analytical models is described. These models are not new. However, for the present study they were all rewritten into the same notation in order to put them into perspective. Simple analytical models were developed to describe the transient response of a finite length shell. Finally, in order to describe more complicated boundary conditions, a finite element model was developed.

In part II of this report an analysis is presented for the GALCIT 6 inch shock tube. Results from calculations and experiments are compared for a thin aluminium tube subject to shock loading. The shock tube problem is well defined and the important mechanisms and concepts can be analyzed for this setup.

Finally, an analysis of the detonation tube problem will be described in part III. The detonation tube is a thick walled tube that is constructed of relatively short segments, connected by flanges. Theory and experiments will be used to develop methods in the design process.

Chapter 2

Experimental setup

2.1 The GALCIT Detonation Tube

A drawing of the complete detonation tube is given in figure 2.1. The plumbing schematic is given in figure 2.2. The tube consists of three sections. Each section is about 2.4 m. long. The internal radius of the tube is 14 cm and the outer radius is 16.5 cm. The tube is made of stainless steel. The sections are connected by flanges.

Before each experiment, the tube is evacuated. After that the tube is filled to the desired pressure with the mixture of interest. The firing plug on the left of the tube is loaded with a thin wire. A high voltage capacitor is charged and then discharged over the wire. Just before the discharge a small amount of a sensitive driver mixture (1.5 kPa acetylene oxygen) is injected into the left end of the tube. The exploding wire will initiate a detonation of the driver mixture. The driver detonation on its turn will trigger a detonation in the testmixture. The injection of driver gas initiates a detonation, also for less sensitive mixtures. However, when for instance large amounts of diluents are used, the initiation can fail. In case of a misfire the glow plug can be used to burn the mixture. If the initiation is successfull, a detonation travels down the tube at a high velocity. Typical velocities range from 2000 m/s to 3000 m/s. A complete checklist for a run is given in appendix A.

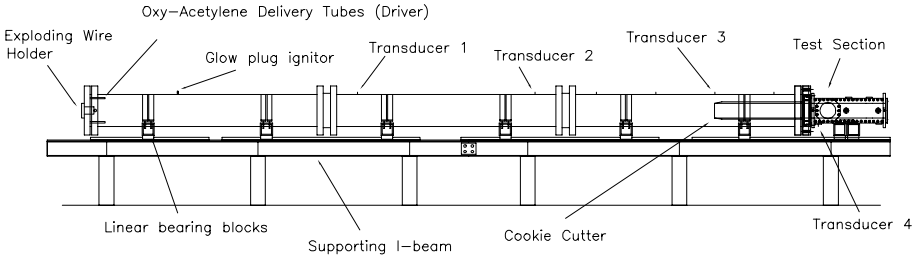

Figure 2.1: The GALCIT Detonation Tube facility

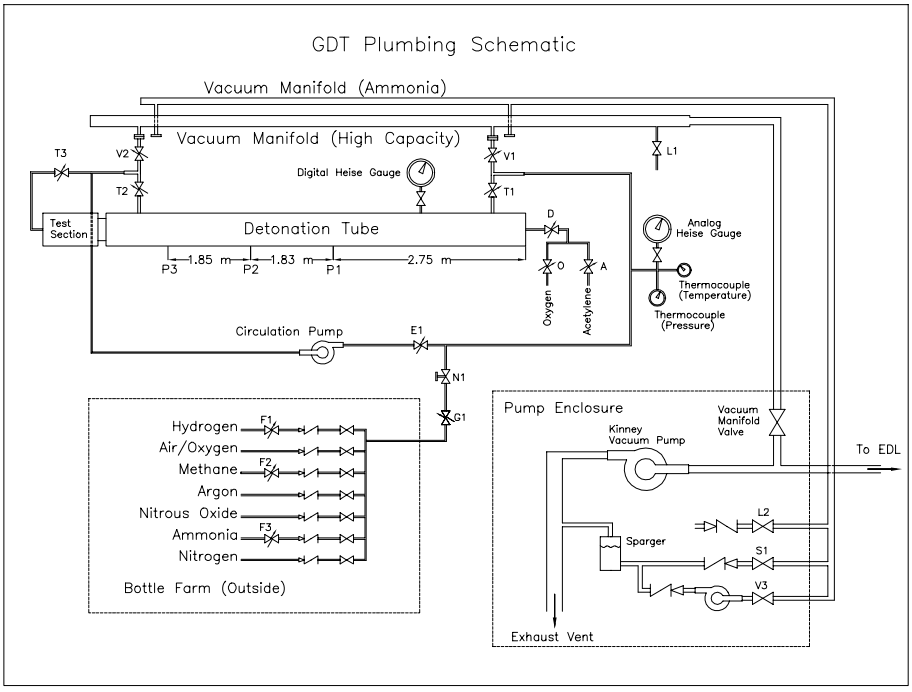

Figure 2.2: Plumbing schematic of GDT

2.2 Material and geometrical properties

The material and geometrical properties of a tube are given in table 2.1. The length is the effective length of one tube section. The sections are connected by flanges (see figure 2.3). The flanges, keys and bolts hold the two pieces of tube together. There is clearance between the inner radius of the flanges and the outer radius of the tube. The motion of the tube is restricted by the flanges that press on the keys and the T-piece between two tubes. The effective length of a tube is taken to be the length between the outer sides of two key grooves. In the finite element calculations, different boundary conditions will be imposed on the ends of the tube.

E	$193 \cdot 10^9\ N/m^2$
ρ	$8 \cdot 10^3\ kg/m^3$
ν	0.23
R_{in}	$0.1397\ m$
R_{out}	$0.1651\ m$
L	$2.38\ m$

Table 2.1: Material and geometrical properties

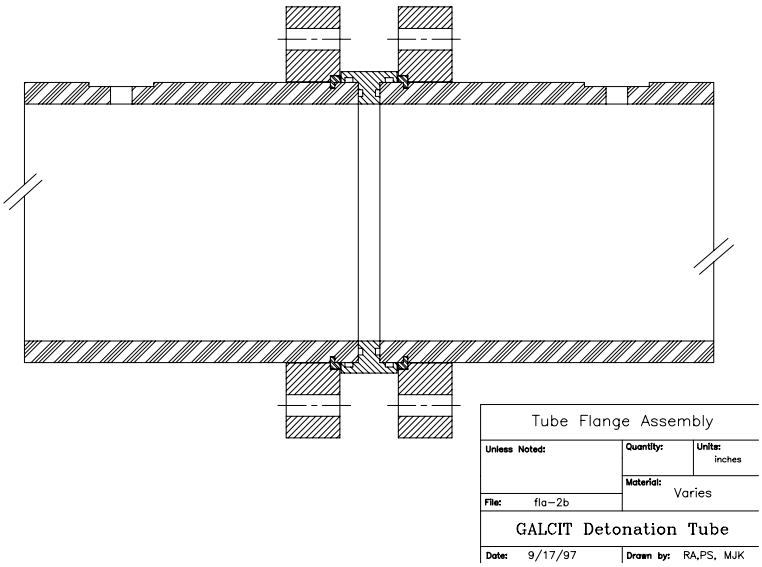

Figure 2.3: Tube connection

2.3 Strain measurements

For the present investigation, 18 strain gages are used. In a previous experiment, three strain gages were already used (gages #4, #6 and #8). The other 15 strain gages were mounted on the tube at several locations. The locations and the gage factors are given in table 2.2 and figure 2.4. Note that the distances x_I, x_{II} and x_{III} are measured from the key.

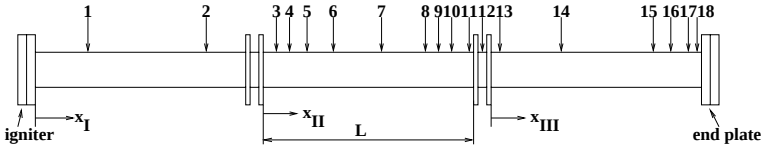

Figure 2.4: Strain gages

Gage	x (cm)	$\frac{x}{l}$	Gage factor
1	$x_I = 118.1$	0.496	2.11
2	$x_I = 195.1$	0.820	2.09
3	$x_{II} = 24.76$	0.104	2.09
4	$x_{II} = 43.26$	0.182	2.11
5	$x_{II} = 78.96$	0.332	2.09
6	$x_{II} = 118.1$	0.496	2.11
7	$x_{II} = 156.7$	0.659	2.09
8	$x_{II} = 195.1$	0.820	2.11
9	$x_{II} = 208.5$	0.876	2.11
10	$x_{II} = 219.5$	0.923	2.11
11	$x_{II} = 227.3$	0.955	2.09
12	middle		2.09
13	$x_{III} = 9.36$	0.039	2.09
14	$x_{III} = 118.1$	0.496	2.09
15	$x_{III} = 195.1$	0.820	2.09
16	$x_{III} = 208.5$	0.876	2.11
17	$x_{III} = 216.0$	0.908	2.11
18	$x_{III} = 224.3$	0.943	2.11

Table 2.2: Strain gage positions for strain measurements

The strain signals are used as input for balanced Wheatstone bridge circuits. The output voltages are then amplified and led to the data acquisition system. A more detailed description of the setup is given in appendix B.

2.4 Pressure measurements

The pressure is measured at three points. The first and the second transducer are mounted on the second tube section (see figure 2.1). The third transducer is mounted on the third tube section. The pressure signals are used to determine the velocity of the detonation. The amplitude of the pressure is not very accurate. Therefore the results will be normalized with respect to a calculated pressure: the Chapman-Jouguet pressure of the detonation.

2.5 Flow visualisation

For the present investigations, the endplate is mounted on the end of the tube. The detonation will reflect off the endplate. However, in figure 2.1 the test section and the cookie cutter are attached to the end of the tube. The cookie cutter sticks back into the tube and "cuts out" a piece of the detonation that then travels down the cookie cutter. The cross section of the cookie cutter is rectangular and at the end the test section is attached. The test section is used for different visualisation experiments. It has windows on both sides. A ruby laser and an optical system are used to visualize the detonation. This setup was used for instance to investigate the diffraction of a detonation over a wedge and the diffraction of a detonation from a small tube.

2.6 Test mixture

The critical velocity of the tube is approximately: $v_{cr} = 1500\ m/s$. A stochiometric Hydrogen Oxygen mixture with variable amount of Argon as diluent was used:

$$2H_2 + O_2 + \#Ar \tag{2.1}$$

The amount of Ar can be used to control the velocity of the detonation. However, by increasing the amount of diluent also the cell size increases. The pressure of the mixture also affects the velocity and the cell size. In order to set up a series of measurements, the behaviour of the mixture was investigated for a number of conditions. In figure 2.5 the (Chapman-Jougeut) velocity of the detonation is plotted as a function of the amount of diluent. The velocity was calculated with the STANJAN program. The cell size data was taken from the detonation database. Data was taken from [1, 2, 3, 4, 5, 6, 7].

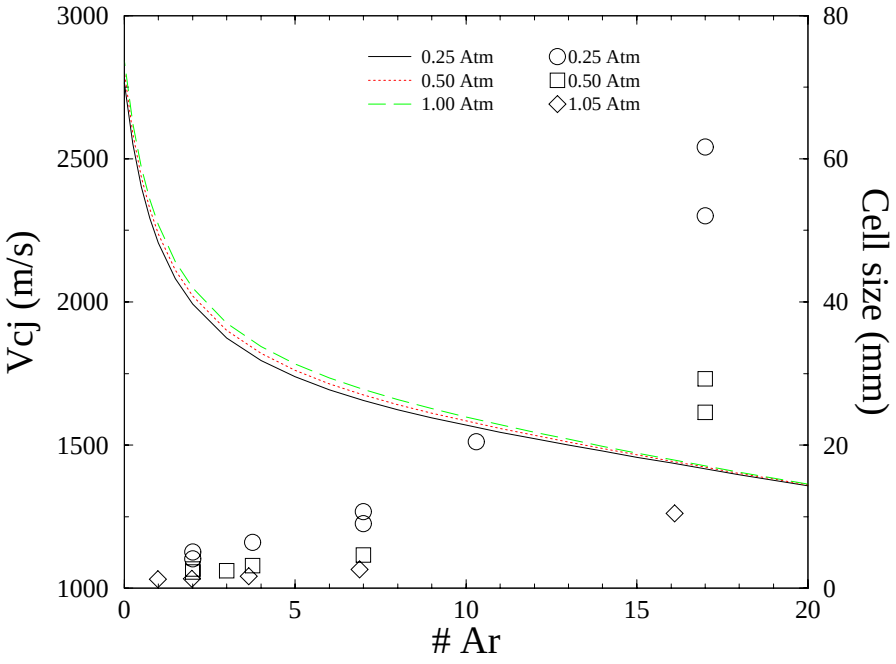

Figure 2.5: Behaviour of test mixture

The following observations can be made:

- the velocity decreases with increasing amount of diluent
- the velocity is not very sensitive to pressure variation
- the cell size increases with increasing amount of diluent
- the cell size is sensitive for pressure variation: it is inversly proportional to the pressure

In the ideal case, the experimental conditions are chosen such, that only one parameter is changed at a time. Since the detonation process depends on a number of parameters, a careful choice has to be made. Based on the previous considerations, the following test conditions were chosen:

- linearity of response
  The linearity of the response is investigated by varying the pressure. If the amount of diluent is kept low, the velocity is not affected very much. The cell size then also remains sufficiently small compared to the structural wavelength. For the conditions of interest the structural wavelength varies between 0.2 and 0.5 m.

- velocity
  The influence of the velocity is investigated by varying the amount of diluent. The pressure is chosen high, 100kPa, so that the cell size remains sufficiently small. Only for the high velocity shots a lower pressure, 50 kPa, is used to stay within the design limits of the tube what maximum pressure is concerned. At these high speeds the amount of diluent is low and the cell size is small.

- cell size
  The influence of the cell size is investigated by varying the pressure at high concentrations of diluent. The velocity is not affected very much, whereas the cell size increases dramatically. The largest cell size in the experiments is of the order of magnitude of the structural wavelength and the tube diameter. Since both the pressure and the cell size vary, the cell size influence can be extracted only if the process proves to behave linearly.

2.7 Test matrix

2.7.1 Reference/reproducibility shots

After each series of shots a reference shot at 1400 m/s is carried out. The data of these shots were used to investigate the reproducibility of the experiments. Extra shots were also carried out at velocities of 1520 m/s and 1460 m/s. The strain gages and the test conditions are given in figure 2.6 and table 2.3.

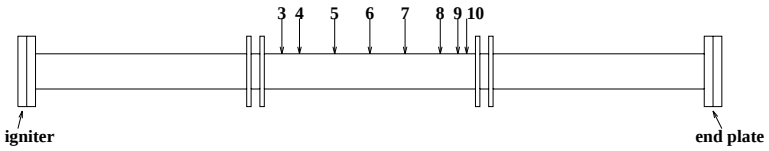

Figure 2.6: Gages for reference/reproducibility shots

Nr	*Shot*	v_{CJ} (m/s)	$\frac{v}{v_{cr}}$	p (kPa)	p_{for} (MPa)	p_{ref} (MPa)	$\#Ar$	p_{H2} (kPa)	p_{O2} (kPa)	p_{Ar} (kPa)
20	621	1400.1	0.933	100	1.20	2.77	18.25	9.27	4.64	84.59
38	641	1400.1	0.933	100	1.20	2.77	18.25	9.27	4.64	84.59
39	642	1520.5	1.014	100	1.43	3.36	13.00	12.31	6.16	80.03
40	643	1460.1	0.973	100	1.31	3.06	15.55	10.62	5.31	82.57
49	652	1400.1	0.933	100	1.20	2.77	18.25	9.27	4.64	84.59

Table 2.3: Reference/reproducibility shots: test conditions

2.7.2 Development of profile

The finite element calculations for the shock tube (see part II) indicate that the deflection profile has to develop. For a tube of finite length, the maximum amplification factor will always remain finite. This indicates that the infinite amplitude, encountered in the simple analytical thin shell model, is only due to the assumption of an infinite tube. The development of the profile can be calculated with the transient analytical and finite element models.

A first comparison with data from the GALCIT 6 inch shock tube showed results that seemed to be not in accordance with expectations. However, only three strain gages were used in that experiment. Furthermore, the ratio between tube length and wave length differs between the shock tube and the detonation tube. For the shock tube, the ratio between length and wavelength is about 50. For the detonation tube this ratio is about 10. Preliminary strain measurements on the detonation tube indicate an increase of maximum amplification with distance. This phenomenon was studied now in more detail. The second

(=middle) tube section was instrumented with a large amount of strain gages, see figure 2.7. The run conditions are given in table 2.4.

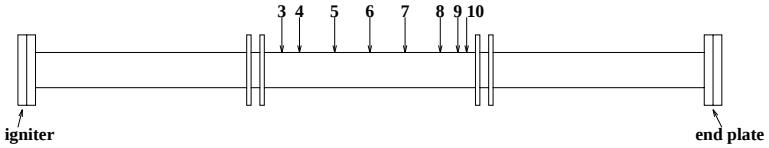

Figure 2.7: Gages to monitor development of profile

Nr	*Shot*	v_{CJ} (m/s)	$\frac{v}{v_{cr}}$	p (kPa)	p_{for} (MPa)	p_{ref} (MPa)	$\#Ar$	p_{H2} (kPa)	p_{O2} (kPa)	p_{Ar} (kPa)
1	602	1300.2	0.867	100	1.03	2.35	23.25	7.50	3.75	87.24
2	603	1325.6	0.884	100	1.07	2.45	21.90	7.91	3.96	86.63
3	604	1350.2	0.900	100	1.12	2.55	20.65	8.33	4.16	86.00
4	605	1375.7	0.917	100	1.16	2.66	19.40	8.79	4.40	85.31
5	606	1400.1	0.933	100	1.20	2.77	18.25	9.27	4.64	84.59
6	607	1420.7	0.947	100	1.24	2.87	17.30	9.70	4.85	83.94
7	608	1440.8	0.961	100	1.28	2.96	16.40	10.15	5.08	83.27
8	609	1460.1	0.973	100	1.31	3.06	15.55	10.62	5.31	82.57
9	610	1478.8	0.986	100	1.35	3.16	14.70	11.13	5.56	81.81
10	611	1498.7	0.999	100	1.39	3.25	13.90	11.66	5.83	81.01
11	612	1520.5	1.014	100	1.43	3.36	13.00	12.31	6.16	80.03
12	613	1539.0	1.026	100	1.46	3.45	12.25	12.92	6.46	79.12
13	614	1559.5	1.040	100	1.50	3.55	11.45	13.63	6.82	78.05
14	615	1579.2	1.053	100	1.53	3.65	10.70	14.38	7.19	76.93
15	617	1599.7	1.066	100	1.57	3.75	9.95	15.21	7.61	75.68
16	616	1624.3	1.083	100	1.61	3.84	9.10	16.28	8.14	74.08
17	618	1649.1	1.099	100	1.64	3.94	8.30	17.43	8.72	72.35
18	619	1675.9	1.117	100	1.67	4.04	7.50	18.76	9.38	70.36
19	620	1699.7	1.133	100	1.70	4.11	6.85	20.00	10.00	68.50

Table 2.4: Development of profile: test conditions

2.7.3 Flanges and end effects

A correct description of the behaviour of the flanges is needed for a good numerical model. In the "ideal" case, the flanges would prevent radial motion and act as local clamping conditions. This would mean that the tube sections are decoupled as far as flexural motion is concerned. In every section, the deformation pattern has to develop again. In a model, one would then only have to model one section instead of the whole tube.

However, the clamping assumption is an ideal situation. In reality there is some clearance between (parts of) the flanges and the tube. A typical maximum strain in a detonation experiment is of the order of magnitude of 10^{-4}. For the tube of interest, this corresponds to a radial displacement of only 0.015 mm. This means that a clearance larger than 0.015 mm would not prevent radial motion. The flange however does add inertia to the detonation tube. The theoretical predictability of the behaviour of the connection is thought to be rather poor. Therefore experiments were carried out to monitor the flanges.

Because the flanges are discontinuities as wave propagation is concerned, part of the wave will reflect at the flanges. The interference between forward travelling waves and reflected waves can lead to high strains and stresses. At the end of the tube the reflected shock and the reflected waves were expected to give the highest strains. Therefore strain gages were mounted near the end and the flanges (see figure 2.7). The test matrix is given in table 2.5.

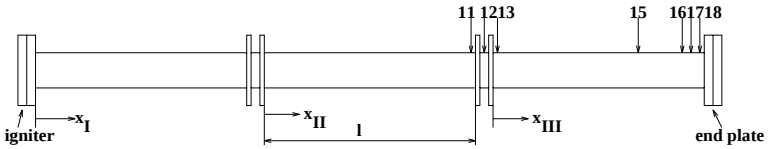

Figure 2.8: Gages to monitor flanges and end effects

Nr	*Shot*	v_{CJ} (m/s)	$\frac{v}{v_{cr}}$	p (kPa)	p_{for} (MPa)	p_{ref} (MPa)	$\#Ar$	p_{H2} (kPa)	p_{O2} (kPa)	p_{Ar} (kPa)
21	622	1350.2	0.900	100	1.12	2.55	20.65	8.33	4.16	86.00
22	623	1375.7	0.917	100	1.16	2.66	19.40	8.79	4.40	85.31
23	624	1400.1	0.933	100	1.20	2.77	18.25	9.27	4.64	84.59
24	625	1420.7	0.947	100	1.24	2.87	17.30	9.70	4.85	83.94
25	626	1440.8	0.961	100	1.28	2.96	16.40	10.15	5.08	83.27
26	627	1460.1	0.973	100	1.31	3.06	15.55	10.62	5.31	82.57
27	628	1478.8	0.986	100	1.35	3.16	14.70	11.13	5.56	81.81
28	629	1498.7	0.999	100	1.39	3.25	13.90	11.66	5.83	81.01
29	630	1520.5	1.014	100	1.43	3.36	13.00	12.31	6.16	80.03
30	631	1539.0	1.026	100	1.46	3.45	12.25	12.92	6.46	79.12
31	632	1559.5	1.040	100	1.50	3.55	11.45	13.63	6.82	78.05
32	633	1579.2	1.053	100	1.53	3.65	10.70	14.38	7.19	76.93
33	634	1599.7	1.066	100	1.57	3.75	9.95	15.21	7.61	75.68
34	635	1624.3	1.083	100	1.61	3.84	9.10	16.28	8.14	74.08
35	636	1649.1	1.099	100	1.64	3.94	8.30	17.43	8.72	72.35
36	637	1675.9	1.117	100	1.67	4.04	7.50	18.76	9.38	70.36
37	638	1699.7	1.133	100	1.70	4.11	6.85	20.00	10.00	68.50

Table 2.5: Flanges and end effects: test conditions

2.7.4 Linearity and comparison of sections

The calculations are all based on linear elastic theory. In order to investigate the linearity, experiments are carried out with different pressure levels for the same detonation speed. By varying the initial pressure at low diluent concentrations the pressure level changes, while the speed remains nearly constant (see section 2.6). The setup is also used to compare the behaviour of the three tube sections. Two strain gages were mounted on "identical" positions on different tube sections for this purpose. If the tube can be considered as a series of independent short sections, the strains would have to be identical for two "identical" positions [1]. There are some aspects that have to be kept in mind:

- the pressure profile has to develop
- the three sections are not completely identical
- reflected waves interfere with forward travelling waves (endplate)

The positions of the strain gages are given in figure 2.9. The run conditions are given in table 2.6.

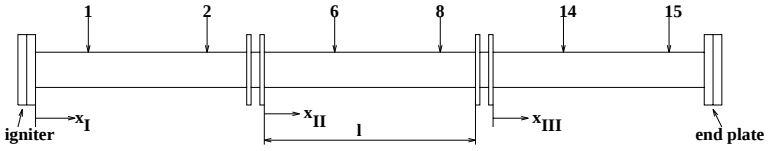

Figure 2.9: Gages to monitor linearity and compare sections

Nr	*Shot*	v_{CJ} (m/s)	$\frac{v}{v_{cr}}$	p (kPa)	p_{for} (MPa)	p_{ref} (MPa)	$\#Ar$	p_{H2} (kPa)	p_{O2} (kPa)	p_{Ar} (kPa)
41	644	1799.5	1.120	100	1.79	4.35	4.70	25.58	12.79	60.12
42	645	1799.3	1.120	75	1.33	3.25	4.54	19.50	9.75	44.26
43	646	1799.6	1.120	50	0.88	2.15	4.31	13.27	6.63	28.60
44	647	1799.5	1.120	25	0.43	1.06	3.94	6.77	3.39	13.34
45	648	1999.0	1.333	100	1.87	4.57	2.35	36.82	18.41	43.27
46	649	1999.5	1.333	75	1.39	3.40	2.26	27.95	13.97	31.58
47	650	1999.9	1.333	50	0.91	2.24	2.14	18.87	9.44	20.19
48	651	2000.0	1.333	25	0.45	1.09	1.95	9.49	4.75	9.26

Table 2.6: Linearity and compare sections: test conditions

[1] discarding reflections at the end

2.7.5 Cell size

A number of shots was carried out to investigate the influence of the cell size on the structural response. At large diluent concentrations and low pressures, the cell size is comparable to the structural wavelength. This might result in a very effective excitation of these structural waves. Therefore shots are carried out with increasing cell sizes. The strain gages that are used are given in figure 2.10. The run conditions are given in table 2.7. The estimated cell size λ is given in this table.

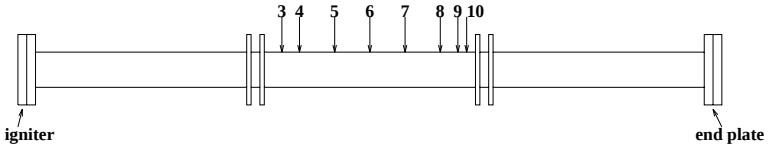

Figure 2.10: Gages for cell size shots

Nr	*Shot*	v_{CJ} (m/s)	$\frac{v}{v_{cr}}$	p (kPa)	p_{for} (MPa)	p_{ref} (MPa)	$\#Ar$	p_{H2} (kPa)	p_{O2} (kPa)	p_{Ar} (kPa)	λ (mm)
50	653	1400.1	0.933	100	1.20	2.77	18.25	9.27	4.64	84.59	15
51	654	1396.4	0.931	50	0.60	1.38	18.25	4.56	2.28	41.65	30
52	655	1392.1	0.928	25	0.30	0.69	18.25	2.21	1.11	20.18	60
53	656	1269.3	0.846	100	0.99	2.24	25.00	7.04	3.52	87.95	30
54	657	1268.6	0.846	50	0.49	1.12	25.00	3.46	1.73	43.30	60
55	658	1267.8	0.845	25	0.25	0.56	25.00	1.68	0.84	20.98	120
56	659	1267.4	0.845	20	0.20	0.45	25.00	1.32	0.66	16.52	150
57	660	1394.3	0.929	35	0.42	0.97	18.25	3.15	1.58	28.77	45
58	661	1392.1	0.928	25	0.30	0.69	18.25	2.21	1.11	20.18	60
59	662	1390.5	0.927	20	0.24	0.55	18.25	1.74	0.87	15.89	70
60	663	1398.6	0.932	75	0.90	2.07	18.25	6.92	3.46	63.12	23
61	664	1269.0	0.846	75	0.74	1.68	25.00	5.25	2.63	65.63	45
62	665	1268.2	0.845	35	0.35	0.78	25.00	2.39	1.20	29.91	95
63	666	1267.8	0.845	25	0.25	0.56	25.00	1.68	0.84	20.98	120
64	667	1267.4	0.845	20	0.20	0.45	25.00	1.32	0.66	16.52	150

Table 2.7: Cell size shots: test conditions

2.7.6 High velocity shots

The critical velocity of the detonation tube is about 1500 m/s. In the experiments described in the previous sections the velocity was varied around this value. These speeds however are relatively low: in most cases the detonation speed is 2000 m/s to 3000 m/s. In order to investigate the behaviour of the

tube for the higher velocities, a number of experiments was carried out with low diluent concentrations. The reflected wave pressure increases with decreasing amount of diluent. In order to stay within the design limits of the tube, the experiments were carried out at a pressure of 50 kPa. At low diluent concentrations the cell size remains very small compared to the wave length. The strain gages are given in figure 2.11. The run conditions are given in table 2.8.

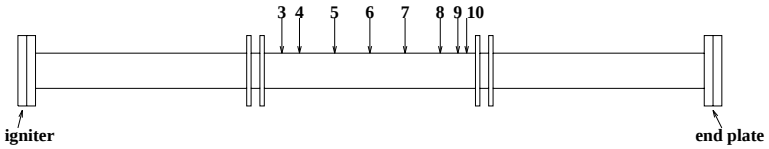

Figure 2.11: Gages for high velocity shots

Nr	*Shot*	v_{CJ} (m/s)	$\frac{v}{v_{cr}}$	p (kPa)	p_{for} (MPa)	p_{ref} (MPa)	$\#Ar$	p_{H2} (kPa)	p_{O2} (kPa)	p_{Ar} (kPa)
65	668	1800.2	1.200	50	0.88	2.15	4.30	13.29	6.64	28.57
66	669	1899.7	1.266	50	0.90	2.21	3.00	16.17	8.08	24.25
67	670	1999.9	1.333	50	0.91	2.24	2.14	18.87	9.44	20.19
68	671	2099.9	1.400	50	0.92	2.26	1.55	21.32	10.66	16.52
69	672	2199.3	1.466	50	0.92	2.27	1.13	23.49	11.74	13.27
70	673	2301.2	1.534	50	0.92	2.27	0.81	25.46	12.73	10.31
71	674	2401.3	1.601	50	0.93	2.27	0.57	27.17	13.58	7.74
72	675	2501.9	1.668	50	0.92	2.27	0.38	28.70	14.35	5.45
73	676	2600.8	1.734	50	0.92	2.27	0.23	30.03	15.02	3.45
74	677	2705.7	1.804	50	0.92	2.27	0.10	31.29	15.65	1.56
75	678	2803.0	1.869	50	0.92	2.27	0.00	32.33	16.17	0.00

Table 2.8: High velocity shots: test conditions

Chapter 3

Finite element model

The finite element calculations were carried out with the package Ideas. A transient linear elastic calculation was carried out to calculate the structural response to a moving pressure load. For the tube of interest, 500 elements were used in the axial direction and 5 in the radial direction. For the strain signals of interest, with a speed of approximately 2000 m/s and a frequency of 6 kHz, this means a resolution of about 70 elements per wavelength. The loading of the shell is highly transient. In each node, a force was prescribed as a function of time. The force history for each point depends on its axial location, the speed of the detonation, the amplitude of the detonation, the final pressure and the exponential decay rate T. In the calculations, a value of $4.34 \cdot 10^{-4}$ was used for T, according to measurements on the second tube sections. The exponential decay was approximated by 20 linear segments. The values of the initial pressure, the final pressure and the atmospheric pressure were set to zero in the amplification calculations. The response was calculated for the second tube section, up to the time that the reflected wave would enter the tube again the tube. For the time integration, 1000 intervals were used. For the problem of interest this means approximately 45 steps per cycle. The response was calculated with a normal mode superposition technique. The modes of vibration of the shell were calculated first. These eigenmodes were then used as a basis to calculate the transient shell response.

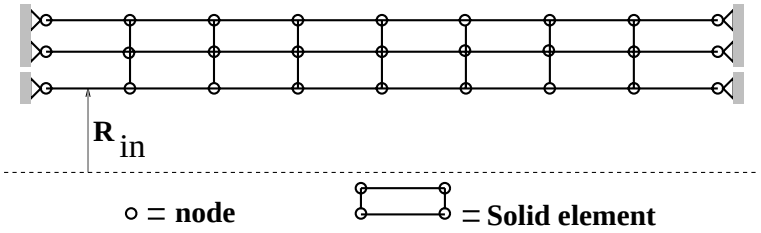

Figure 3.1: Finite element mesh clamped tube

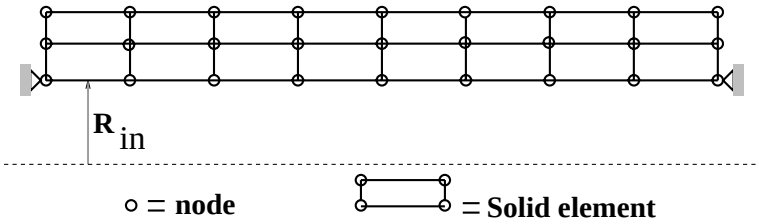

Figure 3.2: Finite element mesh simply supported tube

Chapter 4

Results and discussion

4.1 Reference/reproducibility shots

The results for the reference/reproduccbility shots are given in figure 4.2. The amplification factor is given as a function of velocity for the strain gages on the second tube section. For convenience, the positions of the strain gages are given again in figure 4.1.

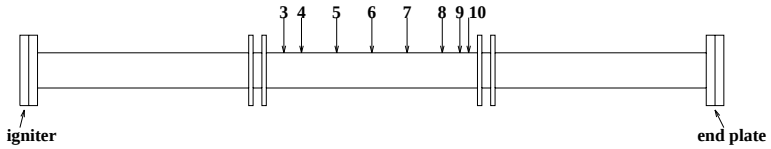

Figure 4.1: Gages for high velocity shots

The amplification factor is calculated by dividing the maximum strain by the equivalent static strain. The equivalent static strain is obtained from the Lame formula, with the Chapman-Jouguet pressure as the excitation. Note that the experimental results are therefore scaled by a calculated value and not by a measured pressure. The measured pressure level is not very reliable.

The results indicate that the shots are very reproducible for the gages 3,5,7,9 and 10. The maximum difference in amplification for these gages between the different shots is less than 4%. The reproducibility for the gages 4,6 and 8 is less good. These were the strain gages that were already used in a previous experiment. Due to the large speading, the results have to be interpreted with care for these gages.

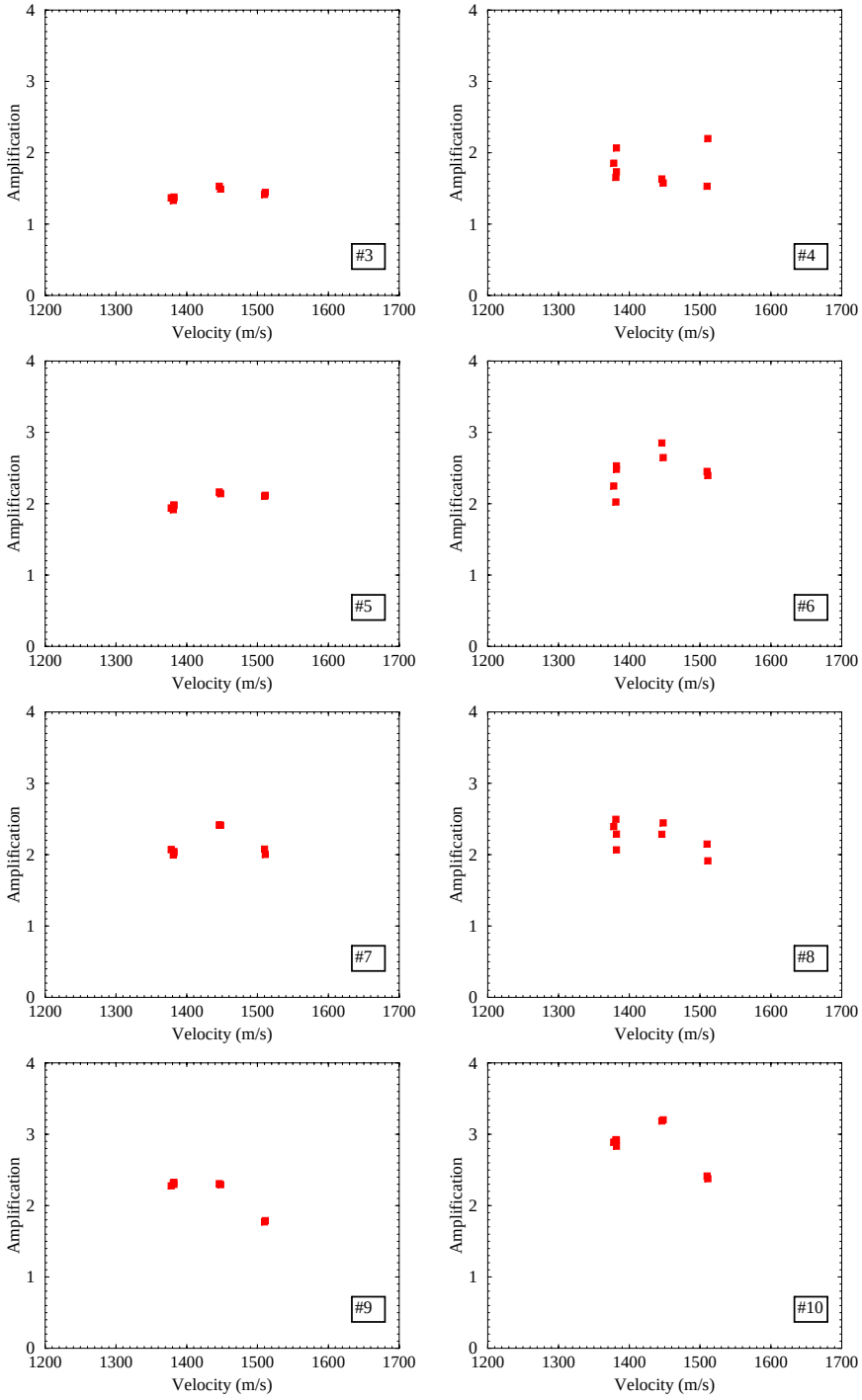

Figure 4.2: Experimental results reference/reproducibility shots

4.2 Development of profile

The strain gages for this measurements are given in figure 4.3.

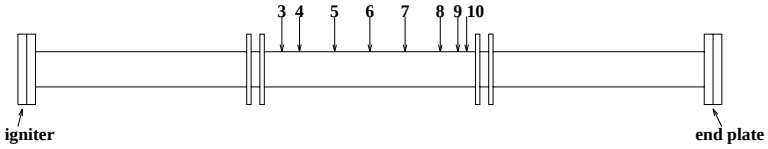

Figure 4.3: Gages to monitor development of profile

A typical strain history for a subcritical velocity is given in the figures 4.5 and 4.6 [1]. The corresponding pressure hisories are given in figure 4.4. The strain signals resemble the signals as predicted by simple analytical models. There is a precursor wave, the frequency of which is about the same as the frequency of the bulk signal. There is a peak when the detonation passes. The decay of the signal is relatively strong. Due to the fact that the waves are decaying, relection and interference is only clear for strain gage 10. This strain gage is mounted near the end of the second section and the reflection and interference causes high strains.

A typical strain history for a speed around the critical velocity is given in the figures 4.8 and 4.9 [2]. The corresponding pressure histories are given in figure 4.7. In this case the amplification is larger. It is clear from the strain signals that the the process is transient: time is required to build up the deflection profile. The maximum amplitude increases with distance. The precursor wave is relatively strong and the interference causes high strains for gage 10.

A typical strain history for a supercritical velocity is given in the figures 4.11 and 4.12. The corresponding pressure hisories are given in figure 4.10. The amplitude of the precursor wave has decreased. The frequency of the precursor signal is higher than the frequency of the bulk signal, as predicted by theory. The wave now start propagating and the decay of the signal after the detonation has passed is not very strong. The maximum amplitude is almost constant as a function of distance. Only for strain gage 10 the reflection and interference causes higher strains.

The amplification factor as a function of the velocity is given in figure 4.13. The experimental results are compared with finite element results for a clamped tube and a simply supported tube. The results clearly indicate the importance of the critical velocity concept.

[1] The large spike that is present in all strain signals just after $t = 0$ comes from the discharge of the capacitor

[2] The strain history for gage 6 shows a somewhat strange behaviour just after the detonation has passed. This behaviour was only observed in some runs for the gages 6,8 and 10. The reproducibility of these gages was low. These are the gages that were already used in previous experiments

The experimental results indicate that the critical velocity for the tube is about 1450 m/s. This is somewhat lower than the value precited by the finite element model, which is about 1500 m/s. The finite element calculations were carried out with material data that was taken from tables. There is a degree of uncertainty in these and other parameters. Regarding the uncertainty in the input parameters the results compare reasonably well with the experimental results. The model for the clamped tube is able to predict the amplification caused by the reflection and interference of waves at the flanges.

An interesting point is the amplification curve for gage 3. The finite element results for the this strain gage show a somewhat strange behaviour around the critical velocity. There are two broad peaks in the curve. By analyzing the strain history, these peak could be attributed to the reflection of waves. In the finite element model there is no damping. Any wave that starts propagating will therefore reflect and travel back to the first end of the section. The reflection and intereference at that end is the cause of the amplification bumps. In the experiments this behaviour was not observed. Due to the damping in the tube and at the joints the amplitude of the wave decays.

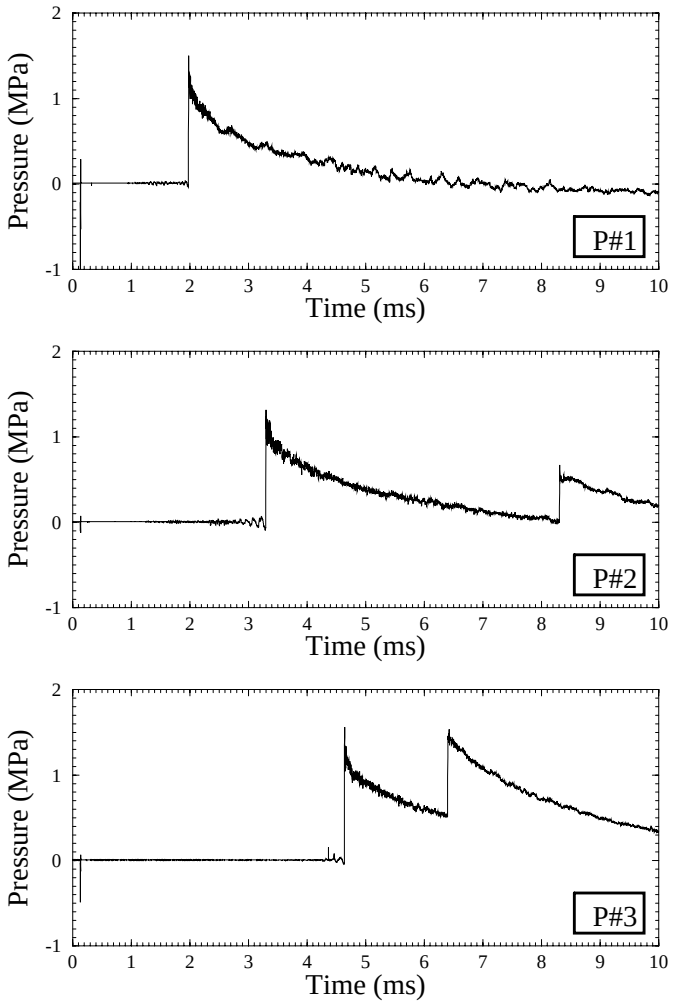

Figure 4.4: Pressure signals for run 606: 1400.1 m/s

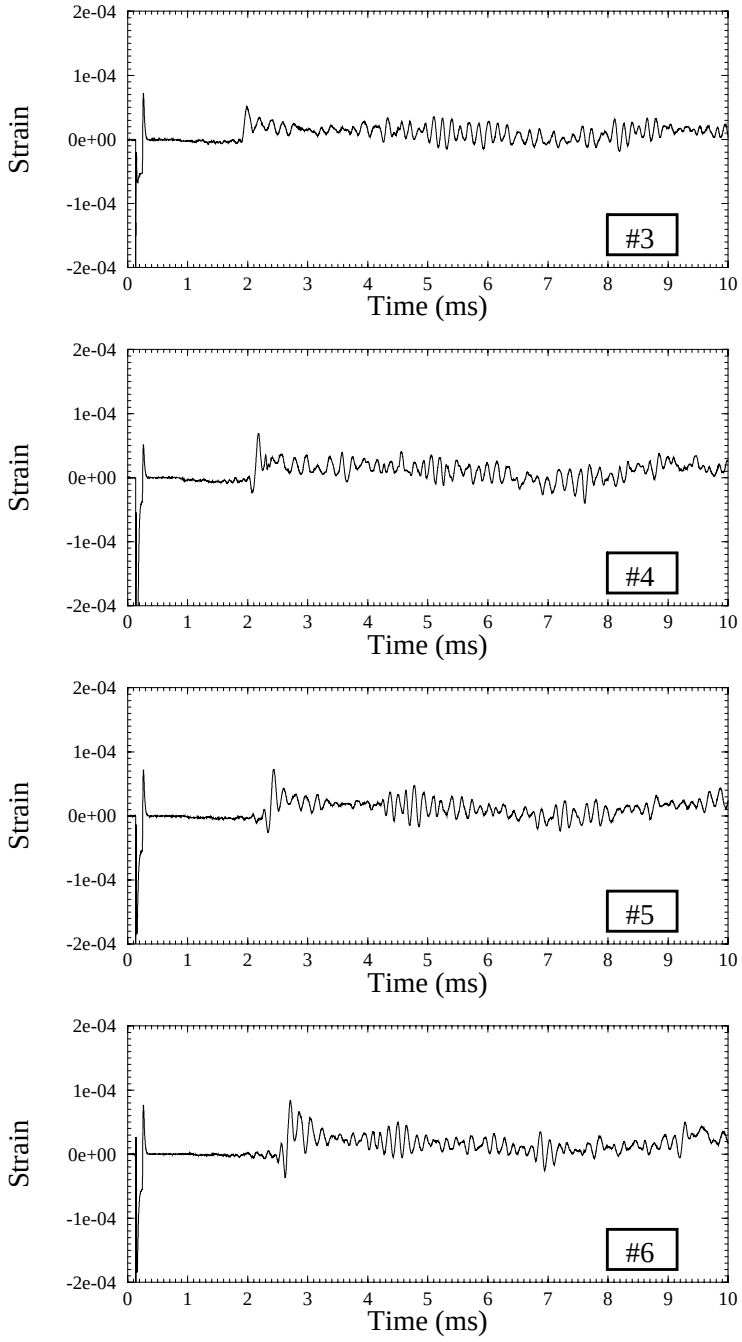

Figure 4.5: Strain signals for run 606: 1400.1 m/s

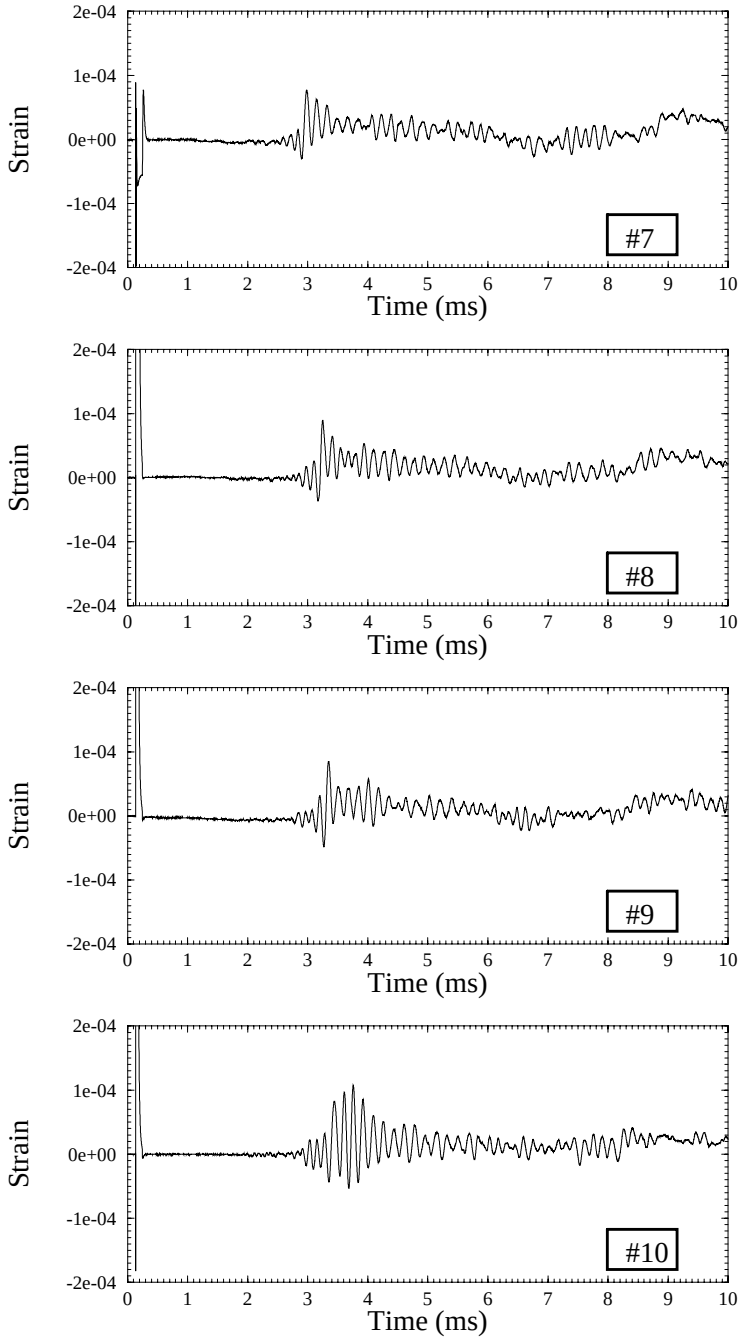

Figure 4.6: Strain signals for run 606: 1400.1 m/s

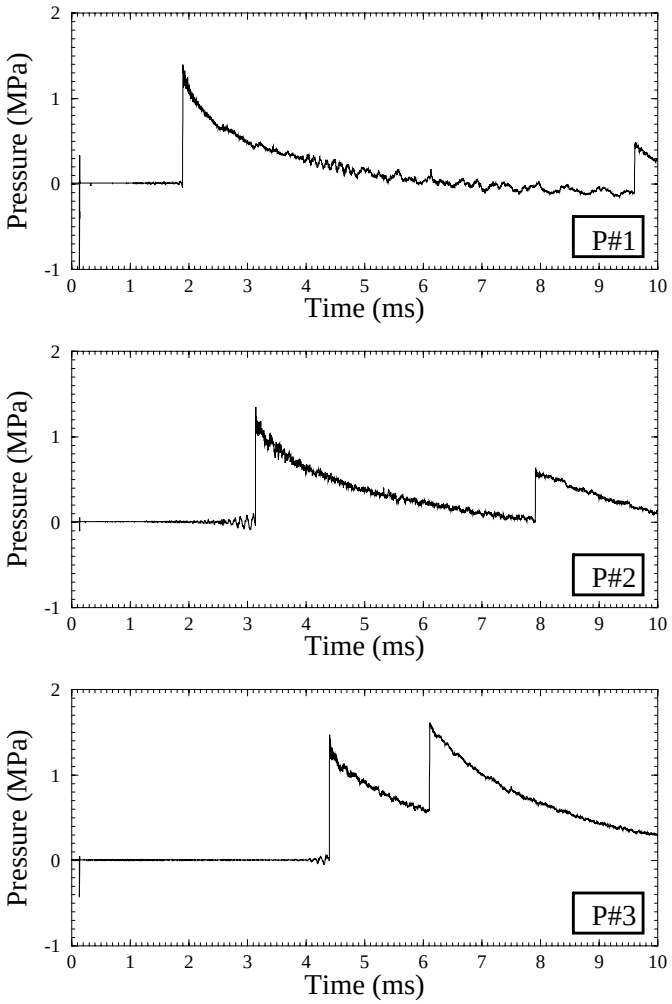

Figure 4.7: Pressure signals for run 610: 1478.8 m/s

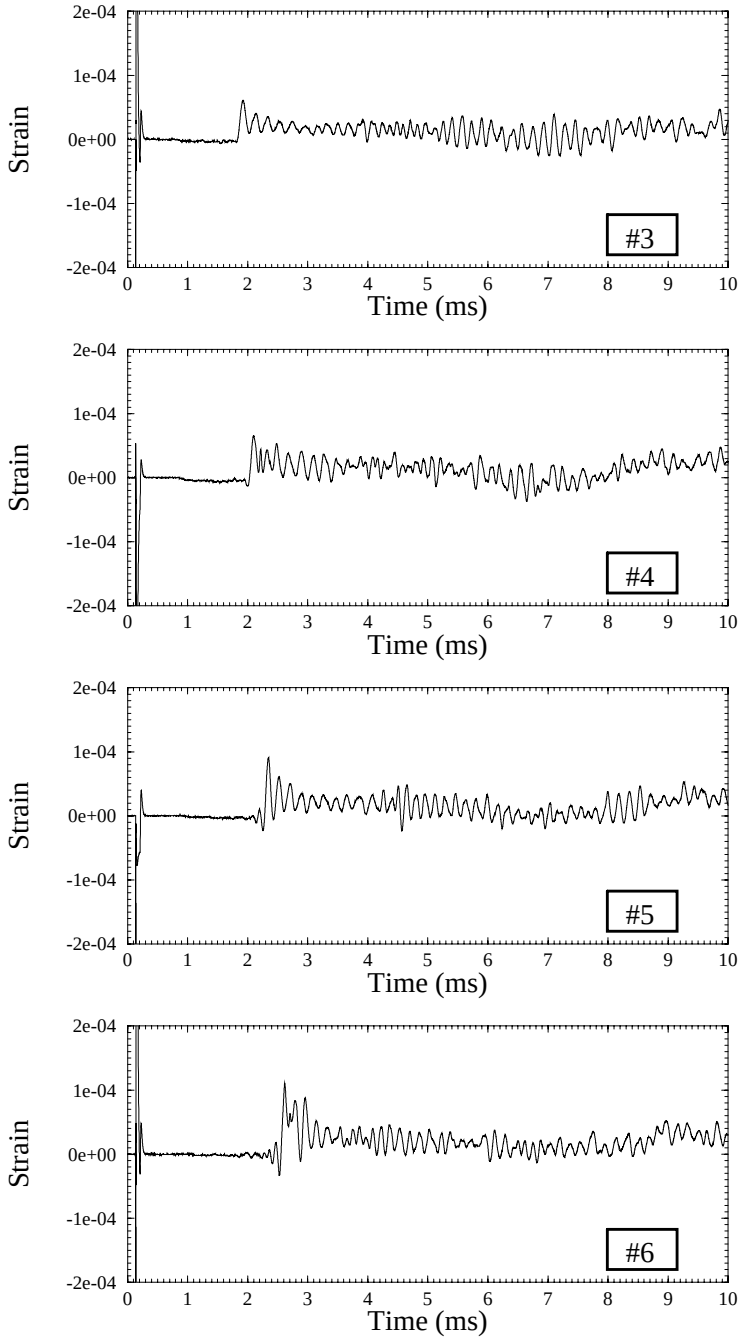

Figure 4.8: Strain signals for run 610: 1478.8 m/s

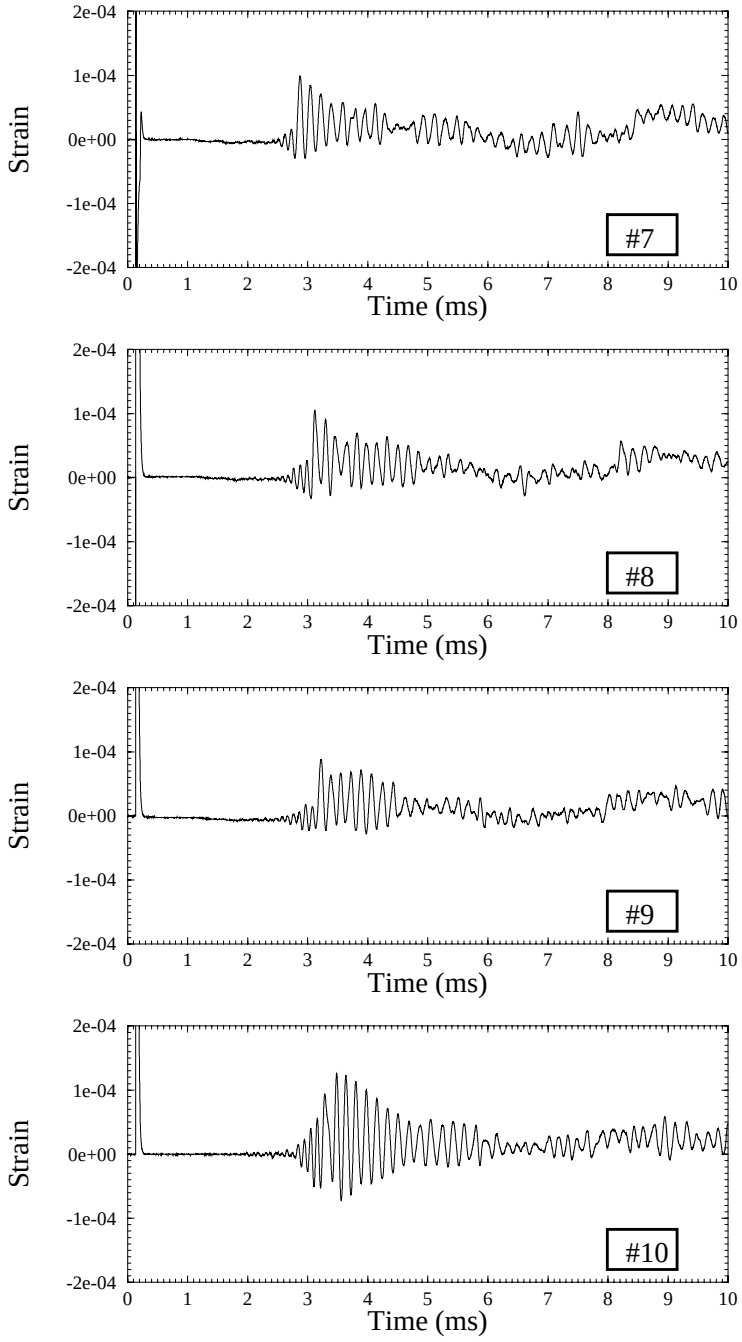

Figure 4.9: Strain signals for run 610: 1478.8 m/s

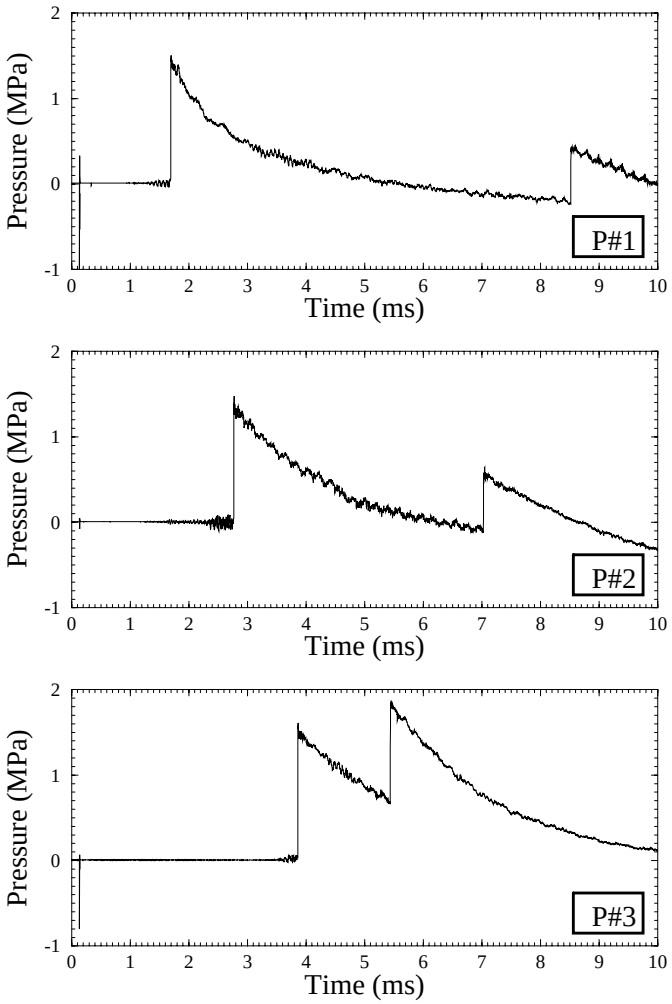

Figure 4.10: Pressure signals for run 620: 1699.7 m/s

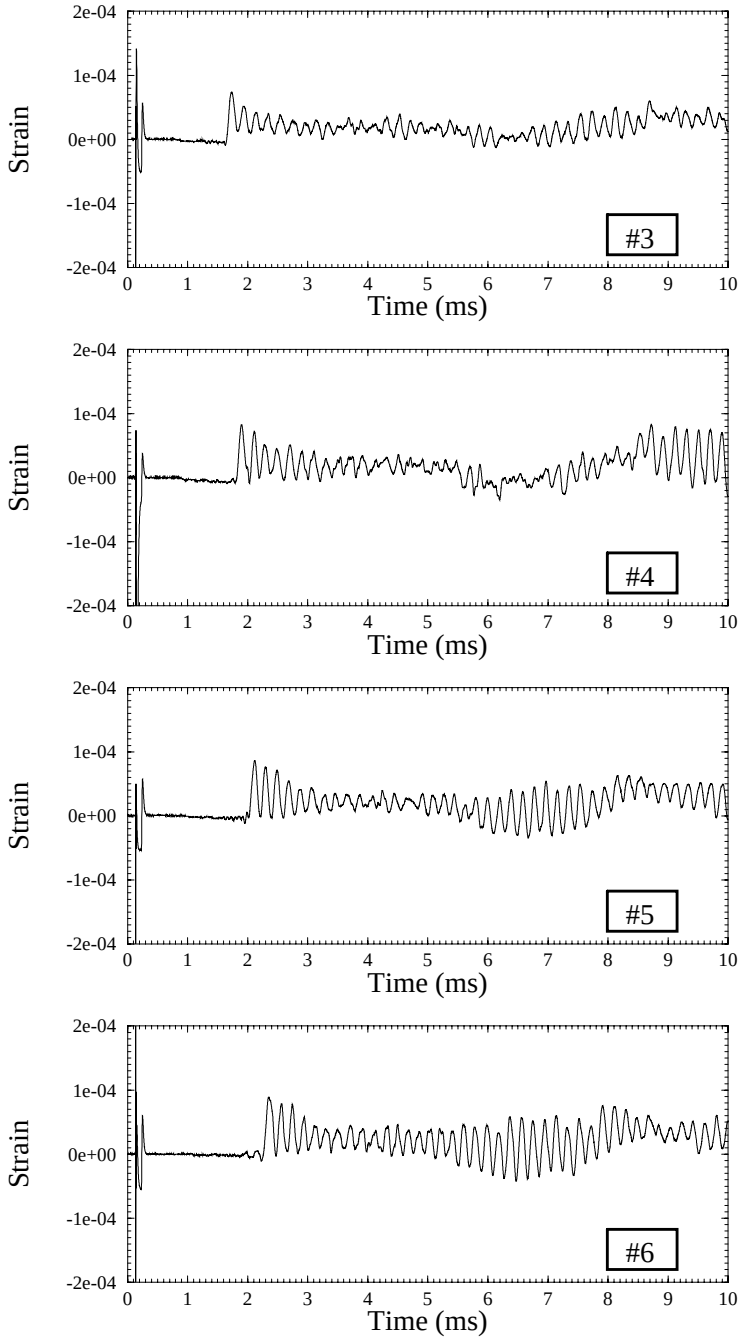

Figure 4.11: Strain signals for run 620: 1699.7 m/s

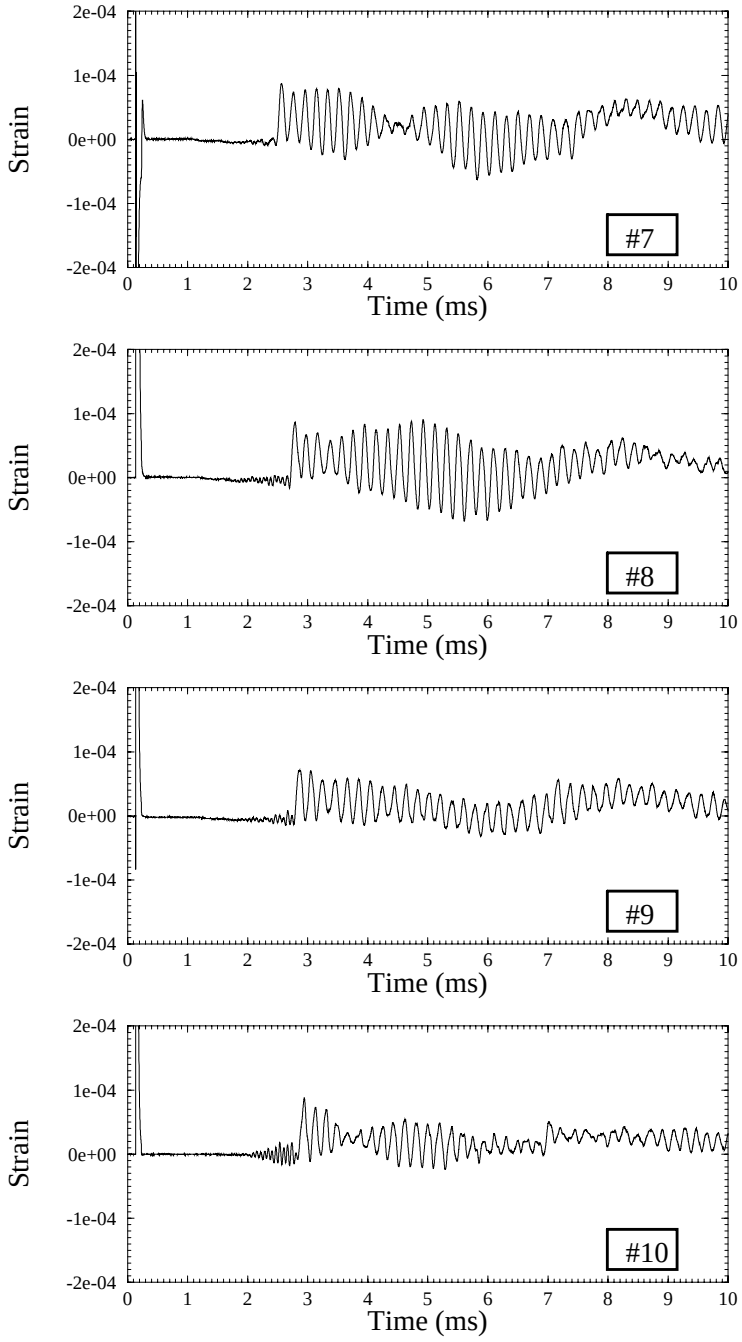

Figure 4.12: Strain signals for run 620: 1699.7 m/s

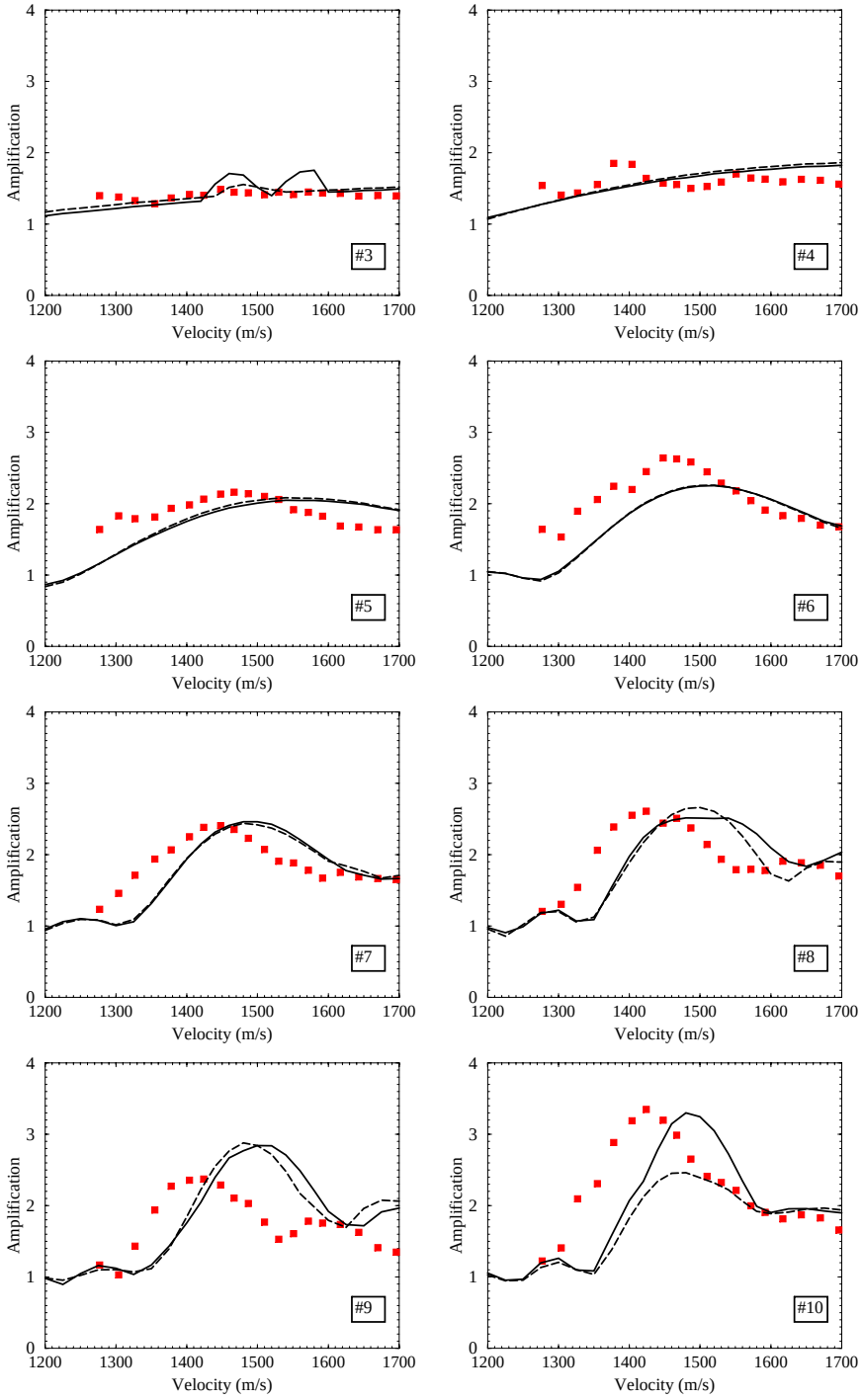

Figure 4.13: Development of profile. Solid: clamped. Dashed: simply supported

4.3 Flanges and end effects

The strain gages for these measurements are given in figure 4.14.

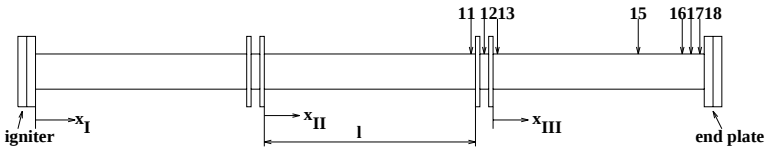

Figure 4.14: Gages to monitor flanges and end effects

Typical histories for a speed around the critical velocity are given in the figures 4.16 and 4.17. The corresponding pressure histories are given in figure 4.15. The amplification as a function of velocity is given in figure 4.18

Due to the reflection and interference of waves, the amplification for gage 11 is relatively high. The amplification however is smaller than the amplification for gage 10. The signal for the gage on the T-piece indicates that the radial deflection is not zero. The amplification for this gage varies around 1, which essentially means that it acts as a simple ring. The connection between the tube and the flange only transmits a part of the wave to the T-piece around the critical velocity. The strain history for this gages also shows different type of behaviour. The amplification curve for the gage 13, mounted just behind the flanges, shows no amplification effect. For the entire velocity range the amplification is essentially equal to one. This implies that the build up of the profile starts all over again. Thus the design of flanges and keys prevents adequate transmission of structural waves between tube sections.

The strains near the end of the tube are relatively large. At the end of the tube not only the structural waves, but also the detonation reflects. This causes very high strains over a relatively large velocity span. The strain traces show the reflection of waves and the passage of the reflected shock. For this velocity there is a relatively large precursor wave.

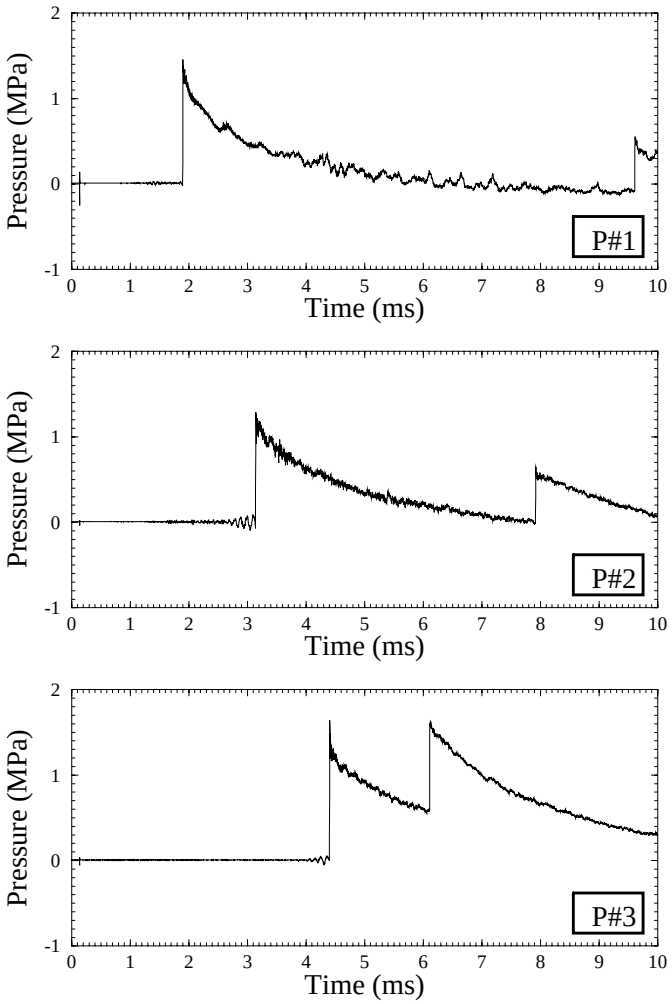

Figure 4.15: Pressure signals for run 628: 1478.8 m/s

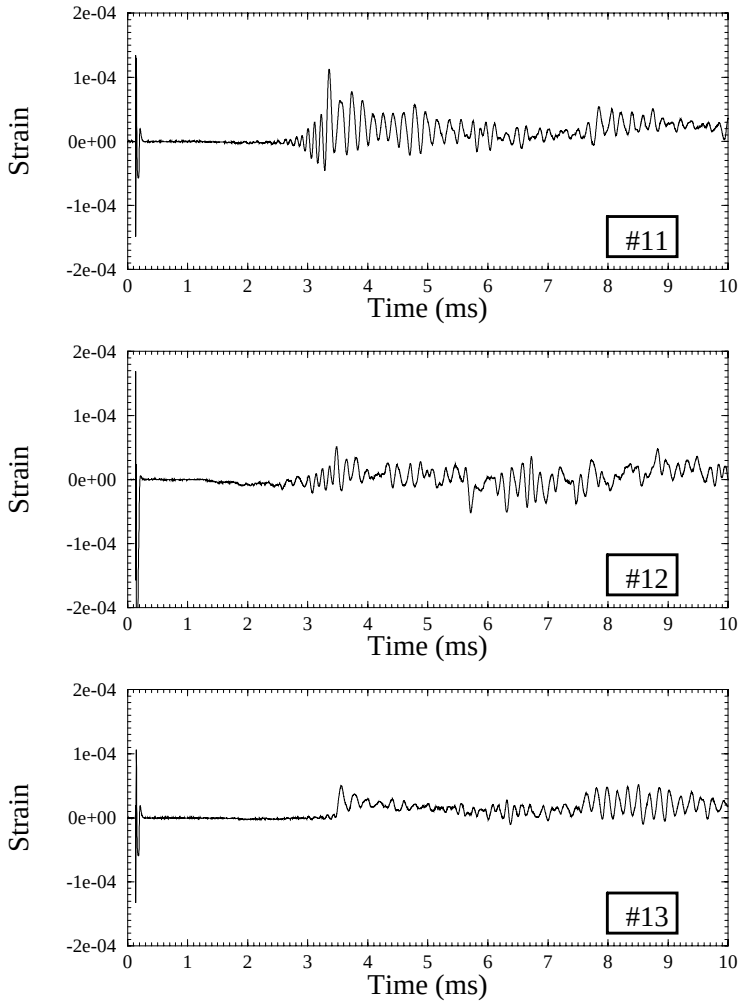

Figure 4.16: Strain signals for run 628: 1478.8 m/s

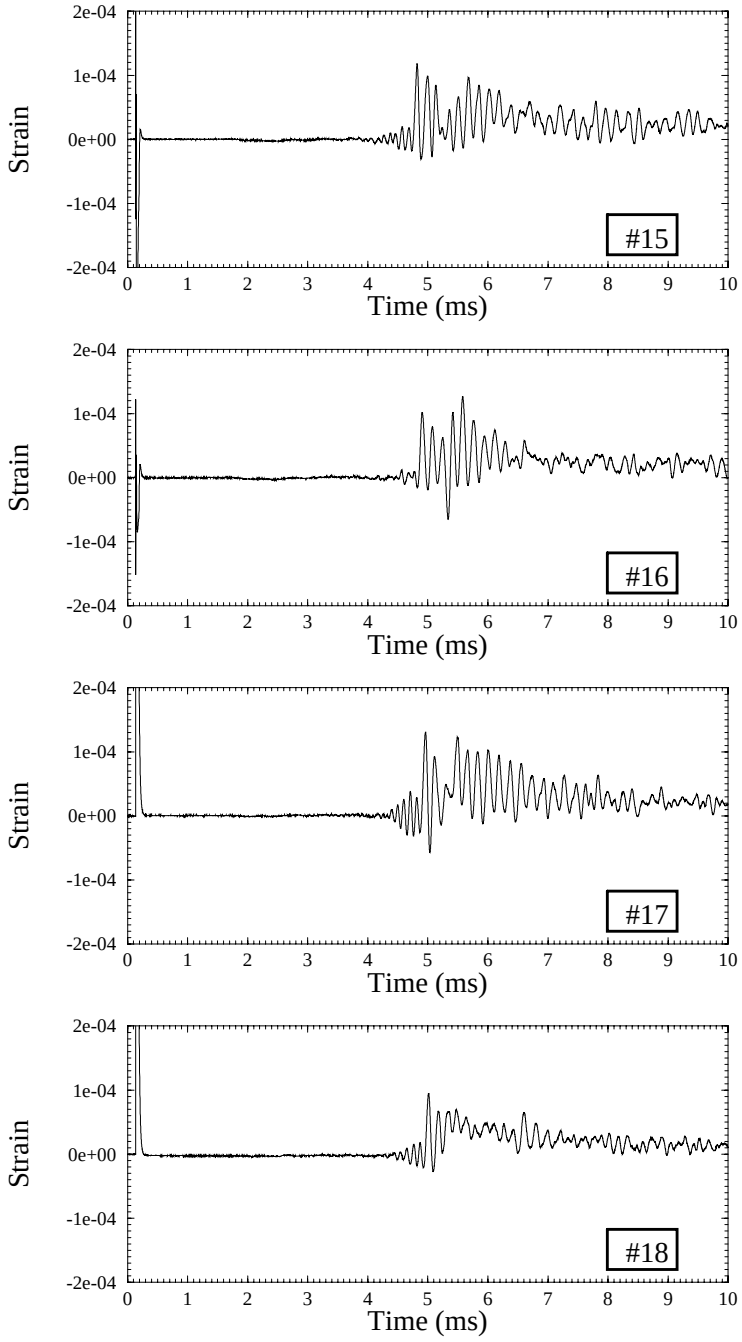

Figure 4.17: Strain signals for run 628: 1478.8 m/s

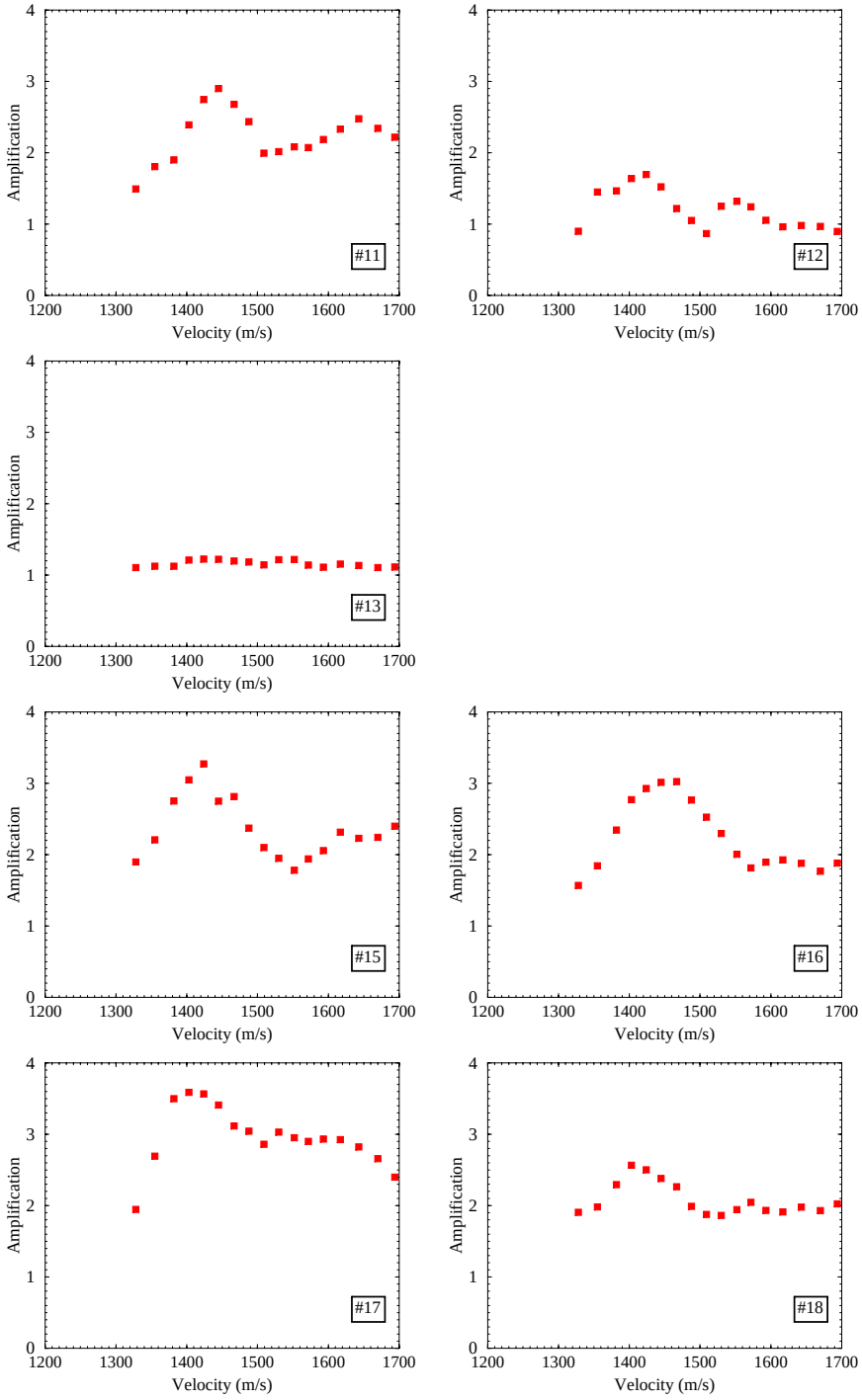

Figure 4.18: Experimental results for flanges and end effects

4.4 Linearity and comparison of sections

The strain gages for these measurements are given in figure 4.19.

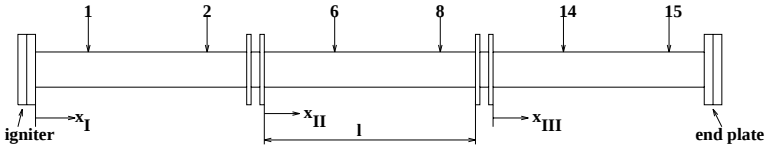

Figure 4.19: Gages to monitor linearity and compare sections

Typical histories for a supercritical velocity of 1999.0 m/s are given in the figures 4.21 and 4.22. The corresponding pressure histories are given in figure 4.20. The strain traces clearly indicate the the speed of the detonation is supercritical. The amplitude of the high frequency precursor is very low. The results for the gages 14 and 15 show the excitation due to the reflected shock. The pressure traces show why the measured pressure is not very reliable. Due to thermolizing effects the pressure drops below zero. Therefore a calculated value, the Chapman-Jouguet pressure, is used to obtain the amplification factor.

The amplification factor as a function of the pressure (Chapman-Jouguet pressure) is plotted in figure 4.23 for a velocity of 1800 m/s. The results for a velocity of 2000 m/s are given in figure 4.24. The figures show that the amplification factor is not a function of the pressure. In that sense the problem is linear. This is an important fact that supports the use of linear theory. When comparing the different sections, the amplification factor does not vary much. The identical positions on different sections show similar behaviour, except for gage 15. This gage shows a significantly higher amplification level due to the reflected wave. However, the conclusion that the sections behave similarly requires additional information. The amplification values for these supercritical speeds is in all cases (except gage 15) equal to 2, as predicted by simple models. The fact however that the profile has to develop all over again when entering a new tube section, supports the assumption that the tube can be regarded as a collection of independent sections.

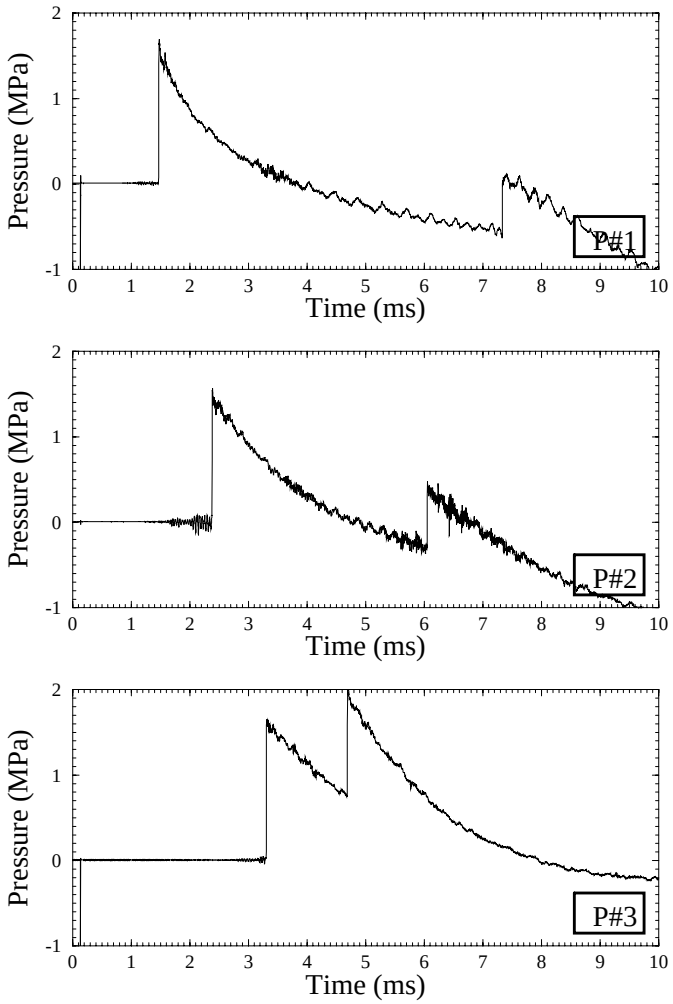

Figure 4.20: Pressure signals for run 648: 1999.0 m/s

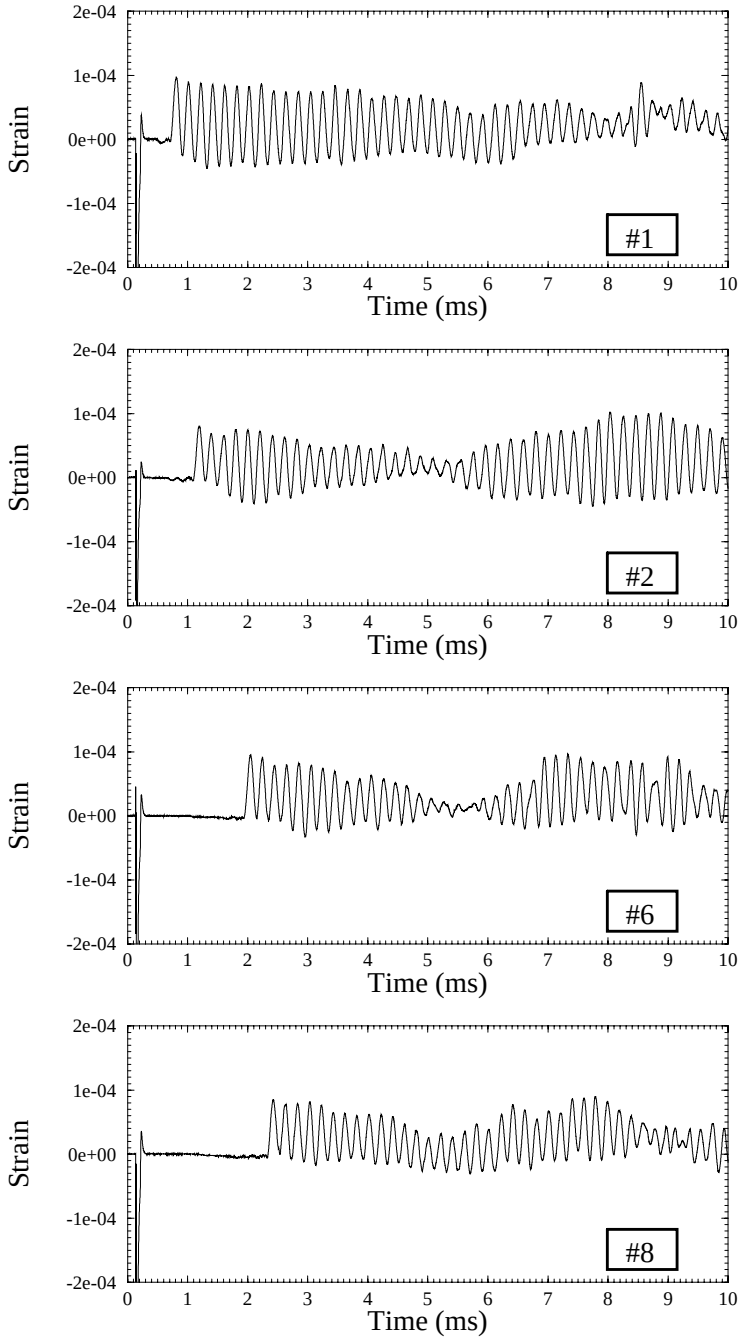

Figure 4.21: Strain signals for run 648: 1999.0 m/s

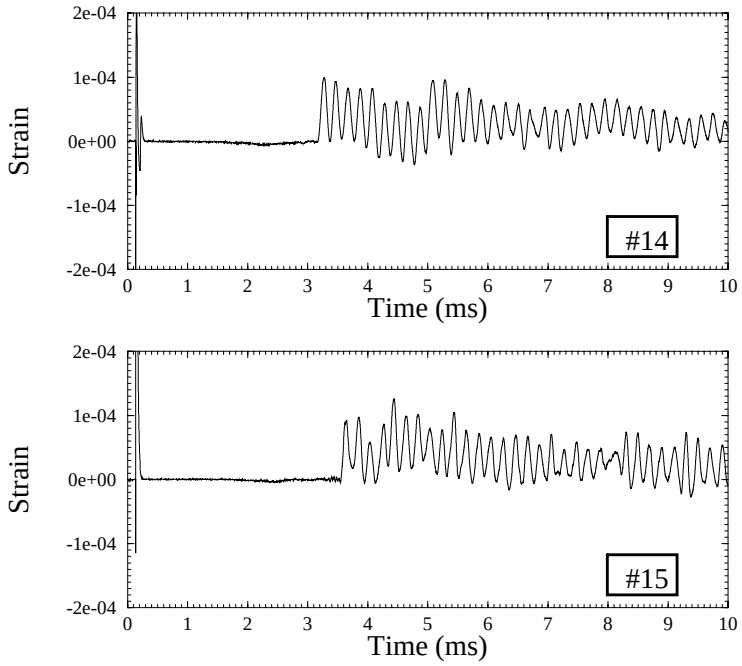

Figure 4.22: Strain signals for run 648: 1999.0 m/s

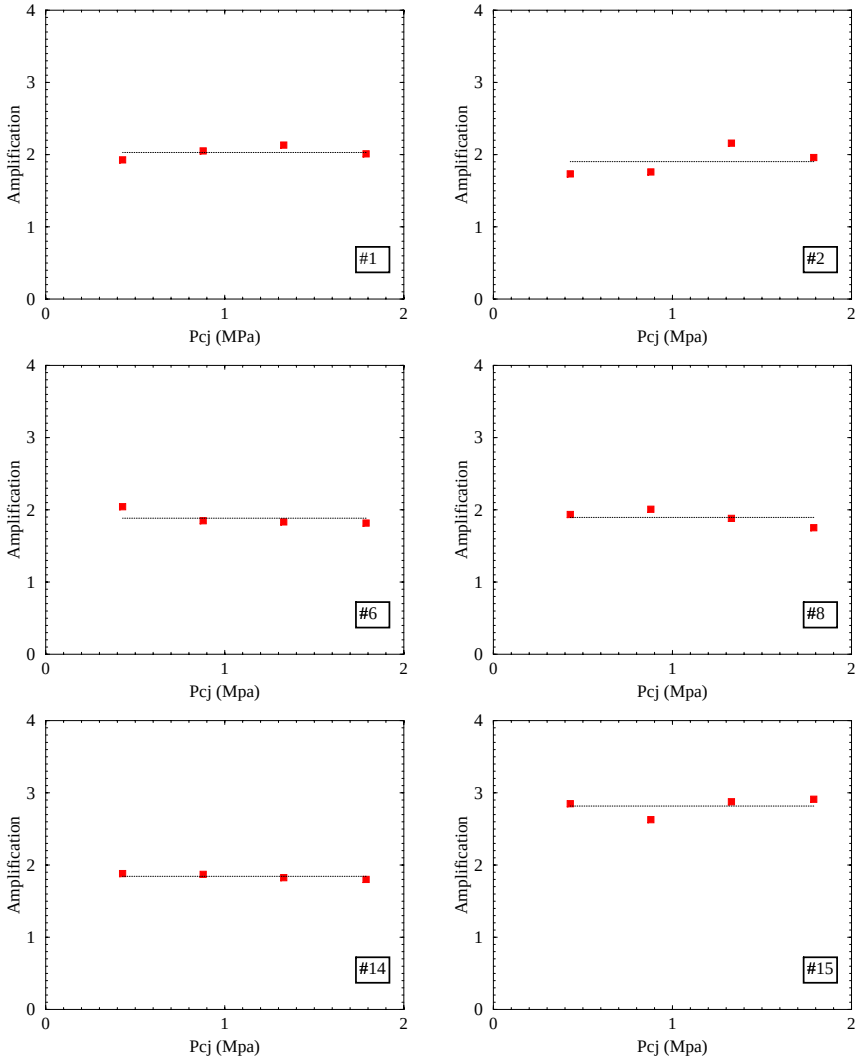

Figure 4.23: Experimental results for linearity/comparison shots at 1800 m/s

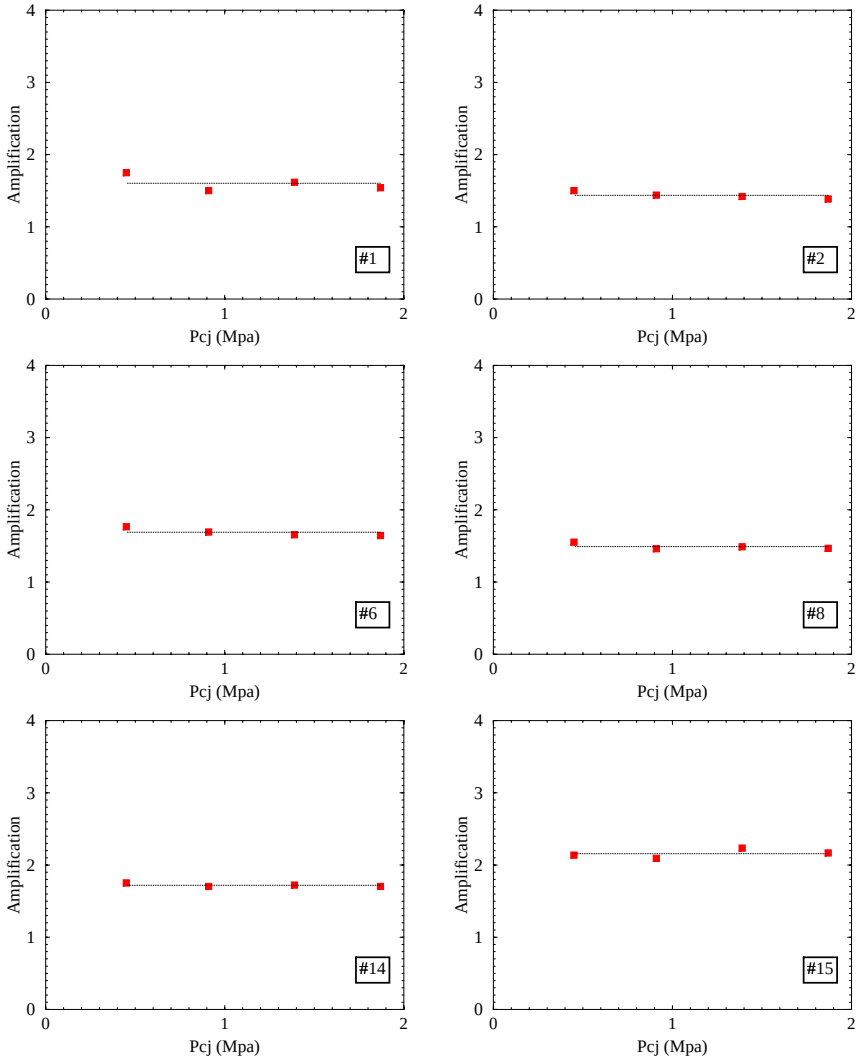

Figure 4.24: Experimental results for linearity/comparison shots at 2000 m/s

4.5 Cell size

The strain gages for this measurements are given in figure 4.25.

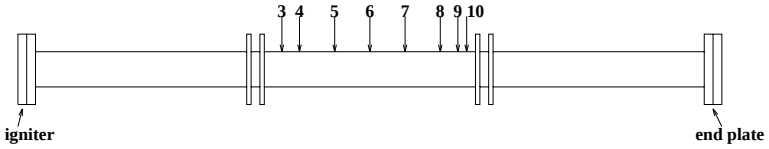

Figure 4.25: Gages for cell size shots

Typical strain histories for a velocity of 1267.4 m/s are given in the figures 4.27 and 4.28. The corresponding pressure histories are given in figure 4.26. The pressure loads are not very well defined. Due to the large amount of diluent and the low pressures, the cell size increases dramatically. The 3-dimensional structure becomes apparent as the distance between the transverse shocks increases. As a result, the loading of the tube is less smooth, especially for the third transducer. Due to this behaviour the reproducibility of the process is also less good. The change in excitation structure is also visible in the strain traces for the gages 8,9 and 10.

The amplification factor as a function of the Chapman-Jouguet pressure is given in figure 4.29 for a velocity of 1400 m/s. Since linearity was checked in section 4.4, the increase in amplification with decreasing pressure can be attributed to cell size effects. The cell size is inversly proportional to the pressure. The structural wave length is usually much larger than the cell size (0.2 m versus 5 mm). As the cell size increases, the ratio between the cell size and the strutural wave length increases. The figure indicates that the amplification is a function of the ratio between the structural wavelength and the cell size. When the cell size is of the same order of magnitude as the wavelength, the flexural waves in the tube are very well excited.

The amplification factor as a function of the Chapman-Jouguet pressure is given in figure 4.30 for a velocity of 1267.4 m/s. The amplification increases with decreasing pressure. The increase in amplification can be attributed to cell size effects. However, for very low pressures the amplification seems to decrease again. This can be explained by analyzing the pressure and strain histories. The pressure histories for the 1400 m/s shot are relatively well defined. However, for a velocity of 1267.4 m/s and a very low pressure, the pressure history for the third transducer shows a very nonsmooth behaviour. There is a large spike followed by a number of smaller spikes. The distance between these spikes increases as the cell width increases. The decrease in amplification at very large cell widths is therefore due to the breakdown of the excitation.

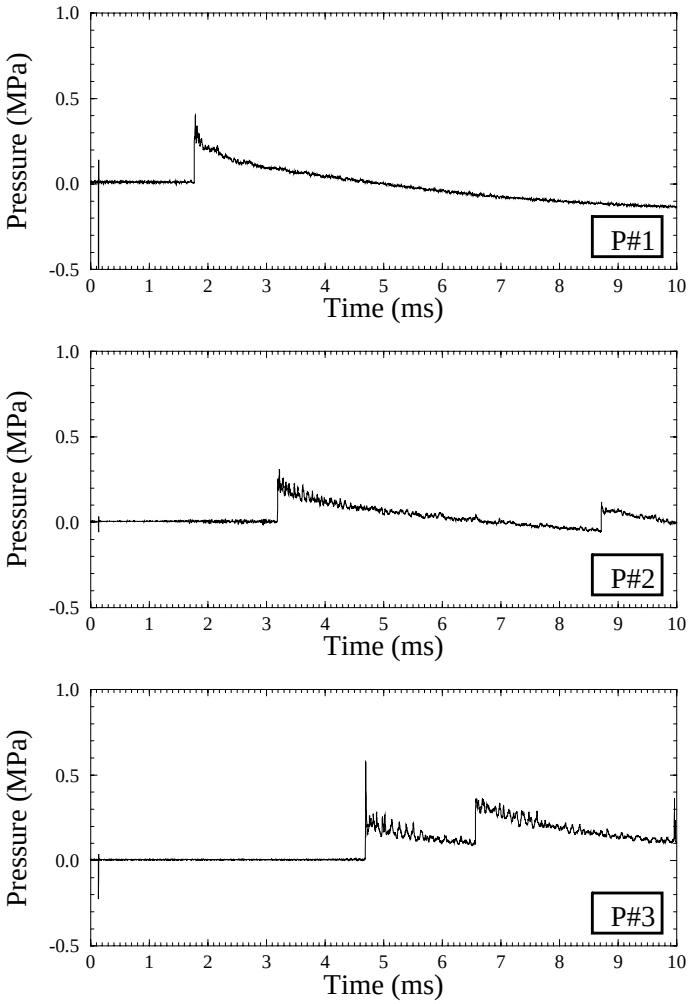

Figure 4.26: Pressure signals for run 659: 1267.4 m/s

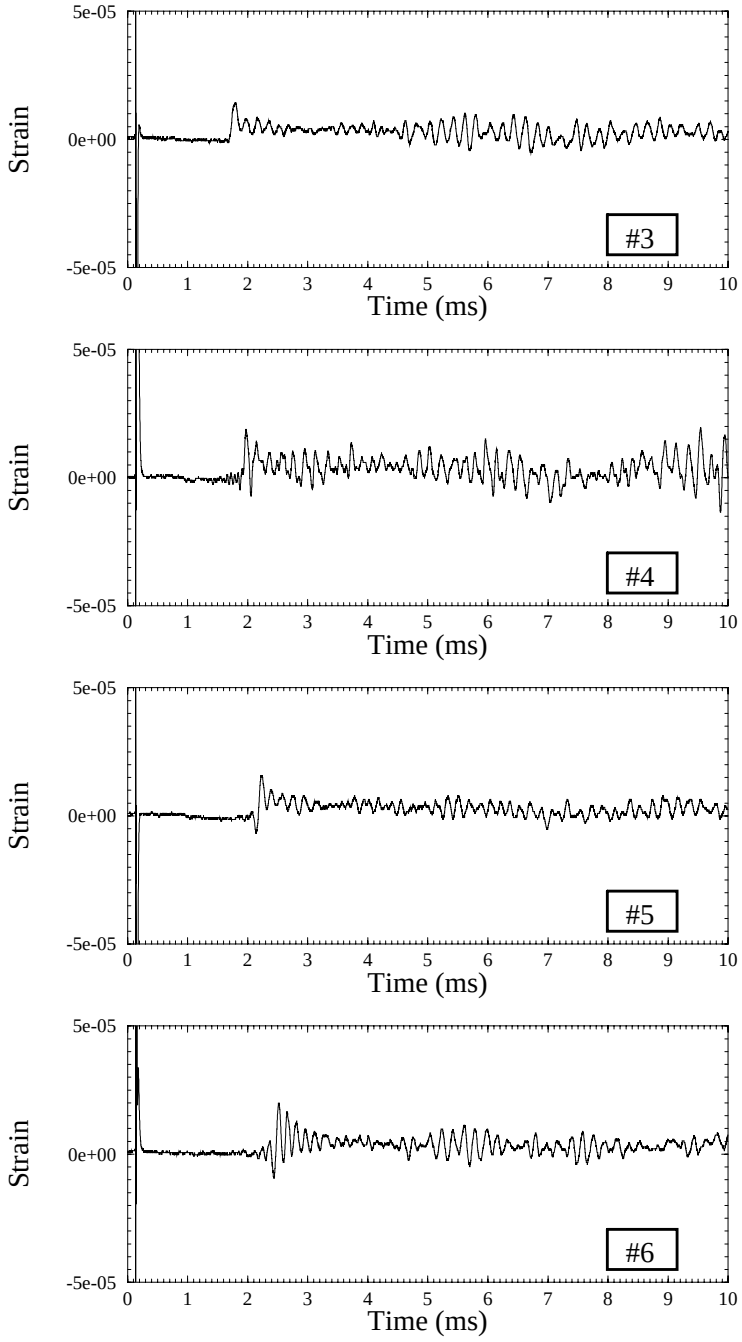

Figure 4.27: Strain signals for run 659: 1267.4 m/s

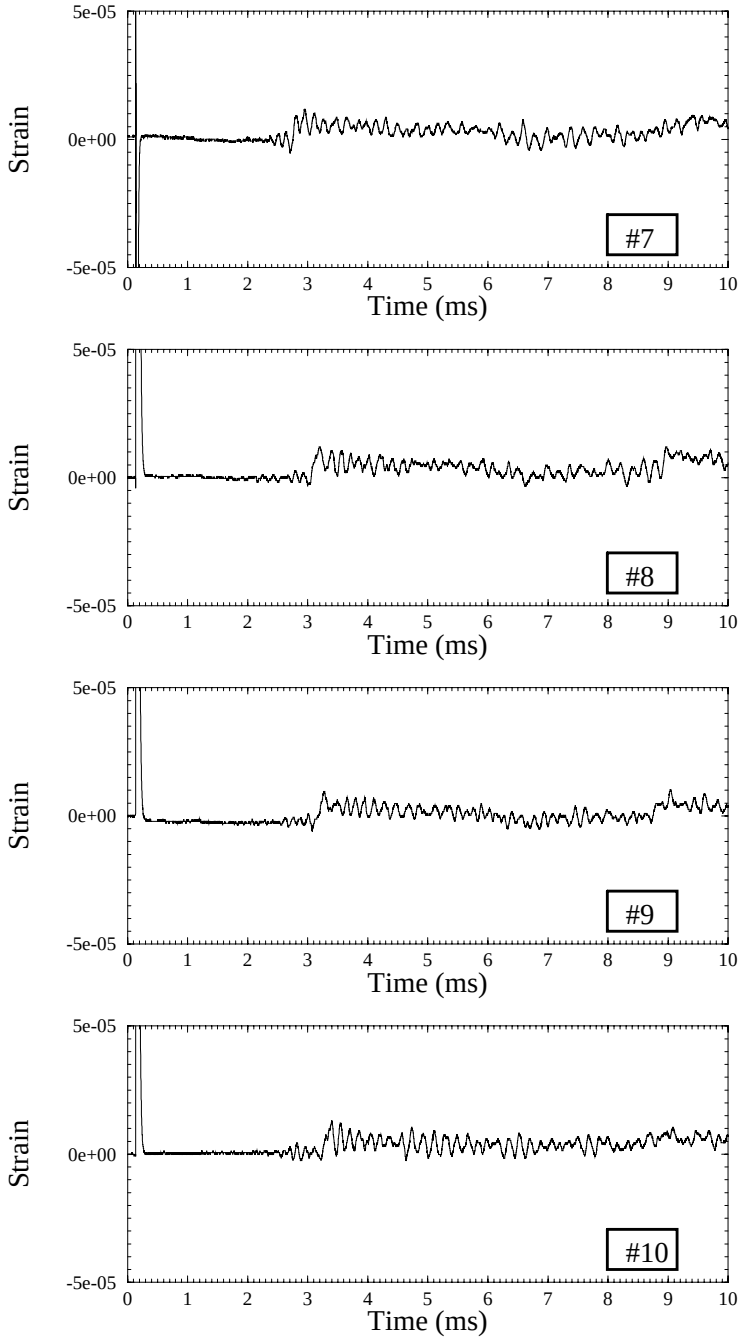

Figure 4.28: Strain signals for run 659: 1267.4 m/s

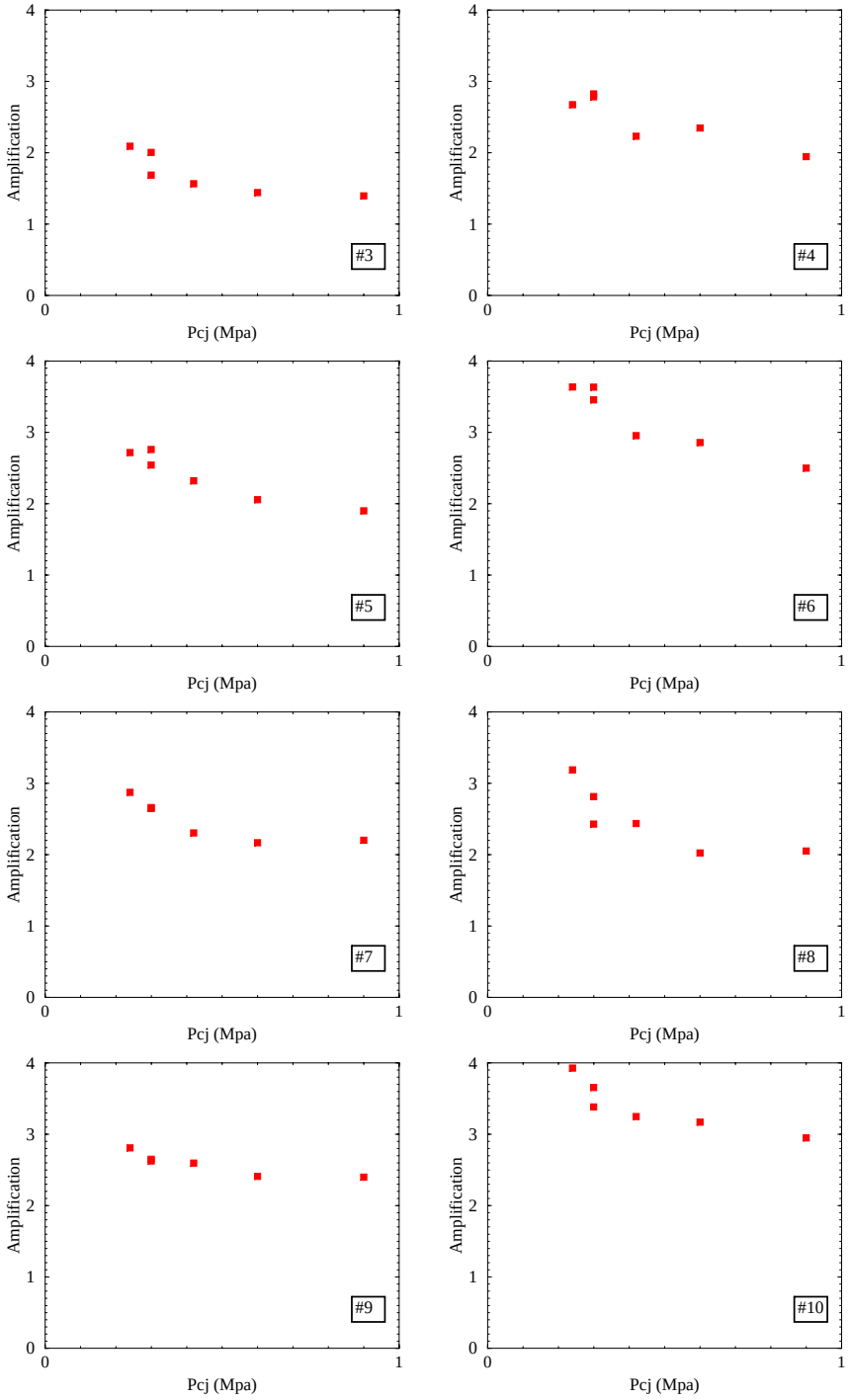

Figure 4.29: Experimental results for cell size shots at 1400.1 m/s

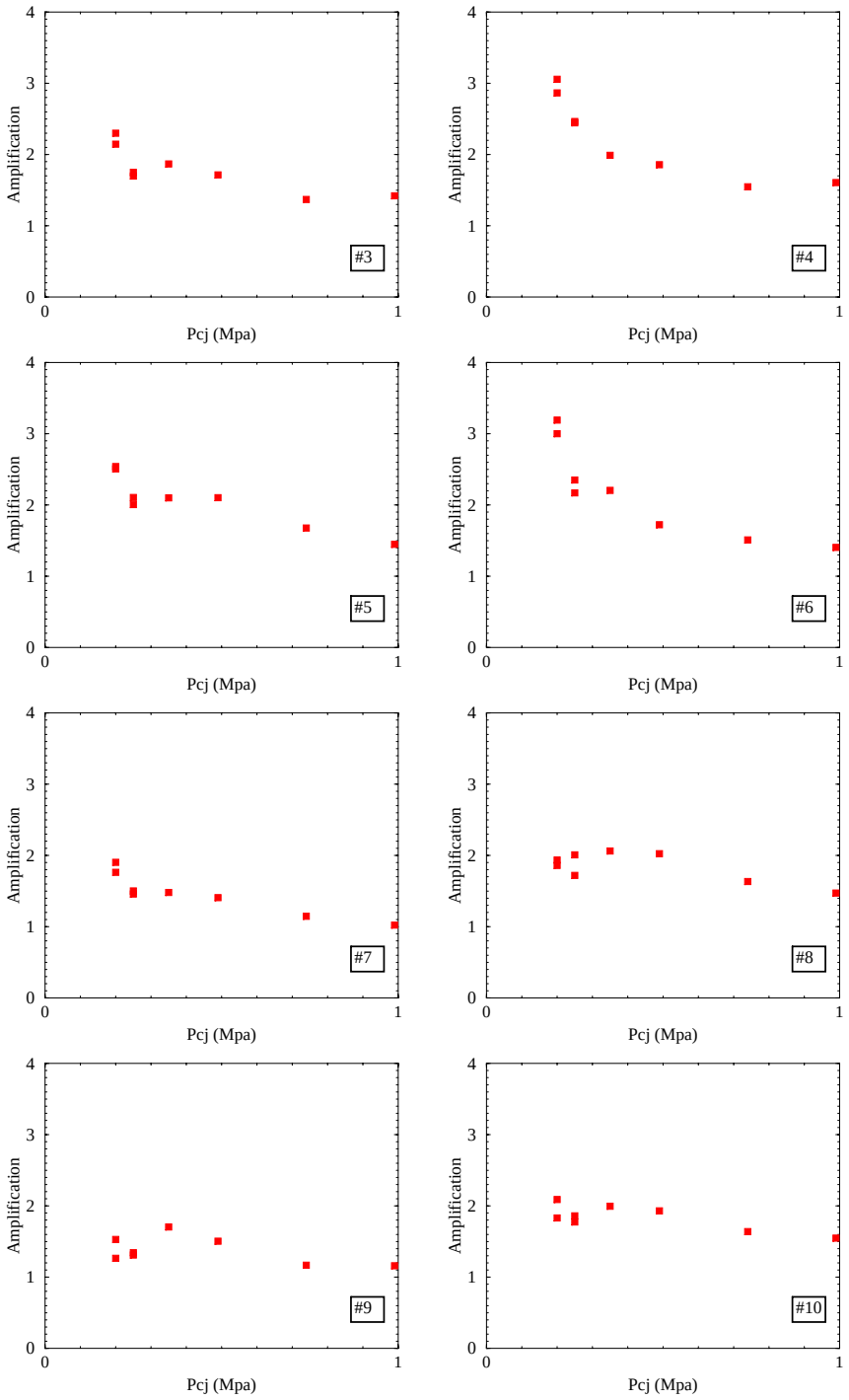

Figure 4.30: Experimental results for cell size shots at 1267.4 m/s

4.6 High velocity shots

The strain gages for this measurements are given in figure 4.31.

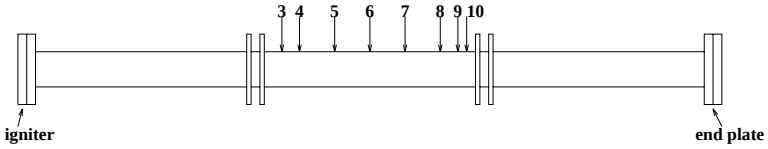

Figure 4.31: Gages for high velocity shots

Typical strain histories for a velocity of 2803.0 m/s are given in the figures 4.33 and 4.34. The corresponding pressure histories are given in figure 4.32. The pressure signals show the thermolizing effect. The strain signals indicate supercritical behaviour. The maximum amplitude is nearly constant as a function of distance. The amplification factor as a function of the velocity is given in figure 4.35. The calculations and the experiments show reasonable agreement. For gage 10 there is a broad peak in the calculated amplification curves at 2000 m/s. By analyzing the strain signals, these peaks are due to successive reflection and interference of waves (see also section 4.2).

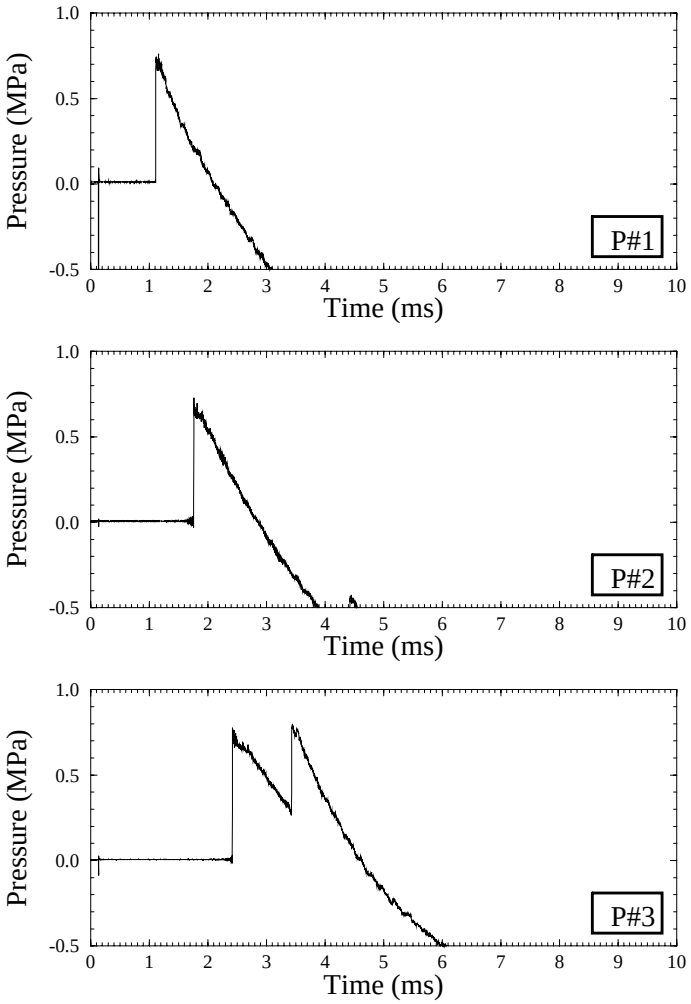

Figure 4.32: Pressure signals for run 678: 2803.0 m/s

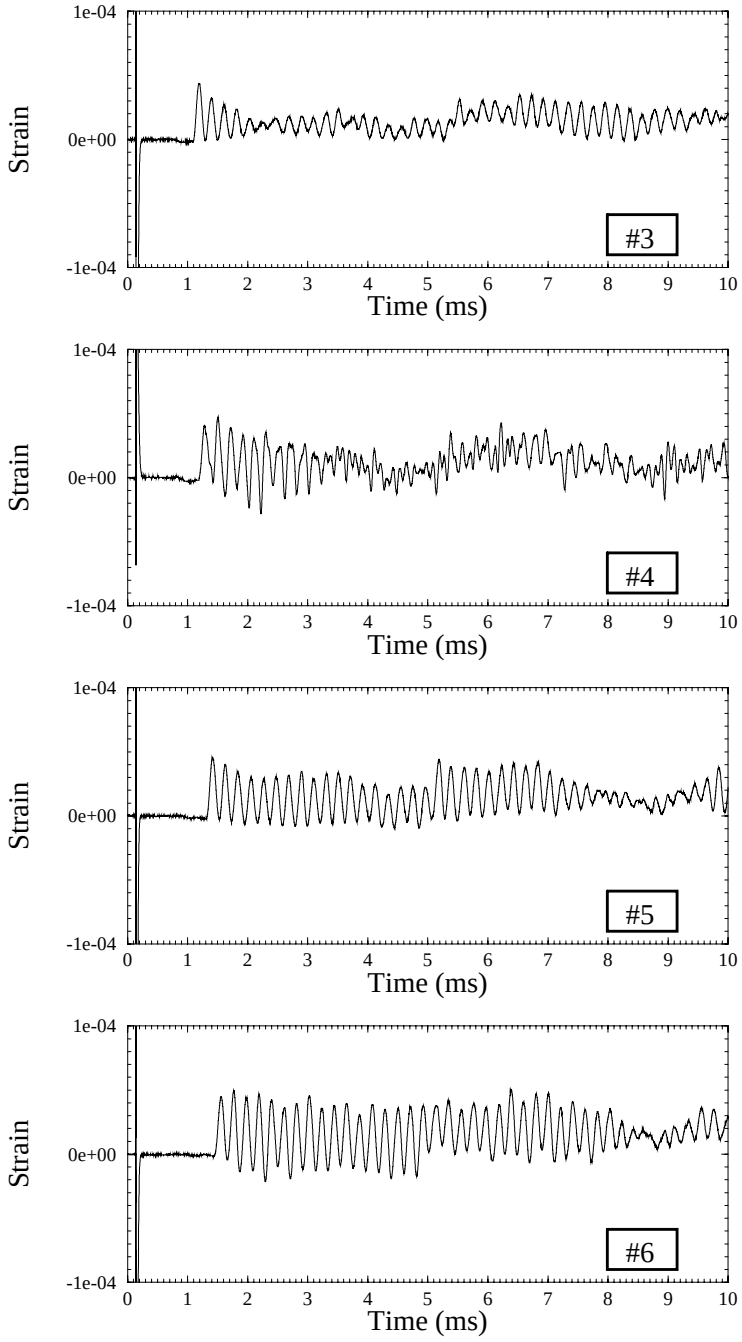

Figure 4.33: Strain signals for run 678: 2803.0 m/s

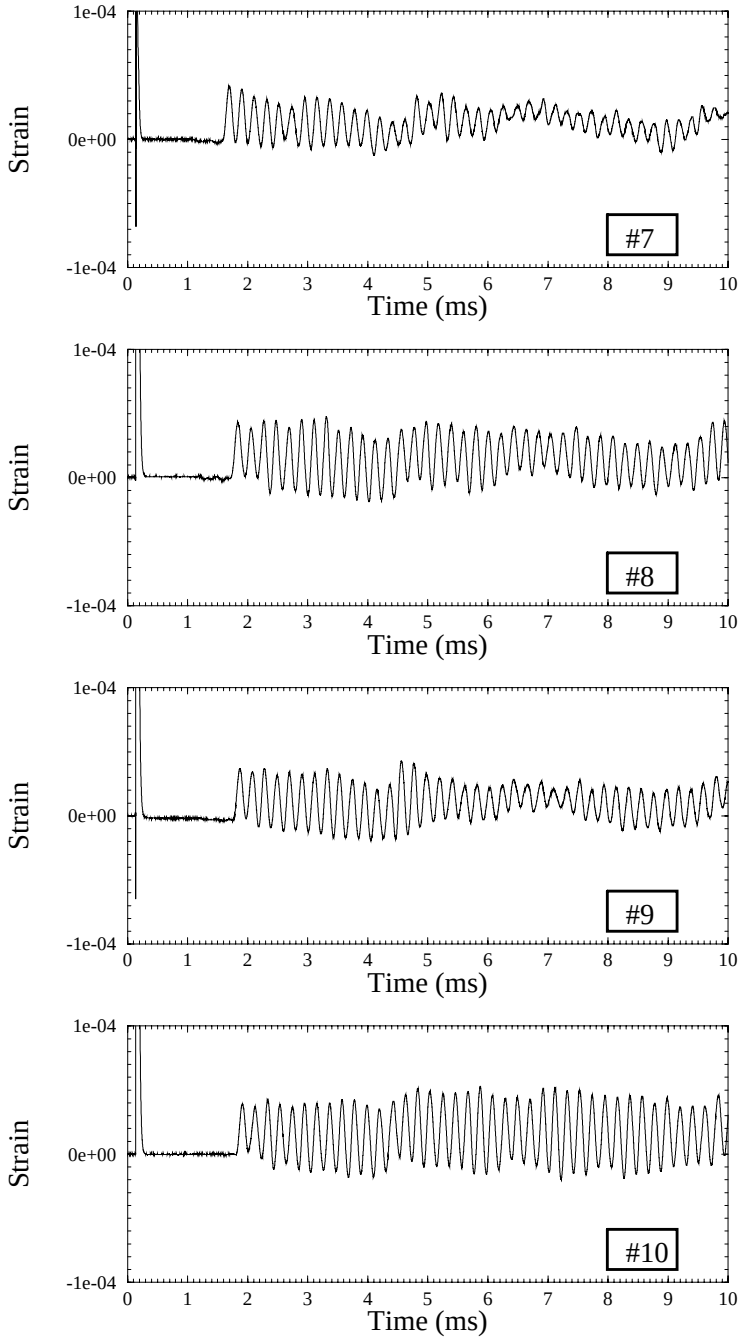

Figure 4.34: Strain signals for run 678: 2803.0 m/s

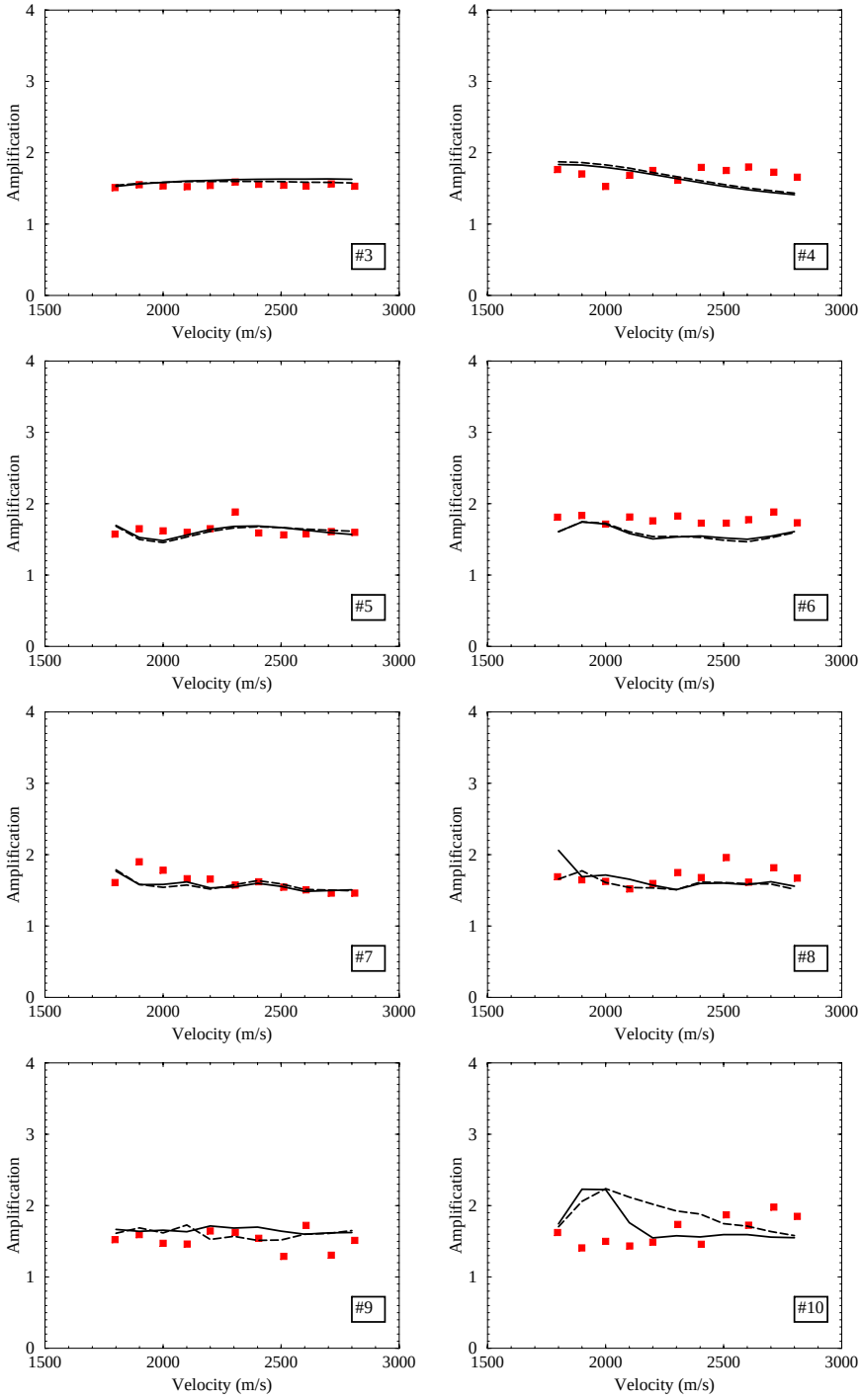

Figure 4.35: Results high velocity shots

4.7 Total velocity range

The results for the development measurements and the high velocity measurements are now combined to visualize the behaviour of the tube over the total velocity range.The strain gages are given in figure 4.36.

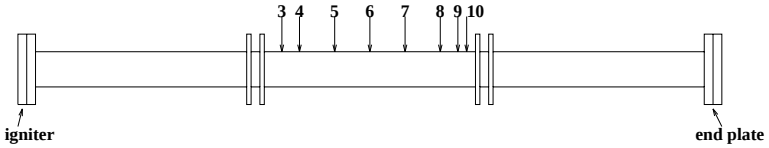

Figure 4.36: Gages for development and high velocity shots

The measured and calculated curves are given in figure 4.37. The general agreement between theory and measurements is reasonable, when taking into account the simplicity of the models and the variation in the input data. The amplification around the critical velocity is predicted fairly well.

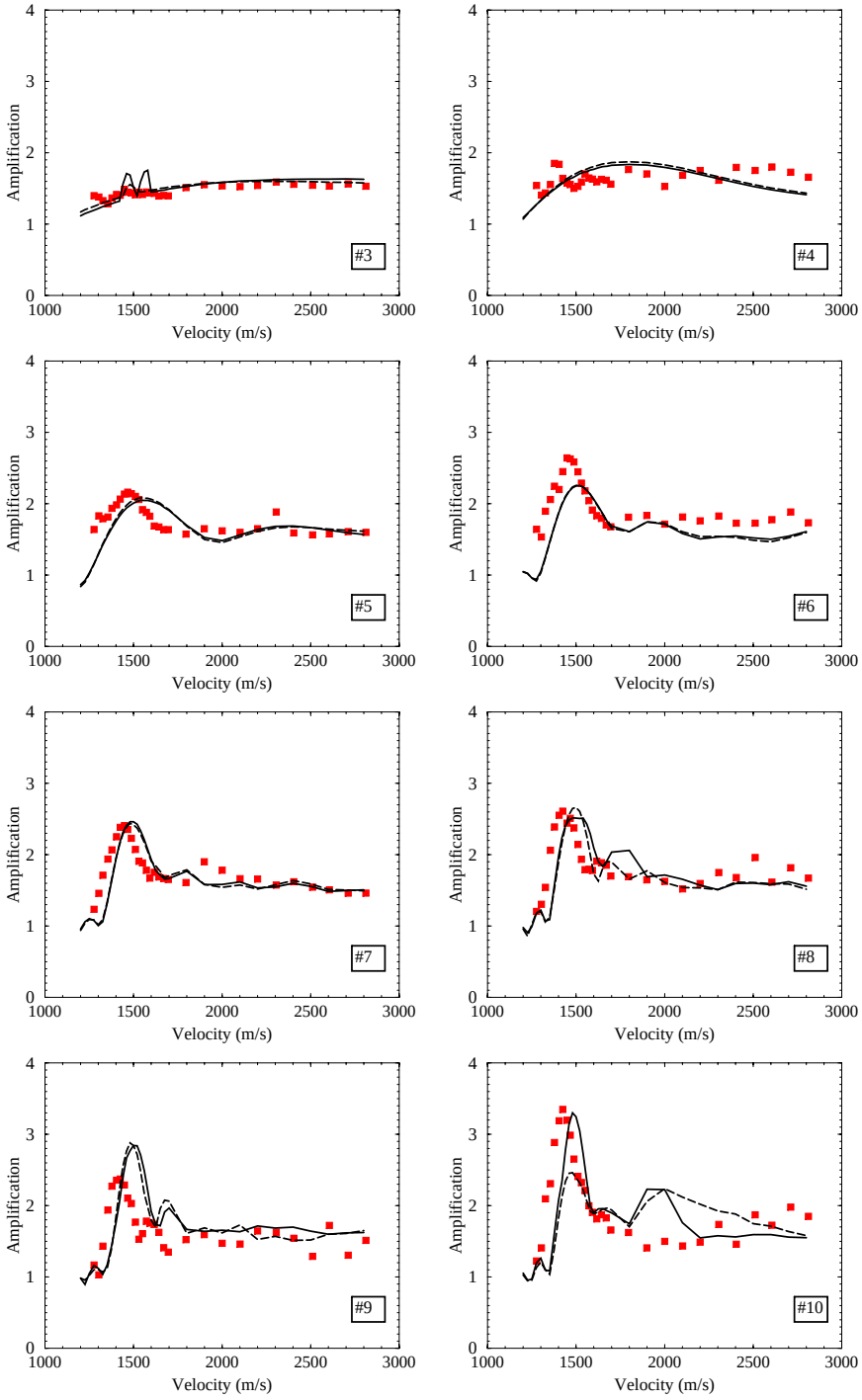

Figure 4.37: Results total velocity range

Conclusions

The following conclusions are drawn from the present investigation:

- The critical velocity for the GALCIT detonation tube is 1450 m/s. The existance of a critical velocity was experimentally verified. Amplification factors in the ranging from 1 to 4 were measured.
- The critical velocity concept is important for tube design. In the operational range of the tube amplifications of 3 to 3.5 were measured. It is evident that this should be incorporated in detonation tube design.
- Calculations and experiments show fair agreement. The finite element results predict the transient development of the profile. The calculations for a clamped tube show reasonable agreement with the experimental results.
- The deflection profile has to develop. Measurements indicate that the flanges cut off the waves: when the detonation enters a new tube section the profile has to develop all over again.
- The reflection and interference of waves leads to high strains. Measurements and calculations show that structural waves are reflected at the flanges and at the end of the tube. The reflection of waves at the flanges leads to strains that are about 1.3 times the strain without interference. Since at the end the detonation also reflects, amplifications were especially high near the end of the tube.
- The structural response of the tube is linear with respect to the pressure load. The experiments indicate that the amplification factor is not affected by the excitation level.
- The cell size of the detonation affects the amplification factor. The ratio between the cell size and the structural wave length is important. When the cell size and the structural wave length are of the same order of magnitude, the flexural wave are excited well. This leads to the highest amplification factor measured in the present study: 4. Large cell sizes are usually obtained at very low pressures, so for tube design this aspect should be of less concern.

Bibliography

[1] T.J. Anderson and E.K. Dabora. Measurements of normal detonation wave structure using rayleigh imaging. *24th Symp. Int. Combust. Proc.*, pages 1853–1860, 1992.

[2] H.O. Barthel. Predicted spacings in hydrogen-oxygen-argon detonations. *Phys. Fluids*, 17(8):1547–1553, 1974.

[3] R.K. Kumar. Detonation cell widths in hydrogen-oxygen-diluent mixtures. *Combust. Flame*, 80(2):157–169, 1990.

[4] J.H Lee and H. Matsui. A comparison of the critical energies for direct initiation of spherical detonation in acetylene-oxygen mixtures. *Combust. Flame*, 28(1):61–66, 1977.

[5] R.A. Strehlow. Transverse waves in detonations: Ii. structure and spacing in h_2-o_2, c_2h_2-o_2, c_2h_4-o_2 and ch_4-o_2 systems. *AIAA Journal*, 7(3):492–496, 1969.

[6] R.A. Strehlow, R. Liangminas, R.H. Watson, and J.R. Eyman. Transverse wave structure in detonations. *11th Symp. Int. Combust. Proc.*, pages 683–692, 1967.

[7] R.A. Strehlow, R.E. Maurer, , and S. Rajan. Transverse waves in detonations: I. spacings in the hydrogen-oxygen system. *AIAA Journal*, 2(7):323–328, 1969.

[8] J.E. Shepherd. Pressure loads and structural response on the BNL high-temperature detonation tube. Technical Report A-3991, Brookhaven National Laboratory, Upton, New York 11973, September 1992.

[9] H. Reismann. Response of a pre-stressed cylindrical shell to moving pressure load. In S. Ostrach and R.H. Scanlon, editors, *Eighth Midwest Mechanics Conference*, pages 349–363. Pergamon Press, 1965.

[10] S. Tang. Dynamic response of a tube under moving pressure. In *Proceedings of the American Society of Civil Engineers*, volume 5, pages 97–122. Engineering Mechanics Division, October 1965.

[11] T.E. Simkins. Resonance of flexural waves in gun tubes. Technical Report ARCCB–TR–87008, US Army Armament Research, Development and Engineering Center, Watervliet, N.Y. 12189–4050, July 1987.

[12] M.C. de Malherbe, R.D. Wing, A.J. Laderman, and A.K. Oppenheim. Response of a cylindrical shell to internal blast loading. *Journal of Mechanical Engineering Science*, 8(1):91–98, 1966.

[13] E. Burcsu and L. Zuhal. Effect of shock loading on circular tubes. Technical Report Ae 104 c, California Institute of Technology, Galcit, Pasadena 91125, 1997.

[14] M. El-Raheb and P. Wagner. Harmonic response of cylindrical and toroidal shells to an internal acoustic field. part i: Theory. *Journal of the Acoustical Society of America*, 78(2), 1985.

[15] M. El-Raheb and P. Wagner. Acoustic radiation from a shell with internal structures. *Journal of the Acoustical Society of America*, 85(6):2452–2464, 1989.

[16] I. Mirsky and G. Herrmann. Axially symmetric motions of thick cylindrical shells. *Journal of Applied Mechanics*, 1958.

[17] E. Schultz. Strain measurements in detonation experiments. Technical report, California institute of technology, GALCIT, Pasadena 91125, 1997. Internal report.

[18] J. Mackerle. Structural response to impact, blast and shock loadings. a FE/BE bibliography (1993–1995). *Finite Elements in Analysis and Design*, 24:95–110, 1996.

[19] J.E. Rieker, Y.H. Lin, and M.W. Trethewey. Discretization considerations in moving load finite element beam models. *Finite elements in analysis and design*, 21:129–144, 1996.

[20] H.A. Dieterman and A.V. Metrikine. Steady-state displacements of a beam on an elastic half-space due to a uniformly moving constant load. *European Journal of Mechanics, A/solids*, 16(2):295–306, 1997.

[21] H.A. Dieterman and A. Metrikine. The equivalent stiffness of a half-space interacting with a beam. critical velocities of a moving load along the beam. *European Journal of Mechanics, A/Solids*, 15(1):67–90, 1996.

[22] N.S. Remez and I.A. Luchko. Deformation of a thick-walled cylindrical shell with a porous filler under an internal blast loading. *International journal Applied Mechanics*, 31(9):742–746, 1995.

[23] Q.M. Li and N. Jones. Blast loading of a "short" cylindrical shell with transverse shear effects. *International journal impact engineering*, 16(2):331–353, 1995.

[24] S. Ḿuller, T. Kryżyński, and H. Ilias. Comparison os semi-analytical methods of analyzing periodic structures under a moving load. *Vehicle system dynamics supplement*, 24:325–339, 1995.

[25] M.R. Eslami, M. Shakeri, and R. Sedaghatti. Coupled thermoelasticity of an axially symmetric cylindrical shell. *Journal of thermal stresses*, 17:115–135, 1994.

[26] A.I. Bezverkhii and V.P. Mukoid. Reaction of a thick-walled cylindrical shell to a suddenly applied internal load. *International journal Applied Mechanics*, 30(6):441–445, 1994.

[27] A.V. Metrikin. Stationary waves in a nonlinear elastic system interacting with a moving load. *Acoustical physics*, 40(4):573–576, 1994.

[28] G. Mareska, P.P. Millela, and G. Pino. Structural response of a nuclear power plant steel containment under H2 detonation. *Nuclear engineering and design*, 40:119–126, 1993.

[29] G. Pan, H. Okada, and S.N. Atluri. Nonlinear transient dynamic analysis of soil-pavement interaction under moving load: a coupled BEM-FEM approach. *Engineering Analysis with Boundary Elements*, 14:99–112, 1994.

[30] J. Pitḱaranta, Y. Leino, O. Ovaskainen, and J. Piila. Shell deformation states and the finite element method: a benchmark study of cylindrical shells. *Computational Methods in Applied Mechanical Engineering*, 128:81–121, 1995.

[31] K.R Sivadas and N. Ganesan. Axisymmetric vibration analysis of thick cylindrical shell with variable thickness. *Journal of sound and vibration*, 160(3):387–400, 1993.

[32] T.P. Chang and Y.N. Liu. Dynamic finite element analysis of a nonlinear beam subjected to a moving load. *International journal Solids and Structures*, 33(12):1673–1688, 1996.

[33] P.W. Smith, J.G. McDaniel, K.D. LePage, and R. Barile. Structural wave reflection coefficients of cylindrical shell terminations: numerical extraction and reciprocity constraints. *Journal of the acoustical society of America*, 101(2):900–908, 1997.

[34] S.F. Felszeghy. The Timoshenko beam on an elastic foundation and subject to a moving step load, part I: steady-state response. *Journal of Vibration and Acoustics*, 118:277–284, 1996.

[35] S.F. Felszeghy. The Timoshenko beam on an elastic foundation and subject to a moving step load, part II: transient response. *Journal of Vibration and Acoustics*, 118:285–291, 1996.

[36] M.D. Olson. Efficient modelling of blast loaded stiffened plate and cylindrical shell structures. *Computers and structures*, 40(5):1139–1149, 1991.

[37] J. Jiang and M.D. Olson. Nonlinear dynamic analysis of blast loaded cylindrical shell. *Computers and structures*, 41(1):41–52, 1991.

[38] D.W. Tennant. Response and failure of internal structural subsystems under blast and shock loading. *Journal of pressure vessel technology*, 116:409–418, 1994.

Appendix A

Shot checklist

GDT Shot Checklist (No Ammonia) Last Modified: 26 November 1997

Shot: _____ Date: _____ Time: _____

Operator(s): _____ Series: _____

Estimated reflected wave pressure: _____ bar Driver Controller Settings:

Ignition Delay		sec
Flow Duration		sec

Preparation and Pump Down

1. ___ Load firing plug with wire
2. ___ Check that clamp bolts are snug and clamp movement is clear
3. ___ Mount firing plug in place; do not force in
4. ___ Make sure that the soot foil anchor is secure
5. ___ Align endplate with tube end and make contact between sealing surfaces
6. ___ Check that Driver Controller is off
7. ___ Enable Main Control Panel power
8. ___ Turn on Main Control Panel 12 V relay and close it
9. ___ Open E1 (circulation valve)
10. ___ Open T1, T2 (and T3) (detonation tube isolation valves)
11. ___ Open V1 and V2 (vacuum isolation valves)
12. ___ Switch on thermocouple vacuum gauge (TG1 or TG2) and Heise pressure gauge
13. ___ Open G1 (gas supply isolation valve)
14. ___ Open N1 (gas supply needle valve)
15. ___ Close L1 (vacuum manifold leak-up valve)
16. ___ Check that EDL is not using vacuum pump
17. ___ Open vacuum manifold valve (at pump); set vacuum pump status indicator
18. ___ When firing plug is sucked in place, align backing plate under clamps
19. ___ Pressurize hydraulics; make sure all clamps engage backing plate surface

20. ___ Pressurize hydraulics above 3500 psi
21. ___ **Tighten endplate bolts**
22. ___ Connect Capacitor Box to Firing Plug
23. ___ Check bridge wire continuity
24. ___ Wait for pressure to drop below 50 millitorr - Final level: _____ millitorr
25. ___ Set Heise gauge zero
26. ___ Close V1 and V2 (vacuum isolation valves)
27. ___ Close vacuum manifold valve (at pump); set vacuum pump status indicator

Gas Fill Procedure

28. ___ Turn off thermocouple vacuum gauge
29. ___ **Check that end flange bolts are tight**
30. ___ **Check that hydraulic pressure is above 3500 psi**
31. ___ Turn on warning lights and check that doors are closed - **Laboratory Access is Restricted**
32. ___ Turn on gas supply wall switch

    Fill to desired pressure using external block valves, gas supply valves, and N1. If atmospheric air is used, fill it first, using V1 and L1.

Gas	Target Fraction	Target Partial Pressure	Target Final Pressure	Final Pressure
		kPa	kPa	kPa
		kPa	kPa	kPa
		kPa	kPa	kPa
		kPa	kPa	kPa
		kPa	kPa	kPa

33. ___ Turn off gas supply wall switch
34. ___ Close N1 and gas supply ball valves
35. ___ Run circulation pump for 5 minutes
36. Final pressure: _____ kPa Final Temperature: _____ °C
37. ___ Close T1, T2 (and T3)
38. ___ Close E1 and G1
39. ___ Open L1 to vent vacuum manifold

Firing Procedure

40. ___ Arm data acquisition system(s)
41. ___ Close Heise gauge isolation valve(s)
42. ___ Turn off electronic Heise gauge
43. ___ Align tube to "fire" position; check that movement is free.
44. ___ Switch off 12 V relay (on Main Control Panel)
45. ___ Check that Fire Ready light is on
46. ___ Switch TM-11 Toggle to *Driver Controller*
47. ___ Turn on Driver Controller
48. ___ Remove shorting cable from capacitors
49. ___ Clear personnel from ignition area

50. ___ Turn on TM-11
51. ___ Turn on Hipotronics power supply
52. ___ Raise Hipotronics voltage to 9 kV (charge for 2 minutes)
53. ___ Check data acquisition system(s); rearm if necessary
54. ___ Engage 12 V Power Relay on Driver Controller
55. ___ Arm Driver Controller
56. ___ To initiate shot, press and hold red Fire button Time: _____
57. ___ If system misfires, execute Misfire Procedure and continue with item 65
58. ___ Turn down Hipotronics voltage and switch it off
59. ___ Turn off TM-11
60. ___ Turn off Driver Controller
61. ___ Download data
62. ___ Discharge capacitors with grounding stick
63. ___ Short capacitors with shorting cable
64. ___ Turn off warning lights - **Laboratory Access is Unrestricted**

Tube Venting Procedure

65. ___ Switch on 12 V relay on Main Control Panel and close it
66. ___ Switch on Heise gauge and thermocouple vacuum gauge
67. ___ Close L1
68. ___ Check that EDL is not using pump
69. ___ Open vacuum manifold valve (at pump); set vacuum pump status indicator
70. ___ Open V1, V2, E1, and Heise gauge isolation valve Final pressure: _____ kPa
71. ___ When pressure drops to about 100 millitorr, open T1, T2 (and T3)
72. ___ When pressure reaches 200 millitorr, close T2 and V2
73. ___ Turn off thermocouple vacuum gauge
74. ___ Close vacuum manifold valve (at pump); set vacuum pump status indicator
75. ___ Open L1 to vent vessel up to atmospheric pressure

Record wave speeds:

	1	2	3	CJ Speed
Times	μs	μs	μs	
Speeds	m/s	m/s		m/s

Remarks:

Appendix B

Strain measurements

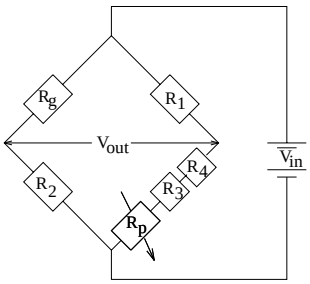

Figure B.1: Wheatstone bridge circuits

The output voltage for the Wheatstone bridge is:

$$\frac{V_{out}}{V_{in}} = \frac{R_3 + R_4 + R_p}{R_1 + R_3 + R_4 + R_p} - \frac{R_2}{R_g + R_2} \tag{B.1}$$

The strain, ε, is then calculated from:

$$\varepsilon = \frac{-4V_r}{GF\,(1 + 2V_r)} \tag{B.2}$$

where V_r is calculated from the difference between the strained and the unstrained case [1]:

$$V_r = \left.\frac{V_{out}}{V_{in}}\right|_s - \left.\frac{V_{out}}{V_{in}}\right|_u \tag{B.3}$$

[1] For a balanced bridge the output voltage in the unstrained case is set to zero by varying the resistance R_p

For the measurements, an input voltage of 12 V was used. The amplifiers were set at a gain of 500 and a bandwidth of 10 kHz. The other spceifications are given in table B.1. The setup is given in figure B.2. The power schematic is given in figure B.3. Note that the ground and the negative were connected in order to eliminate 60 Hz noise.

The weakest point in the strain setup is the connection between the wires from the strain gages and the bananaplugs. Before each run the connections were checked. The bridges were balanced and the wires were "wiggled". If the motion introduces a shift in output voltage of the bridge, the connection has to be renewed.

Description of components
Strain gages:
Micro Measurement strain gages type WK-13-250BF-10C
Resistance Rg: 1000 Ω $\pm$ 0.3
Gage length: 6.25 mm. Overall length: 9.53 mm
Grid width: 3.18 mm. Overall width: 3.18 mm.
Matrix size: 13.2 mm x 5.6 mm (L x W)
Wheatstone bridge circuits:
R_1 and R_2: 1 kΩ, 1% metalfilm, $\frac{1}{4}$ W
R_3: 909 Ω, 1% metalfilm, $\frac{1}{4}$ W
R_4: 40.2 Ω, 1% metalfilm, $\frac{1}{2}$ W
Trimmer R_p: 10 turn wirewound, 100 Ω
Scale dial, 10 turn
Amplifiers:
#1: Preston Scientific 8300 XWB. Pool nr. 1-49
#2: Preston Scientific 8300 XWB. Pool nr. 1-51
#3: Preston Scientific 8300 XWB. Pool nr. 1-50
#4: Preston Scientific 8300 XWB. Pool nr. 1-48
#5: Preston Scientific 8300 XWB. Pool nr. 1-6
#6: Princeton Applied Research 113. Pool nr. 1-7
#7: Princeton Applied Research 113. Pool nr. 1-25
#8: Princeton Applied Research 113. Pool nr. 1-17
BNC cable:
BNC - type RG-58 - 50 Ω

Table B.1: Specifications equipment strain measurements

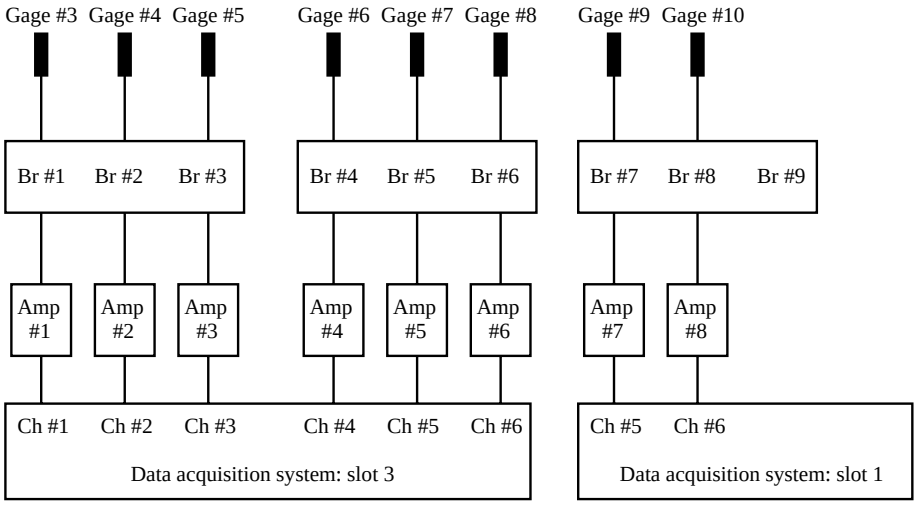

Figure B.2: Equipment for strain measurements

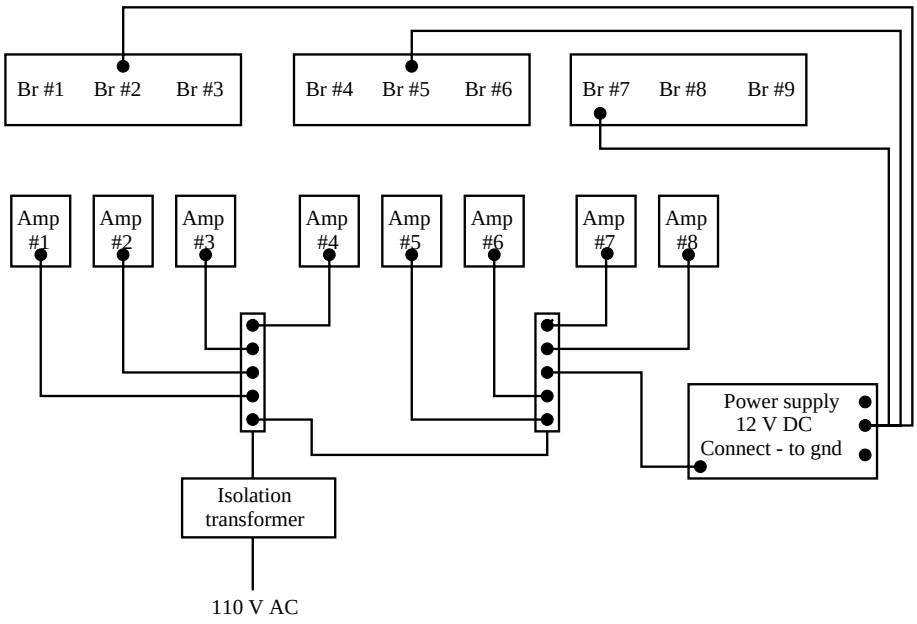

Figure B.3: Power supply for strain measurements